**Master's thesis**

Karina Trøan Eidem and Kristian Werner Lindgaard

# Large scale model testing of CPTU in sand

Master's thesis in Civil and Environmental Engineering
Supervisor: Steinar Nordal
Co-supervisor: Jean-Sébastien L'Heureux

June 2022

**NTNU**
Norwegian University of
Science and Technology

NGI

Karina Trøan Eidem and Kristian Werner Lindgaard

# Large scale model testing of CPTU in sand

Master's thesis in Civil and Environmental Engineering
Supervisor: Steinar Nordal
Co-supervisor: Jean-Sébastien L'Heureux
June 2022

Norwegian University of Science and Technology
Faculty of Engineering
Department of Civil and Environmental Engineering

**NTNU**
Norwegian University of
Science and Technology

# Preface

This master's thesis in TBA4900 Geotechnics was written in the spring of 2022 and is the final project for the Master of Science in Civil and Environmental Engineering at the Norwegian University of Technology and Science (NTNU). The study consisted of large-scale model testing using CPTU in sand. The study is part of an ongoing research at NTNU, where the aim is to improve the detection and accurate characterization of thin clay layers in sand. The project is done in cooperation with the Norwegian Geotechnical Institute and Dr. techn. Olav Olsen.

Takk!

Trondheim, 2022-06-10

*Kristian Lindgaard*

Kristian Werner Lindgaard

*Karina Trøan Eidem*

Karina Trøan Eidem

A preliminary Specialization project in (TBA5410) was conducted in the fall semester of 2021. Since this thesis is a continuation of the work performed during the Specialization project, some of the theoretical framework and laboratory procedures are adapted from the work from the preliminary report. Mostly, the previous work is edited and developed, but some self-plagiarism will occur. This primarily applies to chapter 3 on laboratory procedures, as it is the least edited chapter.

# Abstract

Field investigations are essential for assessing in situ design parameters, which could be crucial for preventing landslides. The cone penetration test is an important field test due to its availability, cost-effectiveness and simplicity. However, the detection of thin, weak layers in sand deposits is challenging since the soil around the advancing cone tip will be influenced by the surrounding layers, thus affecting the cone resistance. For accurate detection and characterization of thin, weak clay layers, it is not only important to understand the behaviour of the weak layer but also to have a clear idea of the behaviour of the sand itself. The failure mechanism around the advancing cone tip is complex, and an improved characterization of the failure mechanism in sands will better the understanding of the layering effects and the soil behaviour affecting the cone resistance between two layers.

Through three large scale physical experiments in a chamber, the soil behaviour of sand during CPTU-testing was investigated. The strength and stiffness parameters for the used sand were determined through supplementary laboratory tests such as triaxial tests and oedometer tests. The CPTU-measurements were investigated using the effective stress based interpretation method based on the theoretical framework from the bearing capacity theory suggested by Janbu and Senneset (1974), called the NTH method. This method implements the plastification angle, $\beta$, which defines the geometric size of the stress field around the advancing cone. $\beta$ was used in this study to investigate the failure mechanism around the advancing cone. This parameter was determined through back-calculation using the NTH method, and the correlation between $\beta$ and $\psi_{BJ}$ was investigated. The state parameter was determined based on void ratio and stress and from the empirical relation to cone resistance presented by Been et al. (1987). It is found that $\psi_{BJ}$ influences the plastification field around the cone tip and describe the soil behaviour for different void ratios and stress states very well. A theoretical relation between the plastification angle and the state parameter was determined during this study, which generates similar values for $\beta$ as using the NTH method. This supports that a correlation between the two theories exists. The relation between $\psi_{BJ}$ and $\beta$ gives a more theoretically consistent determination of the plastification angle, $\beta$, and will improve the interpretation of the design parameter, $\phi$, the angle of friction. This study has improved the understanding of the soil behaviour regarding the size of the plastified field under the advancing cone, considering the state of the sand.

A numerical analysis using the Material point method was conducted in this study, where a model of the chamber and cone was developed to simulate the CPTU-test in sand. This analysis aimed to investigate the plastified zones around the penetrating cone in terms of the shear strain and the volumetric strain. This was used for comparison of the plastification angle. The numerical analysis did not confirm or

refute the experimental results but showed expected dilation and contraction for positive and negative dilatancy angles, respectively.

Great time and effort were put into the building of the test specimen. Each layer was constructed similarly, and the vibration time was increased for each layer to prevent over compaction. Despite this, it was found challenging to build a homogeneous sand sample with the same density all throughout the sample. This makes high accuracy in the interpretation of the state parameter rather difficult because of the variation in void ratio. For further research, it is recommended to see if improvements in the build-in procedure for the sand could be developed. The wetting and tamping process layer by layer should be carefully evaluated and improved.

# Sammendrag

Feltundersøkelser er viktig innenfor geoteknisk prosjektering, og kan være uunværlig for å unngå jord-skred. CPTU-testen er en viktig feltundersøkelse på grunn av at det er en metode som er enkel og tilgjengelig å bruke, i tillegg til at den er kostnadseffektiv. Å finne tynne, svake leir lag i sandavset-ninger kan derimot være en utfordring på grunn av at det deformerte jordmaterialet rundt spissen av sonden vil bli påvirket av omkringliggende lag. Dette vil ha innvirkning på spissmotstanden, $q_c$. For å kunne finne og karakterisere tynne, svake lag er det også viktig å ha forståelsen for oppførselen i sanden alene. Bruddmekanismen rundt spissen av sonden er kompleks, og en forbedret metode for tolkning av bruddmekanismen i sand vil forbedre forståelsen av effektene av lagdelingen of hvordan spissmotstanden påvirkes i overgangen mellom lagene.

Oppførselen til sand under en CPTU-test er undersøkt gjennom tre fysiske laboratorieforsøk, hvor sanden er bygget inn i et stort kammer. Styrke- og stivhetsparameterne for sanden er bestemt gjen-nom treaksialt trykkforsøk og ødometerforsøk. Målingene fra CPTU-testen er undersøkt ved bruk av effektivspenningsbaserte løsninger med bæreevneteorien, utviklet av Janbu and Senneset (1974), som teoretisk ramme. Denne metoden introduserer plastifiseringsvinkelen,$\beta$, som definerer størrelsen på de plastifiserte sonene rundt spissen på sonden. $\beta$ ble i dette studiet benyttet som grunnlag for å et-terforske spenningsfeltet som oppstår i sanden rundt spissen av sonden. Plastifiseringsvinkelen ble bestemt gjennom tilbakeberegning ved bruk av NTH-metoden. Korrelasjonen mellom plastifiserings-vinkelen og tilstandsparameteren $\psi_{BJ}$ har blitt undersøkt. Tilstandsparameteren ble bestemt basert på målinger av poretall ved gitt spenningstilstand, i tillegg til å bli bestemt gjennom den empiriske relasjonen til spissmotstanden presentert av Been et al. (1987). Gjennom studien ble funnet at $\psi_{BJ}$ påvirker plastifiseringsfeltet som oppstår rundt sonden, og beskriver sandens oppførsel for forskjel-lige poretall og spenningstilstand godt. En teoretisk relasjon mellom plastifiseringsvinkelen, $\beta$, og tilstandsparameteren, $\psi_{BJ}$, har blitt uttrykt gjennom dette prosjeket. Verdiene for $\beta$ som blir generert gjennom denne relasjonen viser seg å være svært like verdiene til $\beta$ beregnet fra NTH metoden. Dette underbygger at en korrelasjon mellom de to teoriene eksisterer. Relasjonen mellom $\psi_{BJ}$ og $\beta$ gir en mer konsekvent, teoretisk bestemmelse av plastifiseringsvinkelen. Dette forbedrer tolkningen av friks-jonsvinkelen, $\phi$. Denne studien har forbedret forståelsen av oppførselen til sanden når det kommer til størrelsen på det plastifiserte spenningsfeltet foran konspissen, når tilstanden til sanden er tatt med i betrakning.

En numerisk analyse ved bruk av Material point method er utført gjennom studiet, hvor en modell av kammeret og CPT-en ble utviklet for å simulere CPTU-testing i sand. Formålet med analysen var å tolke

de plastifiserte sonene rundt konspissen i form av skjærtøyning og volumtøyning. Dette resultatet ble brukt som sammenlikningsgrunnlag for plastifiseringsvinkelen bestemt gjennom laboratorieforsøkene. Den numeriske analysen ga derimot ikke noen entydige resultater, men viste som forventet en dilasjon og kontraksjon for henholdsvis positiv og negativ dilatansvinkel.

Mye tid ble brukt til å bygge inn sandprøvene. Hvert lag ble konstruert likt, og vibrasjonstiden ble økt for hvert lag for å unngå overkompaksjon. På tross av dette, ble det funnet utfordrende å bygge en homogen sandprøve med den samme densiteten gjennom hele prøven. Dette gjør det vanskelig å kunne tolke tilstandsparameteren med høy nøyaktighet, på grunn av endring i poretall. For fremtidige forsøk er det anbefalt å utvikle bedre metoder for innbyggingsprosedyrene. Fukting- og stampingsprosessen lag for lag bør evalueres nøye og utbedres.

# Contents

# Figures

# Tables

# List of Symbols

| | | | | |
|---|---|---|---|---|
| $\beta$ | Plastification angle | | | |
| $\gamma$ | Dry unit weight | a | Unequal area effect |
| $\Delta$ | Change parameter | a | attraction |
| $\delta'$ | Mobilized interface friction angle | $A_c$ | cross-sectional area cone |
| $\epsilon$ | Strain | $A_N$ | Cross-sectional area shaft |
| $\epsilon^e$ | Elastic strain | $A_s$ | Area friction sleeve |
| $\epsilon^p$ | Plastic strain | $B_0$ | Foundation width |
| $\epsilon_v$ | Volumetric strain | D | Diameter cone |
| $\epsilon_1$ | Axial strain | $D_c$ | Diameter chamber |
| $\mu'$ | Friction coefficient | $D_r$ | Relative density |
| $\kappa$ | Flexibility parameter OC-region | e | void ratio |
| $\lambda$ | Flexibility parameter NC-region | $e_{max}$ | Maximum void ratio |
| $\lambda_{ss}$ | Inclination of CSL | $e_{min}$ | Minimum void ratio |
| $\mu'$ | friction coefficient | $e_{ss}$ | Void ratio at state |
| $\nu$ | Void ratio | $e_0$ | Void ratio, measured condition |
| $\nu_p$ | Poisson's ratio | $F_s$ | Force on friction sleeve |
| $\rho$ | Density | $f_s$ | sleeve friction |
| $\rho_d$ | Dry density | $H_s$ | Height of sampler |
| $\rho_s$ | Grain density | $\delta h$ | Settlements from compaction |
| $\sigma'$ | effective stress | K | Earth pressure coefficient |
| $\sigma'_0$ | initial effective stress | k | Normallized $q_c$ value for $\psi_{BJ} = 0$ |
| $\sigma'_a$ | Effective axial stress | l | Decay length |
| $\sigma_{atm}$ | Atmospheric pressure | m | modulus number |

| | | | |
|---|---|---|---|
| $\sigma'_h$ | Effective horizontal stress | m | slope of the normallized $q_c - \phi_{BJ}$ |
| $\sigma'_v$ | effective vertical stress | M | Modul |
| $\sigma'_v n$ | effective net vertical stress | $N_{kt}$ | Total stress based bearing capacity factor |
| $\sigma'_v 0$ | initial effective vertical stress | $N_m$ | cone resistance number |
| $\sigma'_1, \sigma'_2, \sigma'_3$ | Principal effective stress | $N_q$ | Bearing capacity factor |
| $d\overline{\sigma'}$ | Effective stress increment | p | mean stress |
| $d\overline{\sigma'^p}$ | plastifying stress increment | p' | effective mean stress |
| $d\overline{\sigma'^e}$ | elastic stress increment | $Q_c$ | Force acting on cone tip |
| $\phi$ | Friction angle | $q_c$ | Cone resistance |
| $\phi_{cs}$ | Friction angle at critical state | $q_n$ | Net cone resistance |
| $\psi$ | Dilatancey angle | u | excess pore pressure |
| $\psi_{BJ}$ | The state parameter | z | depth from chamber top |

# Chapter 1

# Introduction

Field investigations provide data to obtain information about the in situ conditions of the soil and are an essential step in geotechnical engineering to prevent landslides or other failures. The detection of thin clay layers is crucial to prevent landslides. Analysis of earlier landslides in Norway show that these thin layers may act as a sliding plane of the landslide L'Heureux et al. (2010).

The piezocone penetrometer test (CPTU) is an effective tool widely used for assessing in situ soil parameters and determining soil material type and stratification. However, the detection of thin clay layers (<20 cm) is challenging since the soil around the tip of the advancing cone will be affected by the surrounding layers. Hence, the cone resistance of soundings through thin layers are not reaching the actual characteristic cone resistance of the thin layer. Due to this thin layer effect, an overestimation of the resistance of the soil could occur (Skrede, 2021).

In recent years, research on the thin-layering effects of the cone penetration test has been done. The current study is a continuation of an ongoing research project at the Norwegian University of Science and Technology (NTNU). Through their master's theses, Hammer (2020) and Skrede (2021) investigated the cone resistance response ($q_c$) in thin clay layers embedded in sand. To learn more about the layering effects of the CPTU, and how a surrounding layer affects the cone resistance of a thin clay layer embedded in sand deposits, it is necessary to have a good understanding of the natural variation of the cone penetration readings in a deposit of pure sand and a deposit of pure clay separately. Because of its impact on geohazards, many studies have been done on CPTU-testing in clay. However, less research has been done in Norway on CPTU-testing in sand. The studies by Hammer (2020) and Skrede (2021) indicate a significant variation in tip resistance and friction in what is meant to be a homogeneous, thick sand layer. Consequently, it is crucial better understand the soil behaviour during cone penetration in the sand itself. This variation needs to be studied to determine how large it is and to find the reason for it. One may then be able to reduce the variations in future tests. Preliminary work has been done in connection with TBA4510 Geotechnical Engineering, Specialization Project, to develop repeatable methods for CPTU testing in a chamber with sand. These methods are continued in this study.

There exist many interpretation methods for data obtained from CPTU-testing. Janbu and Senneset

(1974) developed an interpretation method based on classical bearing capacity theory, implementing effective stress parameters applied on both sand and clay. Therefore, this study aims to revisit and hopefully improve the NTH method as an interpretation method of CPTU-data in sands, particularly regarding the plastification angle controlling the extent of the plastified zone and the interpretation of $\phi$. It has been suggested to relate the plastification angle to porosity or, more specifically, to the Been and Jefferies (1985) state parameter.

## 1.1 Problem formulation

The NTH method introduces an idealized stress field around the cone tip, limited by the plastification angle, $\beta$. However, a lot of uncertainties are associated with the plastification angle, as it is a challenging parameter to determine from in situ test methods. The purpose of this study is to examine the tip resistance in view of the stress field around the advancing cone, with the aim to improve the understanding and interpretation of the plastification angle of the soil during cone penetration.

The scope of the project consists of investigating the following problem:

> Investigation of the sand behaviour for different stress states around the advancing cone. Investigate how the state parameter of the soil influences the tip resistance, and in particular, the plastification angle during cone penetrometer testing. How can the stress field under the advancing cone, based on bearing capacity theory from the NTH method, be more precisely understood?

The problem will be investigated through three large scale piezocone penetrometer tests in sand built in a large concrete chamber. The plastification angle defines the geometric size of the plastified zone and will be investigated through this study as a measure of the failure mechanism around the cone tip. The state parameter approach will be implemented into the NTH method, and it will be investigated if any correlation exists between the plastification angle and the state parameter. In addition, a numerical analysis using the material point method will be conducted for comparison to the empirical laboratory study.

The main objectives of the project consists of:

1. Gathering CPTU data by conducting three large scale chamber tests with piezocone penetrometer testings in sand. Stress levels in the chamber should be selected and the porosity with depth should be measured.
2. Obtaining material data of the sand through triaxial tests, oedometer tests and other supplementary laboratory tests. Key parameters are strength data as friction angle and stiffness data.
3. Interpreting the CPTU data using the NTH method.

4. Assessing the plastification angle, $\beta$ using the NTH method.
5. Determining the critical state line of the sand from triaxial testing and determining the state parameter of the sand.
6. Assessing the correlation between the state parameter and plastification angle.
7. Develop a theoretical correlation between the plastification angle from bearing capacity theory, to the critical state soil parameter.
8. Numerical analysis using material point method and comparing to the NTH method.

## 1.2 Limitations

There are some limitations associated with the physical experiments and the numerical analysis. They are summarized below.

- Challenges associated with the physical experiments

  - It was challenging to obtain homogeneous sand samples as desired due to the build in procedures of reconstituted sand in the chamber. Difficulties in sampling of sand, which results in an overestimation of void ratio.
  - The boundary effects does not replicate in situ conditions. The cone resistance, $q_c$, is not corrected for any boundary conditions. The boundary effects are characterized trough measurements from implemented earth pressure cells and Janssens formula for silo effects, but they are difficult to determine accurately.
  - The CPTU tests are performed in the proximity of each other. The cone resistance will be influenced of the spacing.
  - The stress level in the chamber is challenging to accurately determine due to some sensitivity drift and challenges associated with calibration of the pressure cells. The readings from the pressure cells are assumed to be accurate and is the basis for determining the vertical and horizontal stress in the chamber, in addition to the earth pressure coefficient, $K_0$.

- Limitations associated with the analysis

  - The failure mechanism is complex. In this thesis, only the plastification field based on the bearing capacity theory (NTH method) is considered.
  - The friction angle for the sand material is assumed known through linear interpolation of triaxial tests based on measured void ratio in the sample.
  - To determine the critical state line of a soil material, 5-6 triaxial tests needs to be performed. Due to time constraints in this project, the position of the critical state line of the sand is determined from critical state points from two triaxial tests. The inclination of the critical state line, $\lambda_{ss}$ is assumed to be equal to the flexibility parameter, $\lambda$, determined from oedometer.

# Chapter 2

# Theoretical framework

This chapter presents the existing literature on cone penetration testing, the critical state theory, chamber testing and the material point method as part of the literature study done during this project. This chapter presents the existing literature on cone penetration testing, the critical state theory, chamber testing and the material point method. It is the basis for further study and analysis in this thesis.

## 2.1 Cone penetrometer test

The cone penetrometer test (CPT) was first introduced in Norway in the early 1950s. The test has since been developed, and with the addition of excess pore pressure measurements when the piezocone penetrometer (CPTU) was introduced in the late 1970s. The cone penetration test has been widely used for assessing in situ soil parameters and determining the stratigraphic layering of the ground. It also provides data to evaluate important geotechnical design parameters (Lunne et al., 1997). It is a simple, reliable, and cost-effective field investigation test, making it an essential tool in the conventional geotechnical field. This chapter presents the measurements, the testing equipment and the interpretation methods of the acquired CPT data.

### 2.1.1 CPTU measurements

The conventional CPTU measures cone resistance, $q_c$, sleeve friction, $f_s$, and the excess pore pressure, $u$. The equipment consists of a cone penetrometer and pushing equipment in the form of a series of rods. The standard cone penetrometer, according to the European Standard (ISO 22476-1:2012), has a cone angle of 60° and a cross-sectional area of the cone $A_c$ of $10cm^2$, corresponding to a diameter of $35,7mm$, as shown in figure 2.1.
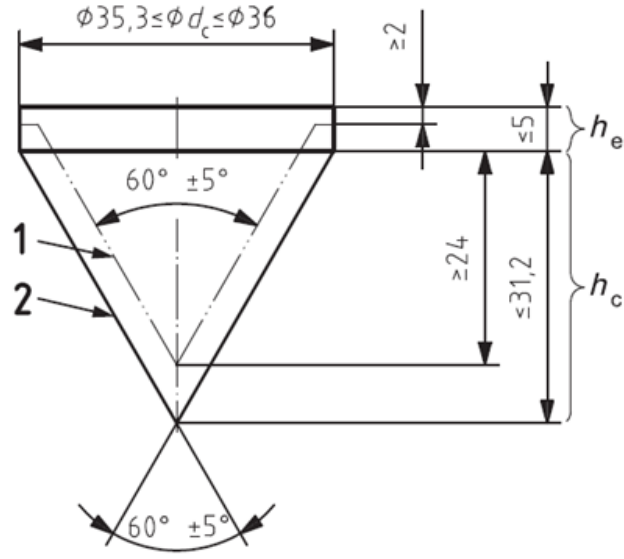
**Figure 2.1:** Standard cone geometry with cone angle of 60° and cross-sectional area of $10cm^2$ according to European Standard (ISO 22476-1:2012).

The cone is placed on the end of the rods. It is then pushed through the ground at a constant rate providing continuous registration of the cone resistance (Lunne et al., 1997). According to the European Standard, the rate of the cone penetration should be $20mm/s \pm 5mm/s$. Dividing the total force acting on the cone tip, $Q_c$ by the cone area, $A_c$, gives the cone resistance, $q_c$, expressed in Equation 2.1, which is a measure of the shear strength of the soil (Lunne et al., 1997).

$$q_c = \frac{Q_c}{A_c} \qquad (2.1)$$

The geometry of the cone causes the pore water pressure to act on the shoulder behind the cone and on the friction sleeve during penetration (Campanella et al., 1982). Because of this, the cone tip resistance, $q_c$, should be corrected for this unequal area effect to the corrected total cone resistance $q_t$ according to equation 2.2. The net cone resistance is defined in Equation 2.3.

$$q_t = q_c + u_2(1-a) \qquad (2.2)$$

$$q_n = q_t - \sigma_{v0} \qquad (2.3)$$

Where $q_c$ is the uncorrected cone tip resistance, $u_2$ refers to the $u_2$ pore pressure filter position, and $a$ is the unequal area factor. This factor is equal to the ratio between the cross-sectional area of the

shaft, $A_N$, and the projected area of the cone, $A_C$. This effect is essential for CPT testing in fine-grained soils. However, this effect is insignificant in sands, as the cone tip resistance, $q_c$, will be large relative to the pore water pressure (Robertson, 2009). In such cases, the uncorrected cone resistance, $q_c$, can be utilized.

During penetration, the force acting on the friction sleeve divided by the surface area of the friction sleeve, $A_s$ expresses the sleeve friction, $f_s$ (Lunne et al., 1997). The sleeve friction is presented in Equation 2.4.

$$f_s = \frac{F_s}{A_s} \tag{2.4}$$

The soil material around the sleeve will become significantly disturbed during penetration of the cone. For fine-grained soils, the sleeve friction, $f_s$, will represent an estimation of the remoulded shear strength (Robertson, 2009).

The incorporation of pore water pressure measurements proved to be important for the interpretation of CPT data. Janbu and Senneset, in addition to Schmertmann, recognized through studies published in 1974 that the effects of pore water pressure changes and dissipation had the potential for detecting thin permeable layers embedded in clay (Lunne et al., 1997).

Pore pressure is typically measured at one, two or three locations on the penetrometer. Figure 2.2 illustrates the possible positions of the filters for pore pressure measurements, denoted $u_1$, $u_2$ and $u_3$. Although there is no standardized position for the filter, the European Standard (ISO 22476-1:2012) suggests the usage of the $u_2$-position, located just behind the cone. In this position, the filter is less prone to damage and is also the most appropriate location for correction of the cone tip resistance according to equation 2.2. The saturation process is also simpler in this location.
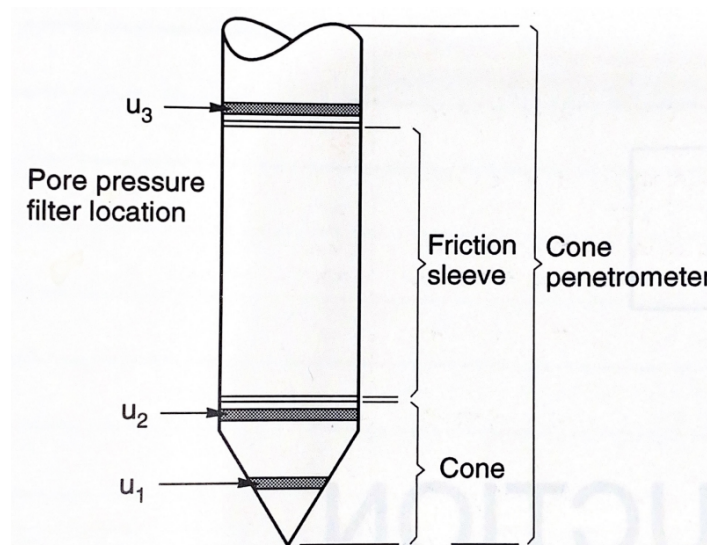


**Figure 2.2:** Proposed locations for filters for pore pressure measurements. The European Standard (ISO 22476-1:2012) suggests the $u_2$ position for the filter.

6

### 2.1.2 Accuracy and repeatabilityy

It is not advisable to base final design parameters solely on the results from CPTs, but a combination of in situ CPTU-test and laboratory testing is advised (Lunne and Christoffersen, 1983). The CPTU-test shows good repeatability from one test to another. The cone penetration test is popular in conventional geotechnical engineering due to its cost-effectiveness and availability. In addition, the test generates repeatable and reliable results for soil investigation. Figure 2.3 shows a series of cone penetration tests at the Øysund research site presented by Hammer (2020). The series of testing supports the repeatability, as the cone resistance shows the same trends for the same test site.
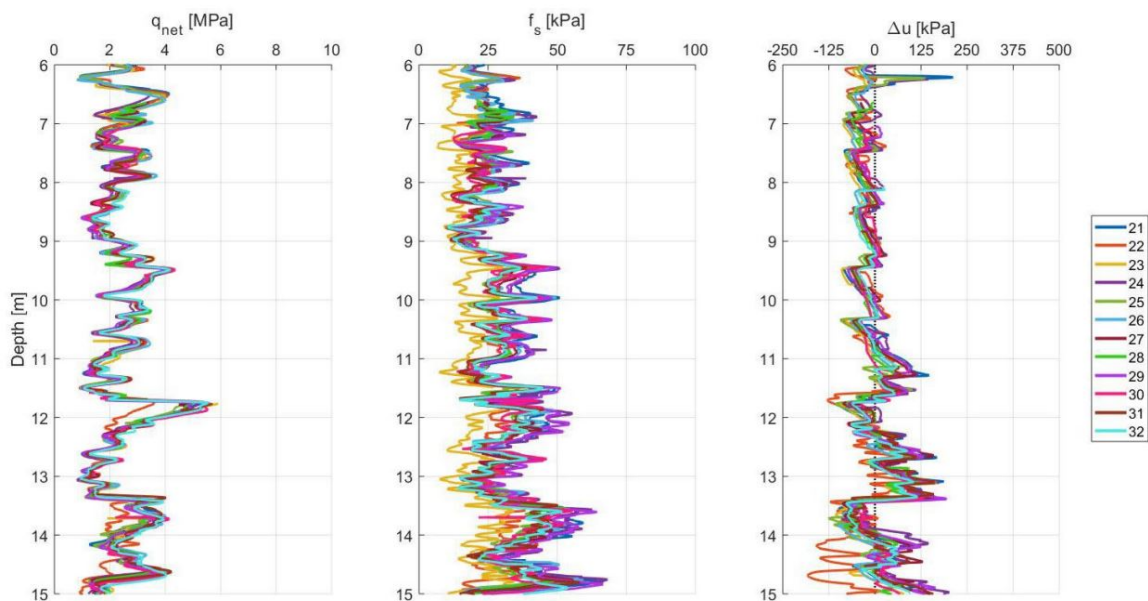


**Figure 2.3:** Cone penetration testing performed at Øysund research site. Showing the repeatability of the cone penetration test. From Hammer (2020).

### 2.1.3 Flow mechanisms

During penetration of the cone through the soil, the cone tip will push the soil to the side and upward. Hence, a plastification zone of the soil surrounding the cone tip will occur. The deformation pattern that occurs around the advancing cone will depend on the geometry of the cone and the material of the soil.

Many studies have been done on soil plastification and the flow mechanism, and a lot of theoretical frameworks for the failure geometry are presented in the literature. When using the NTH method for interpreting the CPTU-data, the plastification angle that limits the area of the plastified zone is of great importance. It is, therefore, relevant to look into studies that have been carried out on the plastification

mechanisms around the advancing cone.

Figure 2.4 shows a summary of the different flow mechanisms around the cone tip that is presented in literature based on the two main theories, the bearing capacity theory and the cavity expansion theory (Emdal, 2020). Figure 2.5 represents the idealized stress field presented by (Janbu and Senneset, 1974). The theoretical framework for the failure mechanism based on the bearing capacity theory is further described in chapter 2.2.3
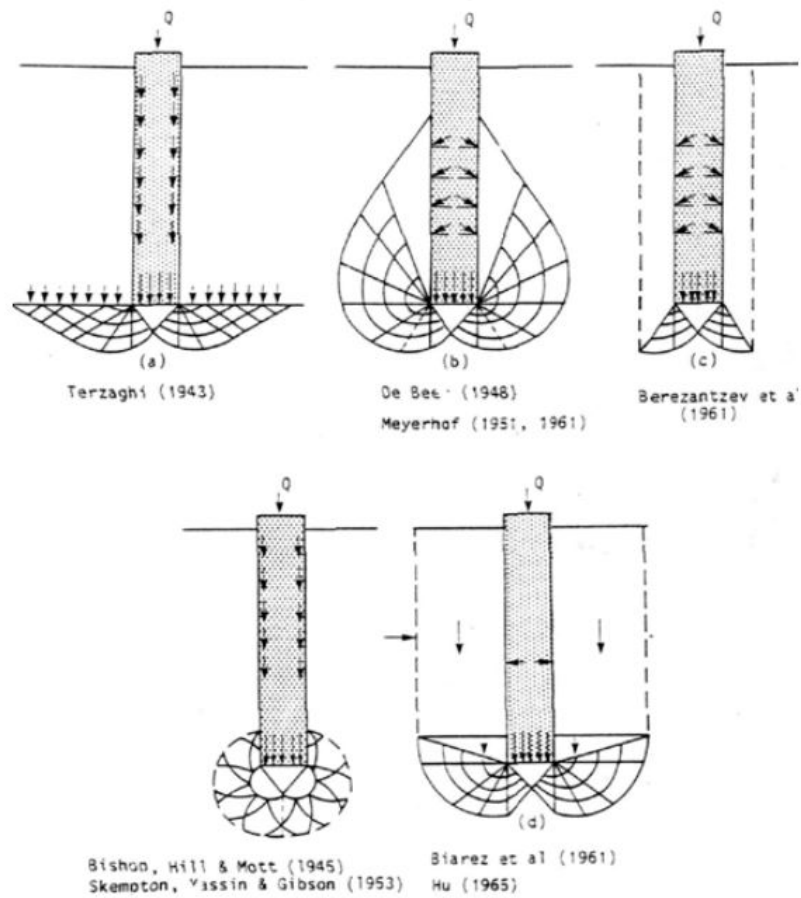


**Figure 2.4:** Different failure surface assumptions presented in the literature based on the theoretical framework from both bearing capacity theory and expansion cavity theory. Adapted from Emdal (2020).
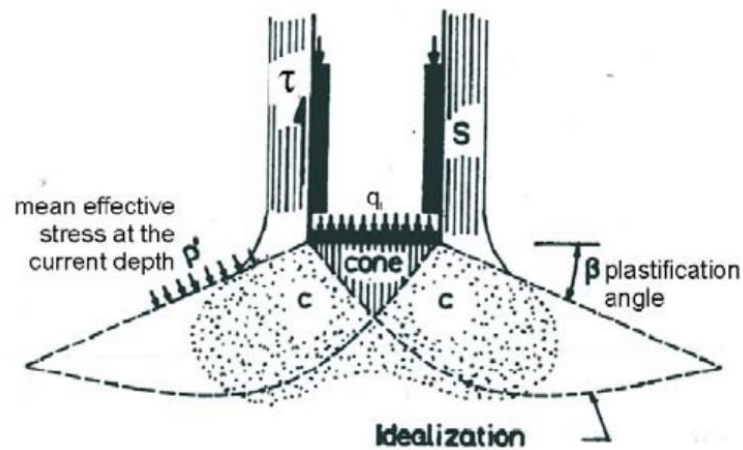
**Figure 2.5:** Theoretical framework for the flow mechanism that occurs around the advancing cone, based on bearing capacity theory. Illustrations from Sandven (1990).

There has also been much development in recent years. Paniagua López (2014) conducted a series of tests on remoulded samples of silty soils using x-ray 3D-DIC imaging to examine the change in soil fabric during cone penetration and evaluate the disturbed zones. Figure 2.6 shows the volumetric deformation around the cone and shaft.
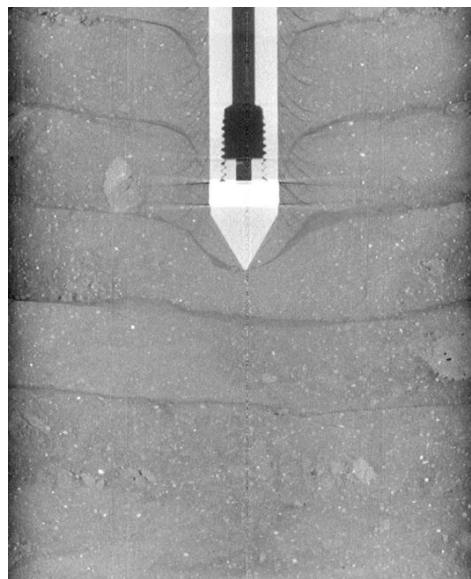


**Figure 2.6:** Volumetric deformation around the advancing cone in silty soils. From Paniagua López (2014).

Through these studies, Paniagua found a complex failure mechanism with compaction close to the cone tip and dilatation in the soils further away from the tip. Figure 2.7 shows 3D-DIC imaging of the change in volumetric strain and shear strain around the cone tip during penetration, illustrating the failure mechanism, including the zones of compaction and dilation.

9
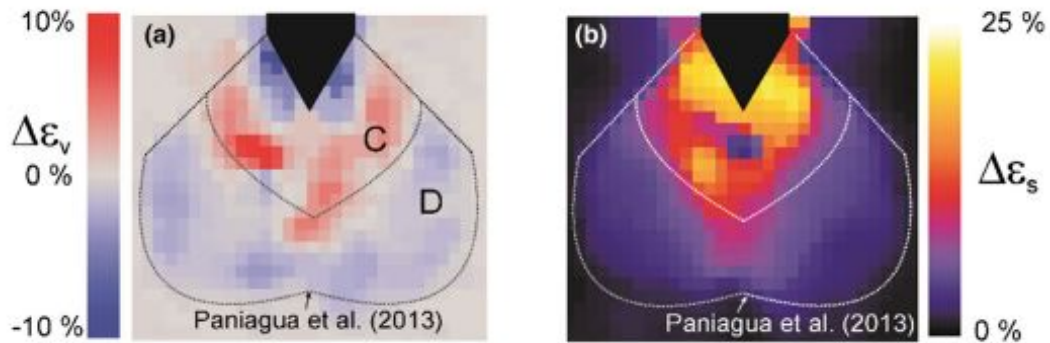
**Figure 2.7:** Change in volumetric strain (left) and shear strain (right) around the cone tip during penetration with 3D-DIC imaging. Showing zones of compaction (C) and dilation (D). From Paniagua et al. (2014).
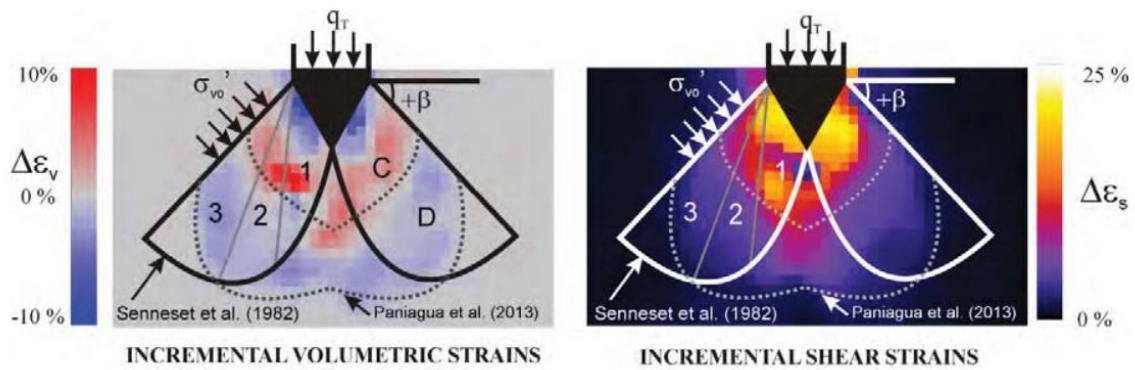


**Figure 2.8:** Comparison between the failure surface from 3D-DIC and the failure surface for the NTH intepretation model. Shows zones for compaction (C) and dilation (D). From Paniagua et al. (2018)

Paniagua went on to investigate whether the failure mechanism from the NTH interpretation model is a suitable fit for the actual failure mechanism that occurs around the penetrating cone based on the 3D-DIC CT scans (Paniagua et al., 2018). This is illustrated in figure 2.8.

The results from the 3D scanning show clear zones for compaction and dilation, as shown in Figure 2.7. Paniagua et al. (2018) compared the realistic approach, including the observed dilative behaviour of the soil with the NTH-method. Fitting the failure surface, Paniagua observed that the active Rankine zone fitted well with the compaction zone and that the dilation zone was a well-suited fit for the passive Rankine zone.

### 2.1.4 Layering effects

One of the key applications of the cone penetrometer test is the characterization of the soil stratigraphy and the detection of the layering of the soil. However, the detection of thin clay layers (<20 cm) could be challenging with CPTU-testing. L'Heureux et al. (2010) stressed the significance of thin clay layers working as a sliding failure plane of past landslides in Norway. It is therefore important to develop new methods for detecting these thin layers.

For the last two years, there has been an ongoing research program performed by Hammer (2020) and Skrede (2021) at NTNU, aiming to investigate the layering effects of cone penetration testing and how the cone resistance, $q_t$, is affected by the surrounding layers and by the interfaces between layers. Through physical experiments, Hammer (2020) and Skrede (2021) found that the surrounding layers may significantly influence the soil close to the layer interface and in thin layers. Hence the tip resistance may not reflect the actual properties of the soil of thin layers or near interfaces. The distances of transition in the materials are defined as sensing- and developing distances, as shown in figure 2.9. Hammer observed through the study that the sensing and developing distance for sand and clay are significantly different.
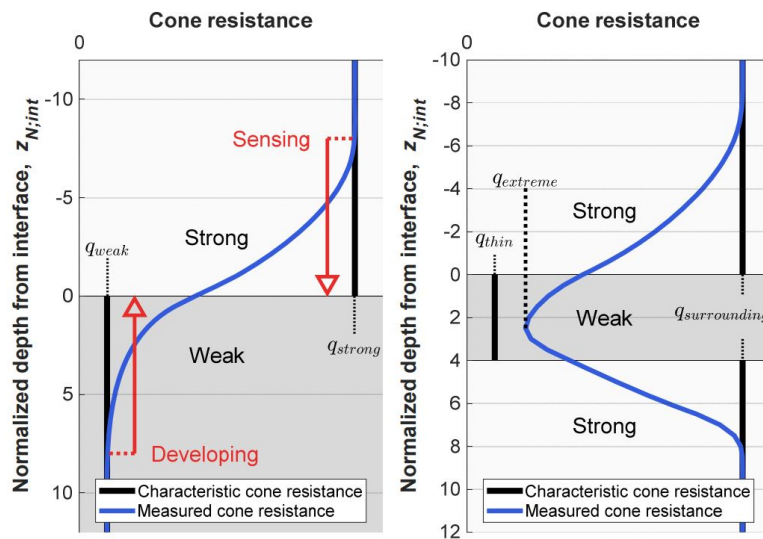


**Figure 2.9:** Illustration of thin-layer effects for a two-layered composition (left) and three-layer composition (right). The distances where the surrounding layers affect the cone resistance of the material are labelled sensing and developing.

Hammer et al. (In press[a]) stated that if the thickness of a weak layer embedded between two strong layers is less than the sum of the developing distance to the previous layer and the sensing distance to the next layer, the characteristic cone resistance will not be reached. Instead, it will overestimate the cone resistance of the weak layer. This effect is illustrated in figure 2.9.

Hammer et al. (In press[a]) suggested that the position of a layer interface could be determined using

the cone resistance change of rate, $q'_t$. Through further studies (Hammer et al., In press[b]), Hammer proposed a method for estimating the position of a layer interface using the peak module number, stating that the module number could be viewed as a measure of the rate of change when a constant cone resistance is assumed. Hammer observed that the position of the peak module number, m, interlined with the position or close to the position of the layer interfaces, as shown in figure 2.10.
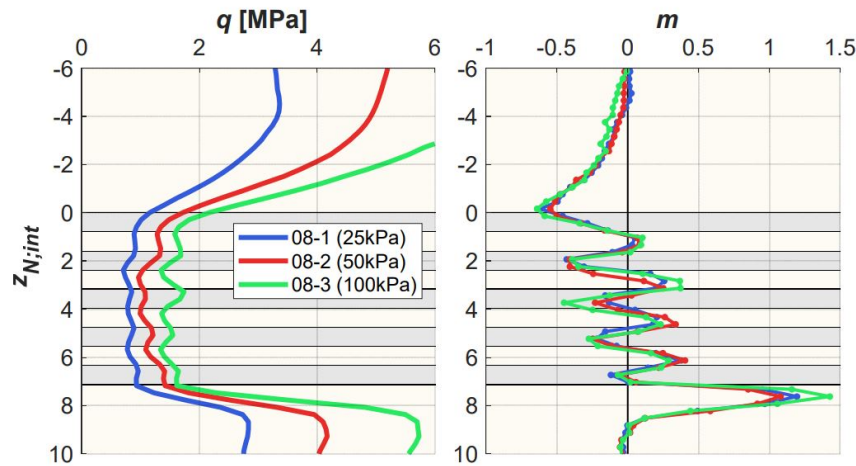


**Figure 2.10:** Cone tip resistance and module number profiles for multiple thin layers of sand and clay. Experiments from de Lange(2018)Adapted from Hammer et al. (In press[b]).

To accurately detect the soil layering with cone penetration testing accurately and achieve accurate detection of thin clay layers, it is crucial to investigate the layering effects and how the soil near layer interfaces affects the cone resistance. In general, the behaviour and layering effects of clay is much studied and covered in the literature because of its sensitivity and impact on geohazards such as landslides. However, to better understand layering effects, it is also of great importance to obtain a better understanding of the behaviour of the sand material.

This current study is a continuation of the research performed by Hammer (2020) and Skrede (2021). While they investigated the layering effects with weight on the importance of thin layers embedded in sand because of its impact on shoreline landslides, this study will investigate cone penetration testing in regard to the sand material alone. This will secure a better understanding of the failure mechanism around the cone and, therefore, a better understanding of how the soil deformation around the cone is affected in the interfaces between sand and clay layers.

## 2.2 Interpretation of CPTU-measurements

Figure 2.11 shows typical CPTU sounding results, presenting both cone resistance, $q_T$ and pore pressure, $u$. From the readings, the layering of the soil can be determined. Sand has typically higher cone

resistance, but since sand is a permeable material, the excess pore pressures are typically equal to zero. Pore pressures typically have a fast response during penetration, and a drop in pore pressure could therefore indicate a layer of drained materials. Due to undrained conditions, sanding in fine-grained materials such as clay will have a higher pore pressure response. Clay will typically have lower cone resistance, dependent on the stiffness of the clay.
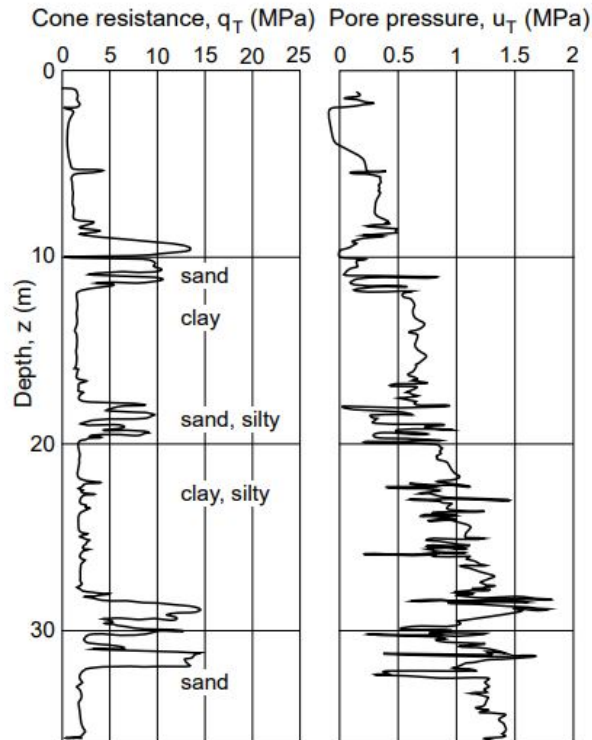


**Figure 2.11:** Typical CPTU sounding results can be used to determine the layering of the soil. Coarse grained materials will typically have higher cone resistance and lower pore pressure response due to the permeability of the soil. Fine grained soils will have a higher pore pressure response, but typically lower cone resistance, dependent on the stiffness of the soil. (Sandven et al., 2017)

### 2.2.1 Interpretation in undrained material

During cone penetration testing performed in fine soil materials such as clay, undrained conditions generally apply. There exist many correlations to determine undrained shear strength, $S_u$. Lunne et al. (1997) presented a summary of the different interpretation methods for CPTU-data in undrained materials. This chapter will present a small summary of the most relevant empirical methods.

The undrained shear strength can be determined from the approach based on classical bearing capacity theory adapted to the penetrating cone using both total and effective cone resistance. The correlation to undrained shear strength using total cone resistance is presented by Equation 2.5.

$$s_u = \frac{q_c - \sigma_{v0}}{N_{kt}} \qquad (2.5)$$

Where $N_{kt}$ represents the total stress-based bearing capacity. Triaxial test results are commonly used to obtain data on $S_u$ to determine $N_{kt}$. Empirically, it is common to use $N_{kt} = 15 \pm 5$. Based on the total stress-based bearing capacity theory, it is common to use the bearing capacity factor, $N_c$, which varies between 6 and 9 (Sandven et al., 2017). According to Lunne et al. (1997), Senneset et al. (1982) suggested that the shear strength could be estimated using effective stress based cone resistance. The correlation is presented by equation 2.6.

$$s_u = \frac{q_t - u_2}{N_{ke}} \qquad (2.6)$$

The shear strength could further be estimated based on cavity expansion theory using the following correlation to excess pore pressure:

$$s_u = \frac{u_2 - u_0}{N_{\Delta u}} \qquad (2.7)$$

A method developed at the Norwegian university of science and technology (previously NTH) by Janbu and Senneset (1974) takes into account the effective stress parameters based on classical bearing capacity formulas for interpreting the CPTU-results for both drained and undrained materials. This method, called the NTH method, is further explained in chapter 2.2.2.

### 2.2.2 Interpretation in drained material

It is challenging to take undisturbed samples of sand. The cone penetration testing is, therefore, a useful test to obtain in situ soil parameters in sands. Cone penetration testing in coarse-grained soil material such as sand is generally performed under drained conditions, and no excess pore pressures should occur due to penetration of the cone (Lunne et al., 1997).

There have been developed several methods to interpret cone penetration test data. These methods are either based on conventional bearing capacity theory, cavity expansion theory or strain path method (Sandven, 1990). Many studies on CPT were performed in calibration chambers from the 1970s to the 1990s. Most methods for interpreting CPT results in sands today are based on these laboratory experiments (Lunne et al., 1997). These studies have shown the correlation between cone resistance and sand density, in situ vertical and horizontal effective stresses and sand compressibility (Lunne et al., 1997).

**Relative density**

The relative density is an important parameter describing the soil properties. Relative density has been commonly used as a soil parameter for cohesionless soils and as the interpretation parameter for cone resistance in sands. The relative density is defined as:

$$D_r = \frac{e_{max} - e}{e_{max} - e_{min}}$$

(2.8)

Where $e_{min}$ and $e_{max}$ are the densest and loosest states of the sand, respectively. There exists no standardised method for determining the porosity limits $e_{max}$ and $e_{min}$. Therefore, the relative density is a difficult parameter to determine since the results from one laboratory may differ from the results from another laboratory due to different test procedures. In this study, the test procedures developed by Deutsche Gesellschaft fur Bodenmechanik (DEGEBO) and Norwegian Geotechnical Institute (NGI) is used. The equation for the void ratio is presented in equation 2.9.

$$e = \frac{V_p}{V_s}$$

(2.9)

Comprehensive studies on CPT-testing in calibration test chambers performed during the last 50 years have shown the correlation between relative density and cone resistance. Karlsrud et al. (2005), at the Norwegian geotechnical institute, developed an empirical correlation to determine the relative density from cone resistance based on the Dr-approach developed by Baldi et al. (1986), referred to as the NGI-99 approach (Karlsrud et al., 2005). The approach suggests that the relative density could be estimated by:

$$D_r = 0.4 \cdot ln\left(\frac{q_c}{22 \cdot (\sigma'_{v0} \cdot \sigma_a tm)^{0.5}}\right)$$

(2.10)

In 1978, Schmertmann proposed an empirical relationship between relative density and friction angle for different grain size characteristics, as shown in Figure 2.12. The Figure shows that the shear strength of cohesionless soil described by friction angle increases with increasing relative density (Lunne et al., 1997).
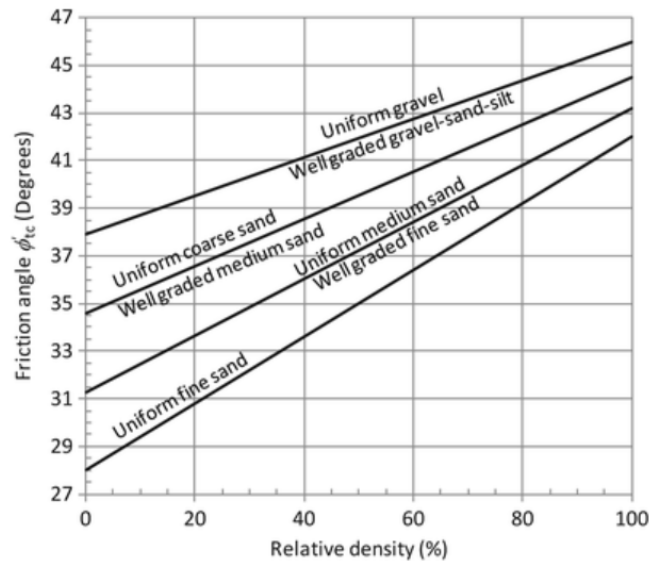
**Figure 2.12:** The relationship between $\phi'$ and $D_R$ suggested by Schmertmann (1978). From Lunne et al. (1997).

**Critical state parameter**

Even though the relative density is a widespread interpretation parameter for CPTU-tests in sand, it has its disadvantages and limitations as a design parameter. The relative density does not take into consideration the compressibility of the soil. Been and Jefferies (1985) therefore introduced a new interpretation parameter, the state parameter, $\psi$. This parameter includes this compressible behaviour of the sand. The state parameter is denoted $\psi$. However, to differentiate from the dilatancy angle, $\psi$, the state parameter will, in this study, be denoted $\psi_{BJ}$. In some figures, the state parameter is denoted with $\psi$ because they are borrowed from Been et al. (1986) and Been et al. (1987).

To explain the state parameter, one needs to understand the critical state concept (also called the steady-state concept) for sand. The critical or steady state is a condition with a given normal stress and large shear strain without any changes in effective stresses or volume. As shown in Figure 2.13, the loose sample will contract during shearing, and the grains will rearrange and fall in between each other until the critical state is reached. The dense sample will dilate during shearing, and the grains will climb on each other until the critical state is reached (Nordal, 2020).
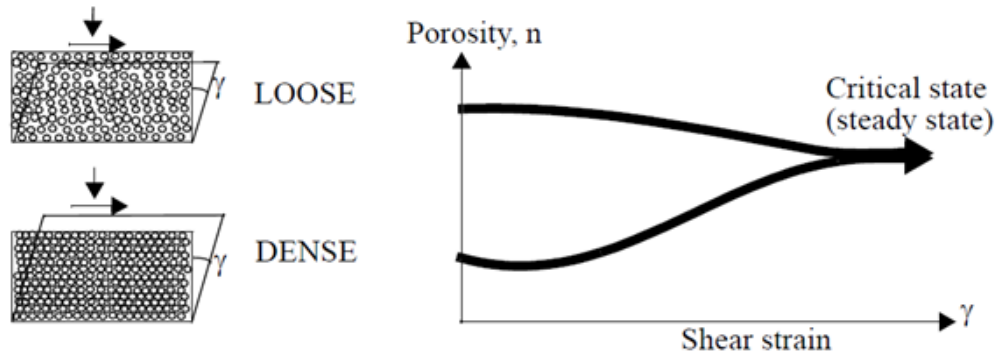
**Figure 2.13:** The definition of critical state. This figure describes how a loose sample contract until critical state, while a dense sample dilate until critical state is reached(Nordal, 2020).

The definition of the state parameter can be illustrated in Figure 2.14. The difference in void ratio, e, for a given mean stress, p is the state parameter, $\psi_{BJ}$. $e_0$ is the state point for the measured condition, and $e_{ss}$ is the void ratio on the critical state line for the same mean stress. The state parameter $\psi_{BJ}$ is defined by $e_0 - e_{ss}$. $\lambda_{ss}$ is the slope of the critical state line. The void ratio and stress are the primary state variables for soils, and the critical state line is, by definition, the locus of the critical state points in the void ratio vs stress space. Fabric is also an important state variable. Soil fabric is a term that describes the arrangement of sand grains on a particulate scale. This means a description of particle orientations, contacts and distribution (Been et al., 1991).
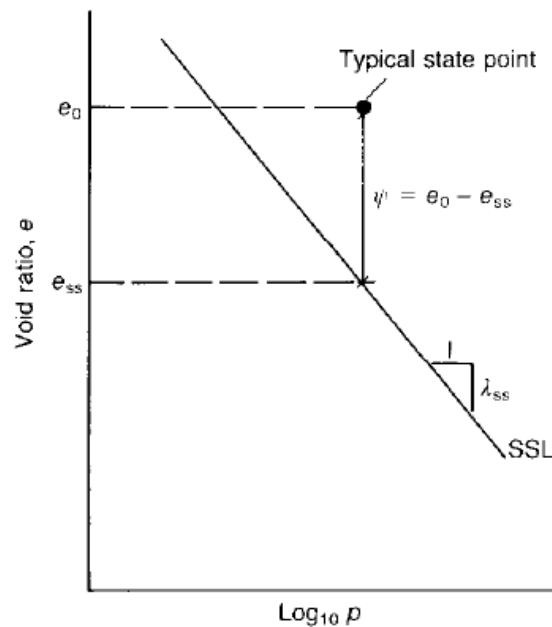


**Figure 2.14:** The definition of the state parameter. The difference in void ratio from a typical state point at $e_0$ and mean stress, p to the critical state line at $e_{ss}$ for the same mean stress p (Been et al., 1986).

### 2.2.3 Method for interpretation of state parameter from CPT

The relation between the cone tip resistance and the sand state has been determined by K. Been, J. H. A. Crooks, D. E. Becker and M. G. Jefferies in the paper "The cone penetration test in sands; part I, state parameter interpretation(Been et al., 1986). They used data from available chamber testing programs from different locations and countries. Parkin and Lunne (1982) have shown that chamber size and boundary conditions affect the cone resistance depending on the sand density. "Chamber size effects for loose sands (Dr <30%) are not significant, provided that the chamber-to-cone diameter ratio is greater than 20. For dense sands (Dr = 90%), the chamber-to-cone diameter ratio must be greater than about 50 to reduce the influence of chamber size in the test results"(Parkin and Lunne, 1982). The boundary effects are minimized when the chamber to cone ratio is larger than 50. The findings by Parkin and Lunne have been replotted by (Been et al., 1986), and the results are shown in Figure 2.15. Boundary condition one, BC1, represents the condition of constant stress in the lateral direction and boundary condition three, BC3, represents the condition of constant volume in the lateral direction. For chamber to cone diameter ratios of 50, one can see that BC1 and BC3 yield similar $q_c$ values.
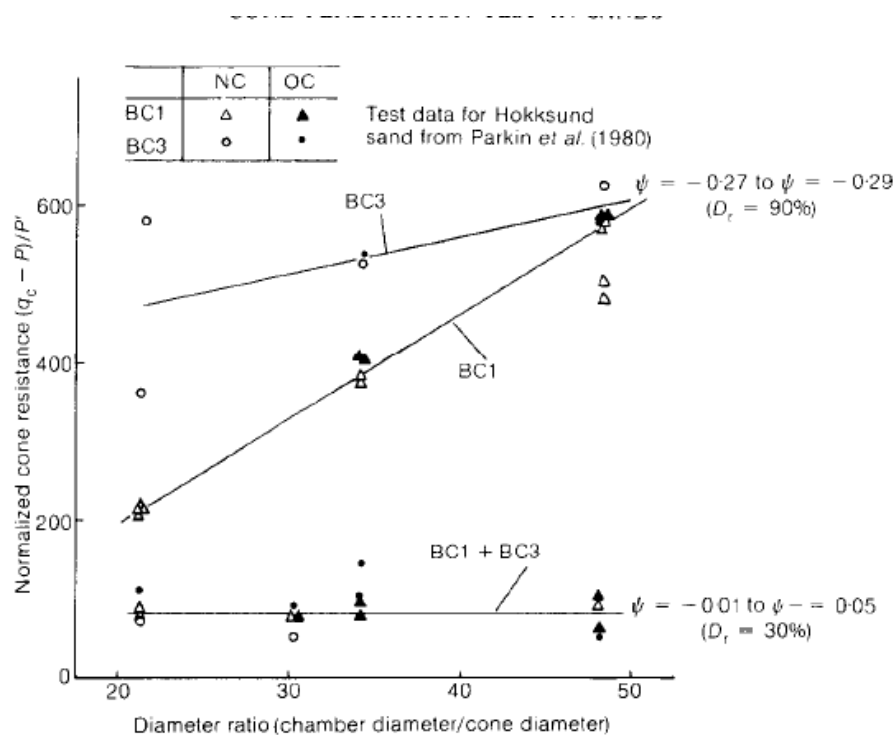


**Figure 2.15:** Chamber size effect. Two different test with different boundary conditions yield similar $q_c$ values for chamber-to-cone ratio of 50(Been et al., 1986).

The relationship between cone tip resistance and sand state is shown in Figure 2.16. Figure 2.16a is not adjusted for chamber size and boundary conditions, while Figure 2.16b is adjusted. The difference is that the linear contours for equal $\psi_{BJ}$ passes through the origin when the results are adjusted. Figure 2.16 indicates that $\psi_{BJ}$ can be expressed as a function of $q_c$, p and p'. This relationship is worked out

18

for monetary sand number 0. Index properties for Monterey no. 0 sand are presented in table 2.1.

$$f(\psi_{BJ}) = \frac{q_c - P}{P'} \tag{2.11}$$

| Property | Monterey no. 0 sand |
|---|---|
| $Medium grain size D_{50} : \mu m$ | 370 |
| $Effective grain size D_{10} : \mu m$ | 250 |
| $Uniformity coefficient \frac{D_{60}}{D_{10}}$ | 1,6 |
| $Percentage passing no. 200 sieve$ | 0 |
| Specific gravity of particles | 2,65 |
| Sphericity | 0,80 |
| Roundness | 0,35 |
| Maximum void ratio | 0,82 |
| Minimum void ratio | 0,54 |

**Table 2.1:** Index properties of Monterey no. 0 sand(Been et al., 1986).



**(a)**                                      **(b)**
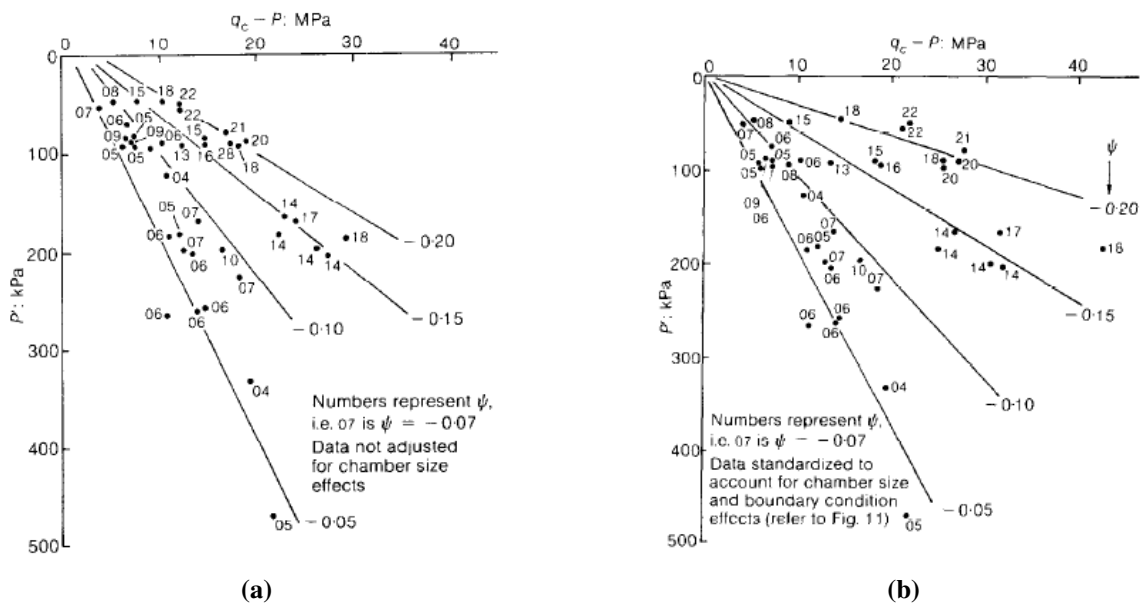
**Figure 2.16:** Relationship between cone tip resistance and sand state. Fig 2.16a: Results not adjusted for chamber size and boundary effects and the correlation lines do not go through the origin (Been et al., 1986). Fig. 3.3b: Results adjusted for chamber size and boundary effects and the correlation lines go through the origin.(Been et al., 1986)

A more general relationship between the state parameter, $\psi_{BJ}$ and the cone tip resistance $q_c$ is presented by (Been et al., 1987). The critical state lines for the different sands were determined using stress-

controlled, undrained triaxial testing techniques. A well-defined relationship between the behavioural properties of sands and $\psi_{BJ}$ exists. Void ratio and stress level can be described in terms of the state parameter $\psi_{BJ}$, as Been et al. (1986) have demonstrated. This relationship was demonstrated for Monterey sand no. 0. During cone penetration, great stresses occur under the cone. Because of this, the knowledge of the gradient of the critical state line must be known. The importance of the gradient of the critical state, $\lambda_{ss}$, can be explained with a simple example. Consider a small stress p' with a given void ratio of $e_0$. This gives a sand state at $\psi_{0BJ}$, which gives a friction angle, $\phi'$. Now consider the same sand with the same void ratio but greater stress. $\phi'$ will still relate to $\psi_{BJ}$, but now the state of the sand is quite different. The new greater stress has reduced the reference void ratio from which $\psi_{BJ}$ is measured. The reference void ratio is reduced proportionally to $\lambda_{ss}$. In Figure 2.17, the different critical state lines for the different sands are presented.
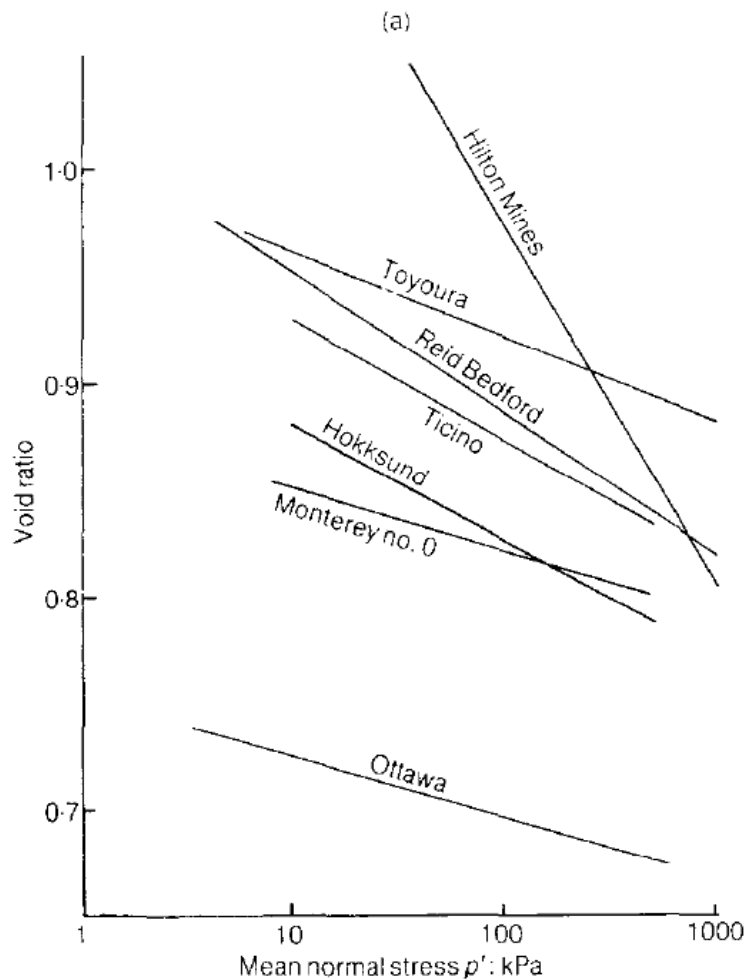


**Figure 2.17:** Critical state lines for the different sand (Been et al., 1987)

The database used to develop the state parameter concept is based on a triaxial test. One can wonder if such a database is relevant to CPT.

Hill (1950) noted that the symmetry of spherical cavity expansion made triaxial (uniaxial) testing directly relevant to the problem. Thus, $\phi' - \psi_{BJ}$ behaviours developed in triaxial testing should be directly applicable to the evaluation of the CPT on the assumption that $q_c$ versus $\psi_{BJ}$ relationships will have the same form as the spherical cavity expansion problem. This assumption does not imply the equivalence of the two problems (Hill, 1950).

To summarize this, the state parameter approach developed on the triaxial test database should be applicable to the evaluation of the CPT data. The relationship between $q_c$ and $\psi_{BJ}$ is based on the various sands presented in Figure 2.18. The relation can be expressed as in formula 2.12. k is the normalized $q_c$ value at $\psi_{BJ} = 0$, and m is the slope of the normalized $q_c - \psi_{BJ}$ relationship.

$$\frac{q_c - p}{p'} = ke^{-m\psi_{BJ}} \tag{2.12}$$
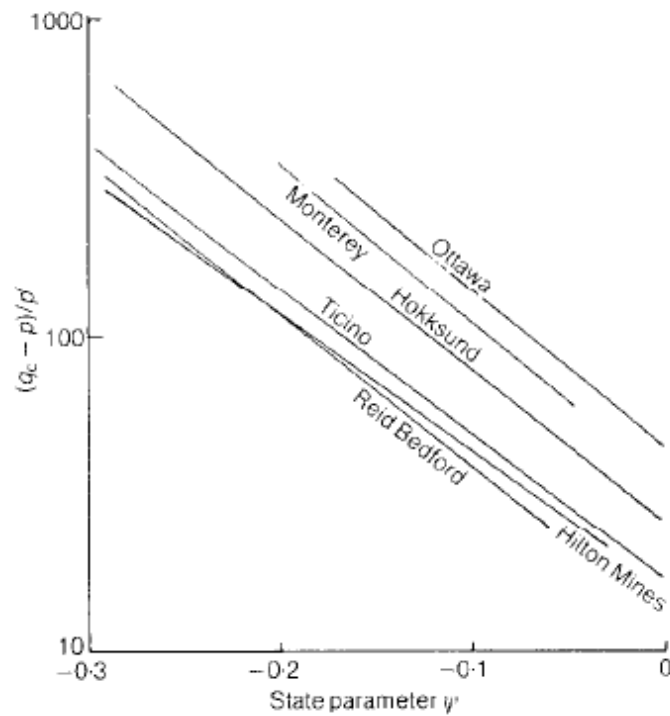


**Figure 2.18:** Relationship between $q_c$ and $\psi_{BJ}$ is based on various sands. The relation ship shown in this figure can be expressed by equation 2.12 (Been et al., 1987).

In Figure 2.19 are m plotted against $\lambda_{ss}$. There is a definite exponential relationship between the two quantities. The relation between the two quantities is used to develop a generalized cone interpretation framework. Expression 2.13 express this relationship.

21

$$m = 8, 1 - ln\lambda_{ss} \qquad\qquad (2.13)$$
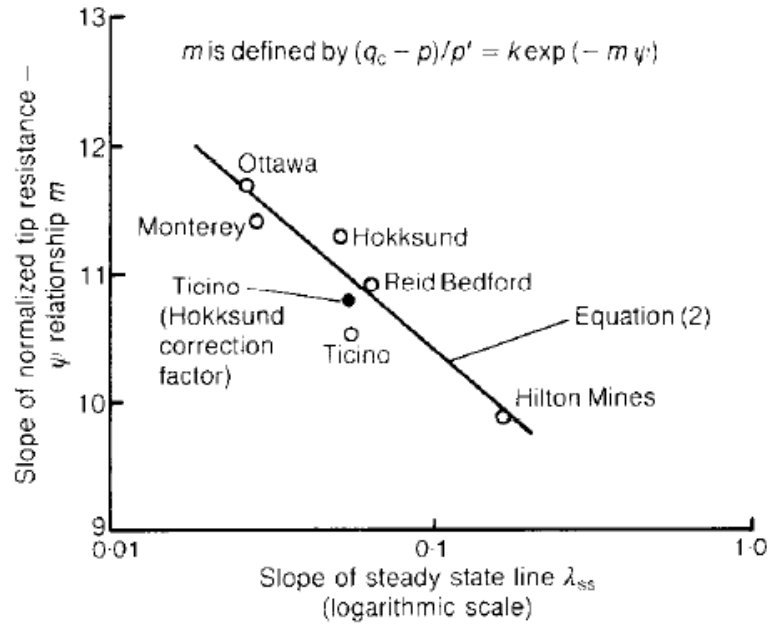


**Figure 2.19:** The slope of the normalized tip resistance - $\psi_{BJ}$ relationship, named m, is plotted against the slope of the critical state line, $\lambda_{ss}$. These two parameters are plotted against each other to get a correlation between the gradient m - $\psi_{BJ}$ relationship and $\lambda_{ss}$. (Been et al., 1987)

.

The value for k can only be positive for whatever values of $\psi_{BJ}$ and $\lambda_{ss}$; this is a physical requirement. Figure 2.20 shows a hyperbolic relationship between k and $\lambda_{ss}$, and because of the requirement of always a positive k, this should be a reasonable approximation to the data. Figure 2.20 can be represented by equation 2.14. Table 2.2 contains the data plotted in Figure 2.20

| Sand | k | m | $\lambda$ | Range of $\psi_{BJ}$ at a given p and $q_c$ |
|---|---|---|---|---|
| Monterey no. 0 | 35 | 11,4 | 0,029 | $\pm 0,02$ |
| Ticino (normally consolidated) | 17 | 10,5 | 0,056 | $\pm 0,040$ |
| Hokksund (normally consolidated) | 26 | 11,2 | 0,054 | $\pm 0,040$ |
| Ottawa | 42 | 11,7 | 0,028 | $\pm 0,025$ |
| Reid Bedford | 13 | 10,9 | 0,065 | $\pm 0,020$ |
| Hilton Mines | 16 | 9,9 | 0,170 | $\pm 0,040$ |

**Table 2.2:** Summary of normalized tip resistance-state parameter relationship (Been et al., 1987).

$$k = 8 + \frac{0,55}{\lambda_{ss} - 0,01} \tag{2.14}$$
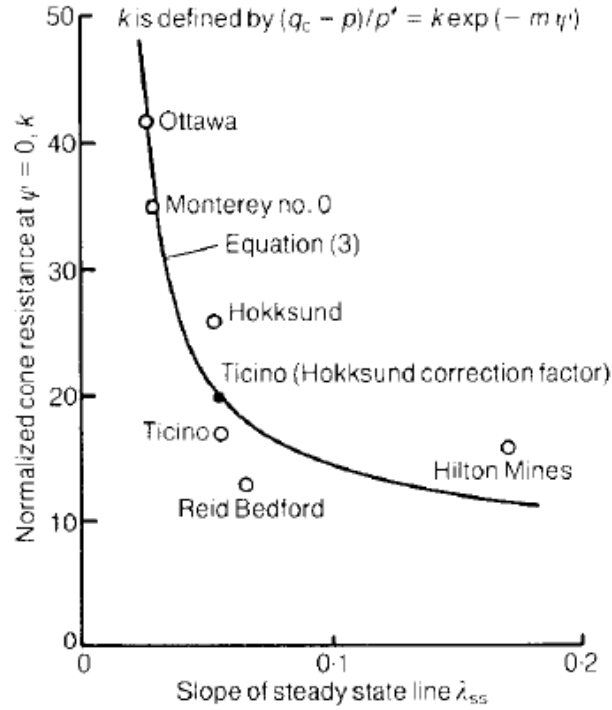


**Figure 2.20:** The normalized cone tip resistance at $\psi_{BJ} = 0$ is plotted against the slope of the critical state line for many different sands. This gives a correlation between the normalized cone tipresistiance at $\psi_{BJ} = 0$, named k and $\lambda_{ss}$. This correlation shown in this figure is expressed in equation 2.14 (Been et al., 1987)

.

Equation 2.15 is a combination of equation 2.12, 2.13 and 2.14 and gives a complete relationship for cone resistance in terms of the key factors controlling sand behaviour during shear, $\psi_{BJ}$ and $\lambda_{ss}$ (Been et al., 1987).

$$\frac{q_c - p}{p'} = (8 + \frac{0,55}{\lambda_{ss} - 0,01})e^{-(8,1-ln\lambda_{ss})\psi_{BJ}} \tag{2.15}$$

In practical use the state parameter $\psi_{BJ}$ will be the unknown and the measured $q_c$ will be known. The parameter $\lambda_{ss}$ needs to be estimated or measured independently. Test on reconstituted samples of the actual sand is necessary to determined $\lambda_{ss}$. The mean stress p may be estimated on the measured vertical stress and the estimated horizontal stress. The inverted form of equation 2.15 can be used to compute $\psi_{BJ}$ when $\lambda_{ss} and p$ are independently known, expressed in Equation 2.16.

$$\psi_{BJ} = -\frac{1}{(8,1 - ln\lambda ss)} * ln[\frac{q_c - p}{p'}(8 + \frac{0,55}{\lambda_{ss} - 0,01})^{-1}]$$ (2.16)

The state parameter approach seems to consider particle shape, varying mineralogy and difference in grain size. Some factors are neglected and can be taken into account for a more complete relationship. These factors are friction angle at steady state ($\phi'_{ss}$), stress history, constrained modulus $M_v$, shear modulus G, initial fabric, chamber size and boundary conditions Been et al. (1987).

## The NTH method (Effective stress based interpretation)

Janbu and Senneset developed an interpretation method for evaluating effective stress parameters for both drained and undrained conditions at the Norwegian Institute of Technology (now Norwegian university of science and technology, NTNU) in the 1970s and 1980s. Through a state-of-the-art study, Sandven (1990) presented an overview describing the NTH method. The theoretical solution is based on the classical bearing capacity theory, where soil is treated as a rigid plastic soil material under plane strain conditions. The bearing capacity of a foundation is defined as the maximum load the ground can sustain, and is based on the stress conditions in the soil under a foundation load. The net effective vertical foundation stress from the classical bearing capacity theory is expressed by equation 2.17 (Geoteknikk, 2020).

$$\sigma'_{vn} = (N_q - 1) \cdot (p' + a) + \frac{1}{2}\bar{\gamma}N_\gamma B_0$$ (2.17)

According to the bearing capacity theory, the bearing capacity failure occurs as a shear failure of the soil under the foundation. The failure mechanism consists of three zones; an active Rankine zone, a Prandtl zone that is the radial shear zone and a passive Rankine zone. The geometry is presented in figure 2.21.
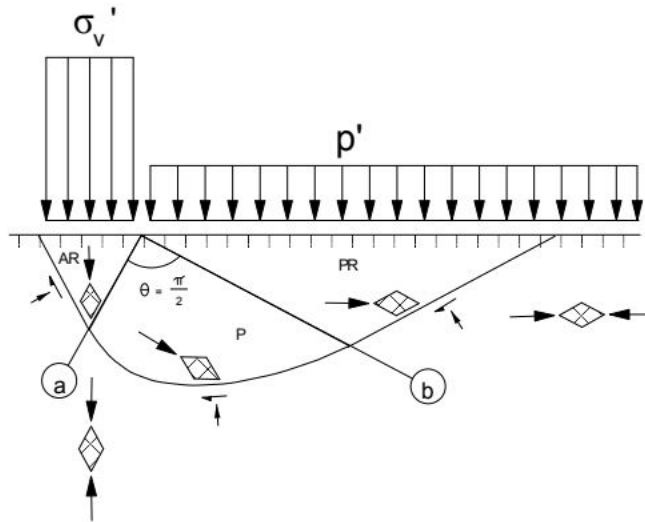
**Figure 2.21:** The stress field from bearing capacity theory of a shallow foundation. The geometry consists of an active Rankine zone, a radial Prandtl zone and a passive Rankine zone. The bearing capacity failure occurs as a shear failure of the soil under the foundation (Geoteknikk, 2020).

Janbu and Senneset suggested that the failure zone geometry that occurs around the advancing cone tip is based on the effective stress field from bearing capacity theory (Sandven, 1990). Figure 2.22 shows the idealized stress field around the cone based on the stress field from the bearing capacity theory. The NTH method introduces the plastification angle, $\beta$, which is an important parameter defining the size of the failure zone around the advancing cone.
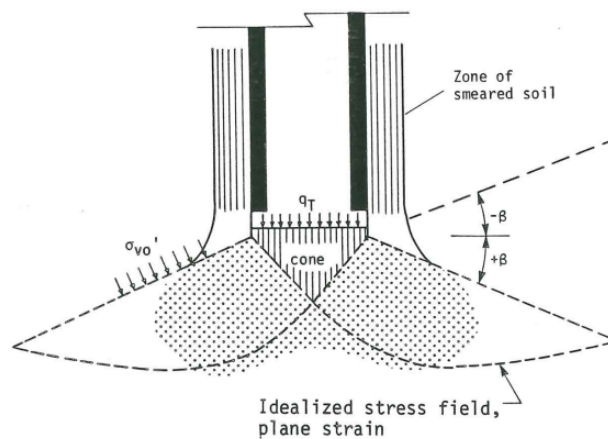


**Figure 2.22:** The idealized stress field around a penetrating cone applying the NTH-method. The stress field is based on the stress field from the classical bearing capacity theory with an active Rankine zone, Prandtl zone and a passive Rankine zone. This is the plastified zone, and the size of the plastified zone is limited by the plastification angle, $\beta$. The soil above the plastified zone will be compressed with the advancing cone. Illustration from Sandven (1990).

The resistance from cone penetration is described using the classical bearing capacity formulation expressed in 2.18, and the net cone resistance is given by equation 2.19 (Sandven, 1990).

$$q_c' + a = N_q \cdot (\sigma_{V0}' + a) \tag{2.18}$$

$$q_n' + a = (N_q - 1)(\sigma_{V0}' + a) \tag{2.19}$$

Where $N_q$ is the bearing capacity factor. The bearing capacity factor from classical bearing capacity formulation is given by equation 2.20

$$N_q = tan^2(45 + \frac{\phi}{2}) \cdot e^{\pi \cdot tan\phi} \tag{2.20}$$

Based on back-calculations from theoretical and experimental studies, the bearing capacity factor has been modified to be applicable for CPT conditions (Sandven, 1990). The bearing capacity factor adjusted for plastification angle $\beta$ is expressed by equation 2.21. $N_q$ varies with friction $tan\phi$ and plastification angle $\beta$.

$$N_q = tan^2(45 + \frac{\phi}{2}) \cdot e^{(\pi - 2\beta) \cdot tan\phi} \tag{2.21}$$
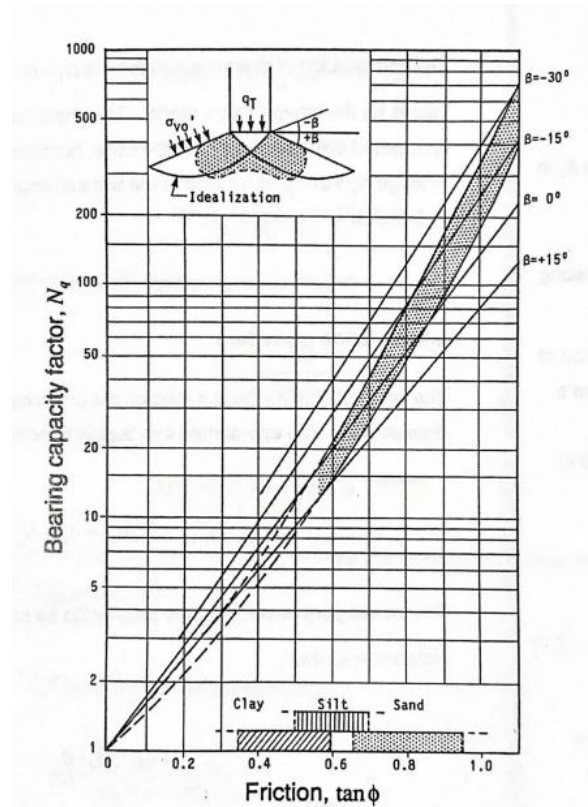
**Figure 2.23:** Experience-based values of the bearing capacity factor, $N_q$, as a function of plastification angle, $\beta$ and friction angle $\phi$. From Sandven (1990).

Figure 2.23 shows the correlation between the bearing capacity factor $N_q$ and friction $tan\phi$ and plastification angle $\beta$, based on experience. The NTH-method further introduces the cone resistance number, $N_m$ as:

$$N_m = \frac{N_q - 1}{1 + N_u \cdot B_q} \tag{2.22}$$

To interpret the friction $tan\phi$ using the NTH-method, an estimation of plastification angle $\beta$ is required. Sandven (1990) found through his study that $\beta$ could be correlated to the net cone resistance, $q_n$, excess pore pressure, $\Delta u_T$, sensitivity $S_t$ and overconsolidation ratio (OCR). However, the angle of plastification is challenging to determine, since there does not exists a unique relationship between $\beta$ and other relevant parameters. Sandven et al. (1988) suggested choosing values for the plastification angle, $\beta$ from tentative ranges based on the different soil types as presented in table 2.3. However, Lunne et al. (1997) stated that a lot of uncertainties are associated with these $\beta$-value.

**Table 2.3:** Tentative values for plastification angle $\beta$ for different soil types suggested by Sandven et al. (1988). Adapted from Lunne et al. (1997).

| Soil type | Tentative $\beta$-values |
|---|---|
| Dense sand overconsolidated silts, high-plasticity clays, low-compressible overconsolidated clays | $-20^o\, to -10^o$ |
| Medium sands and silts, sensitive clays, high-compressible clays | $-5^o\, to +5^o$ |
| Loose silts, clayey silts | $+10^o\, to +20^o$ |

From assuming an appropriate plastification angle, the friction $tan\phi$ for the soil could be determined from the correlation with pore pressure ratio, $B_q$ and cone resistance number $N_m$. Figure 2.24 shows the interpretation chart for plastification angle $\beta = -15^o$. The example in showing the determination of the friction at $tan\phi = 0.6$ from a cone resistance number $N_m = 5$ and pore pressure ratio $B_q = 0.6$.
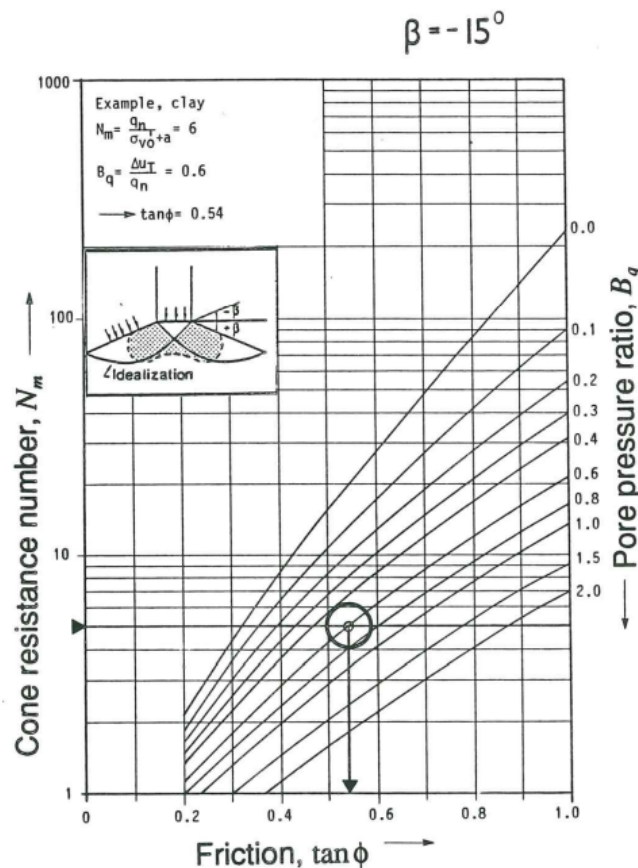


**Figure 2.24:** Interpretation chart for determining $tan\phi$ from cone resistance number $N_m$ and pore pressure ratio, $B_q$ based on assumed plastification angle $\beta = -15^O$. Example showing determination of $tan\phi = 0.6$ from cone resistance number $N_m = 5$ and pore pressure ratio, $B_q = 0.6$. (Sandven, 1990).

Paul Mayne has done a lot of research on the NTH method and presented a modified NTH method in clay accounting for the stress history of the soil material (Ouyang and Mayne, 2019). During a discussion session at the NGTS symposium in 2019, he suggested that for sand the plastification field in terms of the plastification angle could be dependent on the relative density (Paul Mayne, 2-14th June 2019). This idea gave motivation for and inspired the current study. In the original NTH method the plastification angle is anchored in theory of rigid plasticity but in practice used as a pragmatic empirical factor. The theory is conceptually derived for a plane strain rigid plasticity stress field, while it is applied in axisymmetric conditions. This illustrates the pragmatism of the parameter. Still, experience has shown that using the plastification angle as a parameter makes sense. A better assessment of this parameter could improve the understanding of the plastified zones around the cone tip possibly by coupling it more to relative density and critical state / steady state theory. Such an approach may hopefully give a broader understanding of why using plastification angle is a useful concept. The plastification angle will therefore be further investigated in this study.

## 2.3 Elasto-plasticity

### 2.3.1 Plastic strains

In Elasto-plasticity theory strains are divided into two components, elastic strains $\epsilon^e$ and plastic strains $\epsilon^p$. Elastic strains are by definition reversible and plastic strains are not. Strains are elastic as long as the stress state is below the failure surface in linear elastic perfectly plastic soil models. If the stress state crosses the failure surface plastic strains occurs. In more advanced soil models one may have plastic strains before the stress state crosses the failure surface and this is controlled by the degree of mobilization. A linear elastic perfectly plastic soil model is illustrated in Figure 2.25 Nordal (2020).
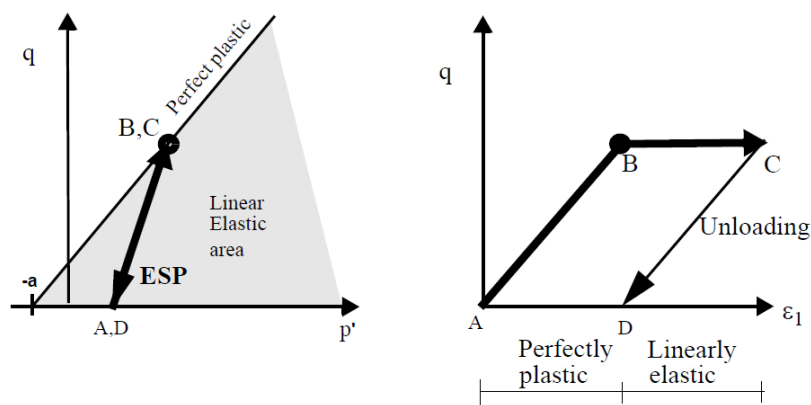


**Figure 2.25:** A visualization of a linear elastic perfectly plastic soil model. The grey area represent elastic behaviour of the material. When applying a stress component perpendicular to the failure criteria line, the stress is reduced back to failure criteria and plastic strains occur Nordal (2020).

The grey area in Figure 2.25 is the elastic region and is delimited by the failure criteria. A stress increment inside this grey area will give a stress increment according to Hookes law. If one try to apply a stress increment that crosses the failure line the material is not able to take the stress and the stress is forced back to the failure line and plastic strains occurs. The flow rule describes how the plastic strains develop when the stress level is tried increased above the failure limit. The concept of the flow rule is presented in Figure 2.26. The stress increment is denoted $d\vec{\sigma}'$. If one try to load above the failure surface with $d\vec{\sigma}'$, one get two components $d\vec{\sigma}'^{P}$ and $d\vec{\sigma}'^{e}$. The material is very sensitive to $d\vec{\sigma}'^{P}$ because it is the critical loading component with respect to crossing the failure surface. This component is perpendicular to the failure surface and is called the plasifying stress increment. The elastic component is tangential to the failure surface and thus in the direction of the boundary of the elastic domain. At failure the material can not take any more stress and when applying more stress one get plastic strains and the plastyfing stress becomes zero. In more advanced models $d\vec{\sigma}'^{P}$ will push the yield surface towards the ultimate yield surface. At the yield surface $d\vec{\sigma}'^{P}$ is not necessarily zero. $d\vec{\sigma}'^{P}$ will have two components $\sigma_1'$ and $\sigma_3'$ and the ratio between them is N as shown in Fiugre 2.26 Nordal (2020).
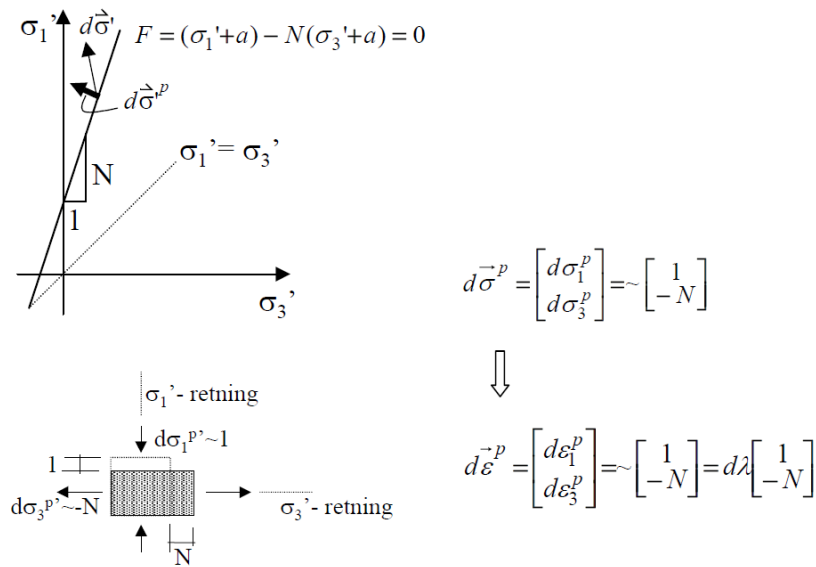


**Figure 2.26:** The concept of the flow rule. This concept is the associated flow rule. N is the ratio between the two components $\sigma_1'$ and $\sigma_3'$, which is the two components of the plastifying stress at the yield surface. Nordal (2020).

A plastic strain proportional to the plastifying stress increment is denoted associated flow. The plastic strains may in such a case be considered to be in the direction of $d\vec{\sigma}'^{P}$ in the stress space. This actually means that the "direction of the plastic strain increment" is defined by normality to the failure surface Nordal (2020).

The partial-derivatives of the failure or the yield criteria, $F = 0$ gives the failure surface gradients which

defines the surface normal. This is the flow rule for associated flow and it is expressed in equation 2.23.

$$d\vec{\epsilon^p} = \begin{bmatrix} d\epsilon_1^p \\ d\epsilon_3^p \end{bmatrix} = d\lambda \begin{bmatrix} 1 \\ -N \end{bmatrix} = d\lambda \begin{bmatrix} \frac{\delta F}{\delta \sigma_1'} \\ \frac{\delta F}{\delta \sigma_3'} \end{bmatrix} \tag{2.23}$$

In laboratory tests the plastic strain may be measured.The results and as shown in Figure 2.27 the lateral expansion is normally less than what the associated flow rule gives. A non-associated flow rule is introduced to adjust the theory. As shown in Figure 2.27 a potential surface Q is introduced and a non-associated flow rule can be worked out form this figure Nordal (2020). The non-associated flow rule is given in equation 2.24.
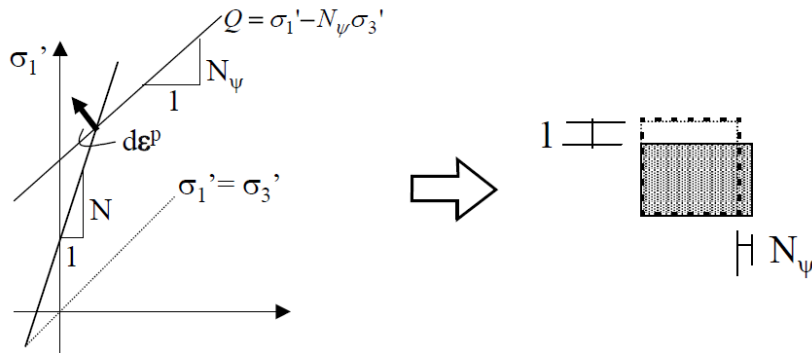


**Figure 2.27:** The concept of the non-associated flow rule, here is the potential surface Q added in the figure Nordal (2020).

$$d\vec{\epsilon^p} = \begin{bmatrix} d\epsilon_1^p \\ d\epsilon_3^p \end{bmatrix} = d\lambda \begin{bmatrix} 1 \\ -N_\psi \end{bmatrix} = d\lambda \begin{bmatrix} \frac{\delta Q}{\delta \sigma_1'} \\ \frac{\delta Q}{\delta \sigma_3'} \end{bmatrix} \tag{2.24}$$

As shown in Figure 2.28, the plastic flow rule describes volumetric strain versus vertical strain. Figure 2.28 is a standard drained triaxial test and thus one could find the angle of dilatancy, $\psi$ from the inclination of the $\epsilon_v - \epsilon_1$ -curve. The dilatacy angle is further explained in the following Chapter 2.3.2.
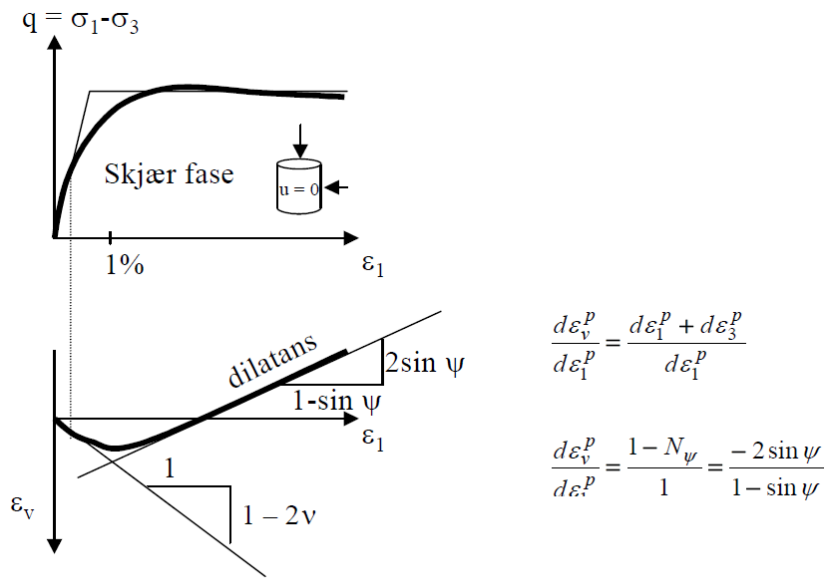
**Figure 2.28:** Dilatancy angle comes out from a drained triaxial test ran with relevant porosity and stress level Nordal (2020).

## 2.3.2 The dilatancy angle

The dilatancy angle is a parameter to describe the volumetric expansion or contraction when a soil material is exposed for shear strain. A densely packed material can be explained by densely packed spheres. When the spheres are laying in between each other and shear strain causes the spheres to move, they have to move on and against each other. The densely packed spheres starts to climb on each other and the loose packed spheres fall in between each other. That causes the densely packed material to dilate and the loose packed material to contract. This concept is shown in Figure 2.29. The same phenomena can be described by a saw teeth analogy. If one push two blades with saw teeth against each other as shown i Figure 2.30a, they will climb on each other. Figure 2.30b shows that the angle of the saw teeth is the dilatancy angle. The inner friction as it is named in Figure 2.30 is from now named the critical state friction $\phi_{cs}$, and it is the friction along the saw tooth surface. The sum of the critical state friction and the dilatancy angle is the external friction of the material Nordal (2020). There is two parameters in this thesis, that are denoted with $\psi$ and it is very important to not mix these two parameters, therefor a short repetition of the notation. The dilatancy angle is as describe in this chapter. The state parameter, which is denoted with $\psi_{BJ}$ is the difference in void ratio from the current state to the critical state as described in Chapter 2.2.2.
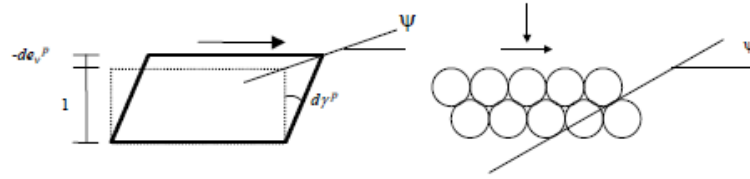
**Figure 2.29:** A visualization of the dilatancy angle. Densely packed grains climb on each other. In this two dimensional case the dilatancy is higher than in a three dimensional case, where the grains can move more freely. (Nordal, 2020)

.



| (a) | (b) |
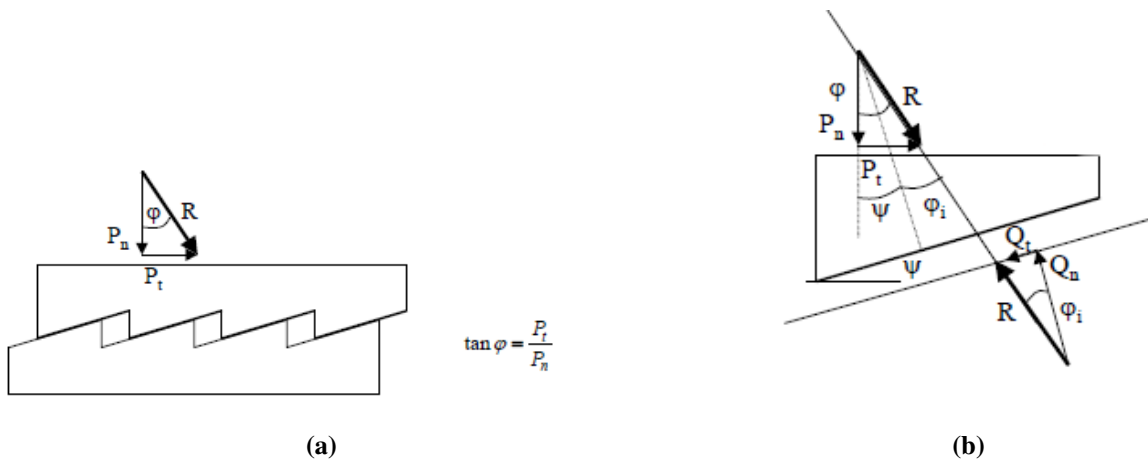
**Figure 2.30:** The definition of the dilatancy angle $\psi$ and the critical state friction angle $\phi_{cs}$ is presented in this figure. The dilatancy angle is the inclination of the saw tooth and the critical state friction angle is the friction on the saw tooth surface. The external friction $\phi$ is the sum of $\psi$ and $\phi_{cs}$ (Nordal, 2020)

.

Quarts sand has a critical state friction of $30^o$ and $30^o$ are often used for other materials as well Nordal (2020). Figure 2.30 gives the equation for critical state friction and is presented in equation 2.26. According to equation 2.25 the dilatancy angle will then be the external friction minus the critical state friction. Equation 2.25 is given by Figure 2.30.

$$\psi = \phi - \phi_{cs} \tag{2.25}$$

$$tan\phi_{cs} = \frac{Q_t}{Q_n} \tag{2.26}$$

Normally the dilatancy angle is much smaller than the angle of friction and because of this a non-associated flow is more realistic than associated flow. The dilatancy angle is very small and it could

be hard to determined, often it is set to zero. This causes an inaccuracy and if possible this parameter should be determine. Negative values of $\psi$ appears in loosely packed materials like sensitive and quick clays. Positive values of $\psi$ appears for example in densely packed sands Nordal (2020).

This theory works fairly well in cases with free surfaces. Under the advancing cone during cone penetration the component from the surrounding soil needs to be taken into account. The way of doing this is the plasticity angle $\beta$, which also can be expressed by the state parameter $\psi_{BJ}$. Thus, there is three soil parameters describing the soil behaviour. The critical state friction $\phi_{cs}$, the dilatancy angle $\psi$ and the angle of plasticity $\beta$ or the state parameter $\psi_{BJ}$.

## 2.4 Triaxial testing and critical state line from triaxial testing

By the definition of state parameter, information about the critical state line is required to investigate the state parameter for the sand. For sand, a critical state point is determined by running stress-controlled CIU triaxial test run until liquefaction occurs. Been and Jefferies (1985) suggested running a series of 5-10 triaxial tests at different void ratios and stress levels following the method described by Castro (1969) to obtain multiple critical state points and hence determining the critical state line.

However, to determine the critical state line, information about the slope of the critical state line, $\lambda_{ss}$ and a single point on the critical state line is required. It could be argued that the slope of the critical state line, $\lambda_{ss}$ found through triaxial testing, could correspond to the $\lambda$ achieved from oedometer tests, which is the inclination of the of the normally consolidated region of a $v-ln(\sigma')$-space. This is further explained in the following section.

**Oedometer modulus**

In Norway the modulus in the over consolidated region is normally used as a constant and linear in the normally consolidated region. In the Cam Clay model a linear modulus is used both in the normally and over consolidated region. The linear modulus curve through origin and this means that the stress strain curves are logarithmic. If one redraw the curve in a $ln\sigma'$ plot, the curve become straight lines and the inclination in the over consolidated region is $\kappa$ and in the normally consolidated region is $\lambda$, see Figure 2.31 (Nordal, 2020).
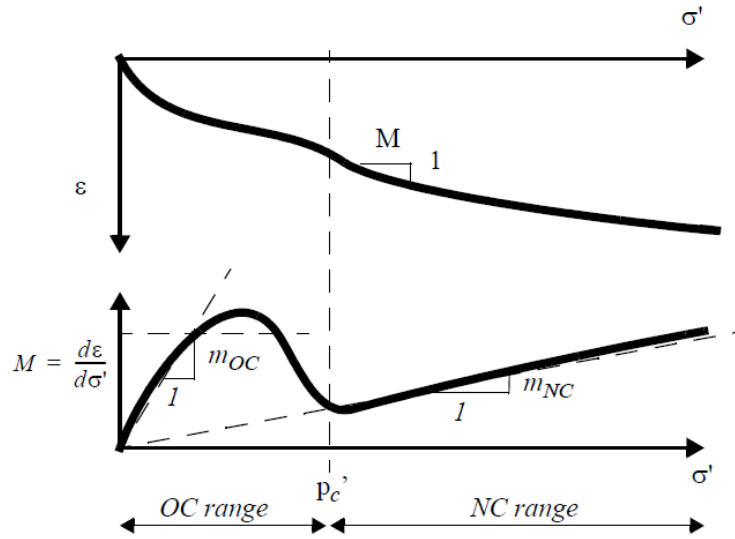
**(a)** The oedometer modulus defined by Janbu (1963) Nordal (2020).
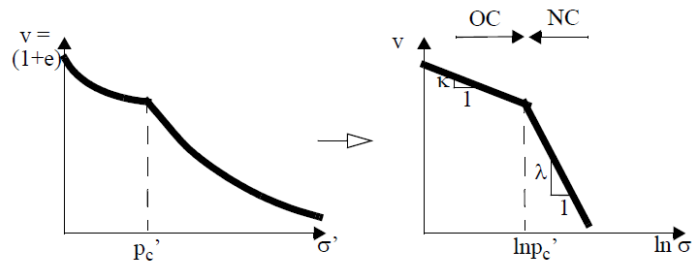


**(b)** The flexibility parameters $\lambda$ and $\kappa$ (Nordal, 2020).

**Figure 2.31**

The vertical strain in an oedometer is the same as the volumetric strain. Therefor can the vertical axis easily be converted to a volumetric measure. Here the specific volume, $v$ is used on the vertical axis. $v = 1 + e$ and e is the classical void ratio. The advantages of using $v$ is because it converts easily to volumetric strain, $\epsilon_p$. Below the formulas are presented (Nordal, 2020).

$$v = 1 + e = \frac{volume\,of\,pores + volume\,of\,solids}{volume\,of\,solids} = \frac{V_p + V_s}{V_s} \tag{2.27}$$

$$d\epsilon_p = \frac{-dV}{V} = \frac{dV_p}{V_p + V_s} = \frac{d(V_p + V_s)/V_s}{(V_p + V_s)/V_s} = -\frac{dv}{v} \tag{2.28}$$

The straight lines in the $v - ln\sigma'$ diagram gives the formulas 2.29 and 2.30. See Figure 2.31b.

$$OC\,range : \Delta v = -\kappa \Delta \ln \sigma' = -\kappa \ln \frac{\sigma'}{\sigma'_0} \tag{2.29}$$

$$NCrange: \Delta v = -\lambda \Delta \ln \sigma' = -\lambda \ln \frac{\sigma'}{\sigma'_0} \qquad (2.30)$$

From equation 2.29 and equation 2.30 one can see that loading from $\sigma'_0$ to $\sigma'$ one get a change in specific volume equal to $\Delta v$. $m_{NC}$ which is the Janbu modulus in the NC range will in the same way give a change in vertical or volumetric strain (Nordal, 2020).

$$\Delta \epsilon = \Delta \epsilon_p = \frac{1}{m_{NC}} \frac{\sigma'}{\sigma'_0} \qquad (2.31)$$

By comparing equation 2.30 and 2.31 and using equation 2.28 the result becomes:

$$\lambda = \frac{v}{m_{NC}} = \frac{1+e}{m_{NC}} \qquad (2.32)$$

The relationships of equation 2.28 to equation 2.32 are valid for oedometer compression test and isotropic compression test (triaxial) and the parameters $m_{NC}$ and $\lambda$ will be more or less the same for the two tests. This is confirmed by a study of comparing oedometer compression curves and isotropic compression curves Nordal (2020). Applying this theory, the critical state line could therefore be determined through one single triaxial test in addition to an oedometer test.

## 2.5 Chamber testing

Cone penetration tests are often used where it is hard to get undisturbed samples. The complex mechanism of a continuous cone penetration in a soil material is very difficult to model theoretically. To get engineering parameters the interpretation of CPTU results are based on theoretical relations modified with empirical data or only empirical relationships. A lot of calibration chamber testing have been conducted through out the years and data sets of soil parameters and CPTU results for several sand types have been presented. NGI carried out a large amount of laboratory calibration tests on large sand samples from 1975 to 1977. Other countries like Australia, Florida in the USA and Italy have done similar investigations.The aim of the study at NGI was to establish correlations between cone resistance and sand strength and deformation characteristics for different sand densities and stress states, in addition to evaluate the effects of the chamber boundary condition and chamber size on the measured cone resistance. The program at NGI included around 90 tests and some of the results are listed in table 2.4 (Lunne and Christoffersen, 1983).

| Calibration Chamber | | | | | | | | Triaxial compression |
|---|---|---|---|---|---|---|---|---|
| Dr [%] | $K_0$ | BC | $R_d$ | $q_c[MN/m^2]$ | $q_c^*[MN/m^2]$ | $N_q$ | $M_0[MN/m^2]$ | $\phi_{peak}$ [°] |
| 22 | 0,41 | 1 | 34.2 | 2.7 | 2.7 | 54 | 18.3 | 35.1 |
| 33 | 0.45 | 1 | 34.2 | 2.3 | 2.3 | 46 | 20.3 | 36.8 |
| 59 | 0.37 | 3 | 21.4 | 9.4 | 10.8 | 216 | 41.9 | 40.9 |
| 59 | 0.37 | 1 | 30.2 | 8.0 | 9.6 | 252 | 41.9 | 40.9 |
| 79 | 0.33 | 1 | 21.4 | 7.9 | 15.6 | 312 | 57.9 | 44.0 |
| 23 | 0.84 | 3 | 48.3 | 2.7 | 2.7 | 54 | 151.0 | 35.3 |
| 58 | 0.76 | 1 | 30.2 | 12.0 | 15.0 | 300 | 225.0 | 40.7 |
| 90 | 0.85 | 3 | 48.3 | 30.6 | 30.6 | 612 | 221.0 | 45.7 |
| 93 | 0.86 | 3 | 34.2 | 23.7 | 29.4 | 588 | 256.0 | 46.2 |

**Table 2.4:** Data from NGI calibration chamber tests and drained triaxial compression tests. $D_r$ = relative density $K_0$ = stress ratio BC = boundary condition; 1: $\sigma_v'$ = constant, $\sigma_h'$ = constant, 3: $\sigma_v'$ = constant, $\epsilon_h = 0$ $R_d$ = chamber diameter/cone diameter $q_c$ = measured cone resistance $q_c^*$ = measured resistance multiplied with a correction factor to account for effects of diameter ratio $N_q$ = bearing capacity factor $M_0$ = constrained deformation modulus and $\phi_{peak}$ = peak drained friction angle from triaxial compression test.

Several others have tested how chamber size and boundary conditions effect cone resistance in chambers. As mentioned in Chapter 2.2.3, the chamber-to-cone diameter ratio for loose sands must be greater than 20 and for very dense sands, greater than 50. Paul W. Mayne and Fred H. Kulhawy used 24 sets of CPT data in sand to evaluate general cone relationships. They developed an simple, general relationship to correct the measured $q_c$ for boundary effects with flexible wall. This relationship includes the relative density of the sand and the chamber-to-cone diameter ratio.

> This relationship allows for a consistent comparison of equivalent "free filed" data regardless of the data source (Mayne, 1991).

All the samples in this study were reconstituted sands that were unaged and uncemented. The void ratio varied between 0,4 to 1,05. Most of the test specimens were consolidated under $K_0$ conditions, while some were consolidated under general anisotropic conditions prior to testing. The mean $K_0$ for the normally consolidated specimens tested under $K_0$ and anisotropically consolidated conditions was 0,43. Most of the tests were conducted with a standard 35,7 mm diameter cone, but the cone diameter varied from 9,5 mm to 50,0mm. The relation developed in the study by (Mayne, 1991) is presented in equation 2.33 (Mayne, 1991). This formula increase the measured cone resistance, because the wall are flexible and will be less stiff than soil. In this project the chamber wall are made of concrete, which makes the boundary stiffer than soil, therefor the measured cone resistance will be higher than free field conditions. Formula 2.33 is not used in this work.

$$q_{c,corrected} = q_{c,measured} * \left[ \frac{(B_c/B) - 1}{70} \right]^{\frac{-D_r(\%)}{200}} \tag{2.33}$$

$\frac{B_c}{B}$ is the chamber-to-cone diameter ratio and $D_r$ is the relative density in percent. When the chamber-to-cone diameter ratio is 71, equation 2.33 assume no boundary effect. The research done by Parkin and Lunne (Parkin and Lunne, 1982) conclude that for dense normally consolidated sand, minimum chamber-to-cone diameter ratio of 50 was applicable for a very dense samlpe, $Dr = 90\%$ and chamber-to-cone diameter ratio of 20 for $Dr = 30\%$. The chamber-to-cone diameter ratio in this research project is $33, 6$ and average Dr for the the densest experiment is 45%. Figure 2.32 show a point from experiment M2 and section 3c which is average relative density against $\frac{B_c}{B}$. This shows that the chamber-to-cone diameter ratio is larger than what is needed for free field conditions.
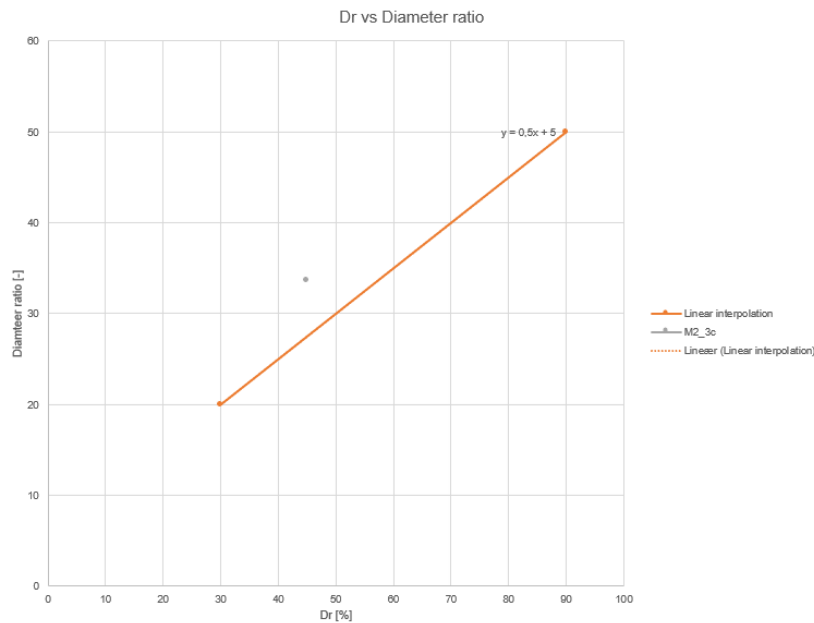


**Figure 2.32:** The research done by Parkin and Lunne (Parkin and Lunne, 1982) conclude that for dense normally consolidated sand, minimum chamber-to-cone diameter ratio of 50 was applicable for a very dense samlpe, $Dr = 90\%$ and chamber-to-cone diameter ratio of 20 for $Dr = 30\%$. In this Figure a line is interpolated between the two points. $\frac{Bc}{B}$ vs average Dr for experiment M2 and section 3c is plotted as the grey point.

### 2.5.1 Silo effect, Janssens formula

The horizontal stresses caused by the weight of the sand and the extra simulated earth pressure and the friction between the wall and the sand leads to a reduced earth pressure with depth. This effect is called the silo effect and is presented by Janssen in 1895 (Jansscn, 1895). The chamber size and the silo effect, affect the measured results from the CPT as well as the chamber height and material height. Increased material height leads to increased stresses and silo effect. The formula presented by (Jansscn, 1895) for vertical stress for dry granular material in a silo is shown below.

$$\sigma_v = \gamma * l(1 - e^{-\frac{z}{l}}) \tag{2.34}$$

$\gamma$ is dry unit weight, l is the decay length and z is the depth from the surface of the granular material. The maximum vertical stress accumulated in the silo, according to the equation 2.34, is $\gamma * l$. According to (Hammer, 2020), the decay length was defined by J. Duran in 2000 as

$$l = \frac{D_c}{4 * K * tan(\delta)} \tag{2.35}$$

Where K is the earth pressure coefficient, $D_c$ is the diameter of the chamber, $tan(tan_\delta)$ is the friction between the granular material and the chamber wall and $\delta$ is the friction angle of the interface. The soil used in these experiments is fully saturated and one assumption is made. The effective stress is the only component affected by the silo effect. The water pressure is hydro-static and the water level is at the same level as the top of the soil. Formula 2.34 is still used with the effective weight of the material $\gamma'$. This gives the updated formula 2.37

$$\gamma' = \gamma - \gamma_{water} \tag{2.36}$$

$$\sigma_v = \gamma' * l(1 - e^{-\frac{z}{l}}) + \gamma_{water} * z \tag{2.37}$$

This estimation of the stress level were used by (Hammer, 2020) and (Skrede, 2021) and will also be used in this study. The extra applied earth pressure is taken into account by the formula 2.38. The extra vertical effective stress is called $\Delta\sigma'_v$.

$$\Delta\sigma'_v(z) = \Delta\sigma'_{v1} * e^{-\frac{z}{l}} \tag{2.38}$$

## 2.6 Material point method

### 2.6.1 Modelling of large deformation problems with generalized interpolation Material Point Method

The modelling of large deformation like a CPTU penetration, can be done by using the Material Point Method including strain-rate effects. This numerical method is of great interest in geotechnical engineering because of the possibility to model large deformations like landslides. The Generalized Interpolation Material Point Method (GIMP) is the method used in this thesis. The method is an evolution of the original Material Point Method by (Sulsky et al., 1994). The Material Point method simulate material behaviour similar to the Finite Element Method, described by a continuum mechanics. The material is discretised by material points as shown in Figure 2.33b. The information required for the simulation is stored in these points. The simulation is run in time steps. The data from the material

points is transferred to the background grid in the beginning of the time step. This is where the balance equations are solved. The material variables are then updated and interpolated back to the material points. The initial configuration of the grid is normally reset at the end of the time step. While the Finite Element Method application is limited due to the mesh distortion, the Material Point Method is viewed as a meshfree method. This makes the Material Point Method well-suited to solve large dynamic displacement problems(Tran and Sołowski, 2019). Numerical instabilities and grid-crossing instability are instability problems in the original MPM. Discontinuous gradient of the shape functions is one of the problems causing instability. A sudden change of the stress, caused by the discontinuity in the shape function, occurs when the material point crosses to a new cell. Algorithmic errors like this are reduced in the newer formulations of the MPM, like the Generalized Interpolation Material Point Method(Tran and Sołowski, 2019). The parameter $\beta$ is difficult to determined and it is an important variable in the NTH-method. The study of the strain field around the tip of the cone together with the physical experiments conducted could give a better understanding of the $\beta$ value and make a relation to the well defined stat parameter $\psi_{BJ}$.
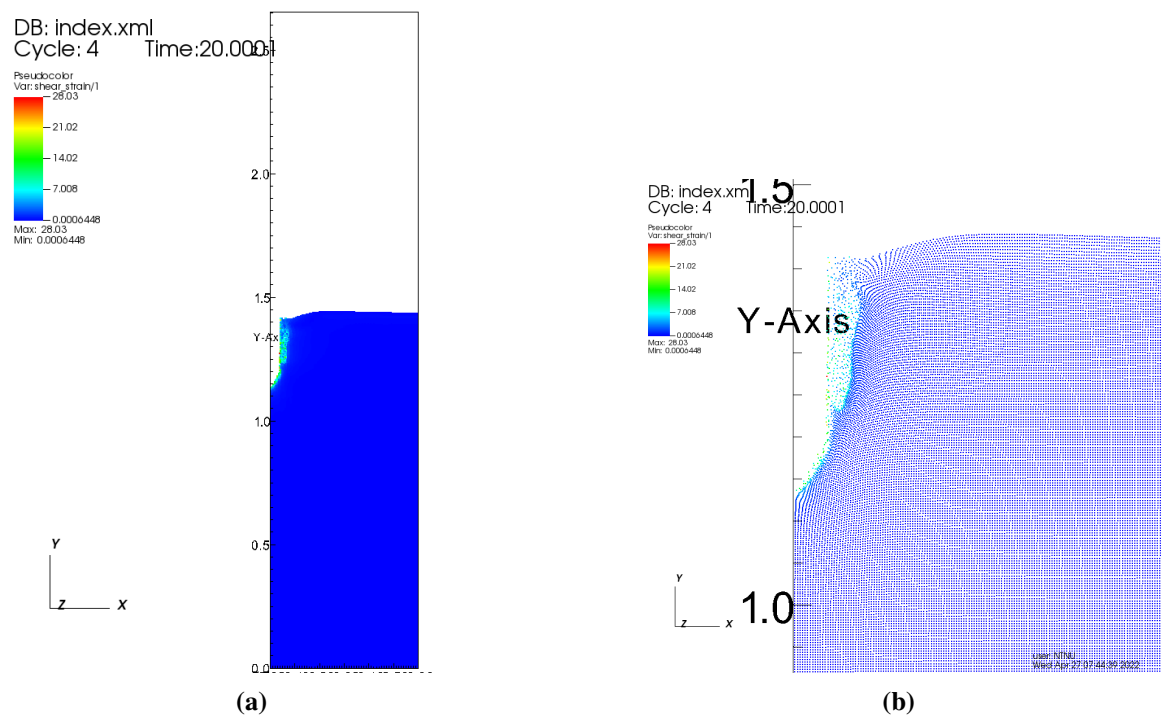


**Figure 2.33:** (a) The model used for the Material Point Method. The model is axis symmetric. The blue points are the soil and the white part, in the soil, along the Y-axis is the cone. (b) The blue points are the material points that containes the information required for the simulation.

# Chapter 3

# Method

To learn more about the soil behaviour around the cone tip during cone penetration, three physical experiments with CPTU were conducted in sand. This chapter covers the methodology related to the experiments and the investigation of the sand behaviour during cone penetration. The chapter will be divided into the methodology related to the physical laboratory set-up, CPTU equipment and procedures, and the determination of sand material properties, including supplementary tests such as oedometer and triaxial testing and the laboratory procedures in terms of sample construction and excavation. In addition, the methods for analysing the stress field around the advancing cone and numerical analysis using the Material point method are presented.

## 3.1   Previous work

This study is a continuation of the work performed by Hammer (2020) and Skrede (2021). The methodology surrounding the laboratory and experimental set-up has been developed and used by Hammer and Skrede. They presented different ways of constructing the sample, and through their studies, described their experience. The method and the laboratory procedures used in this study will be based on the methods developed by Hammer (2020) and Skrede (2021) or an adaption of these procedures.

A preliminary project was performed during the fall semester of 2021 in connection with the subject TBA4510 Geotechnical Engineering, Specialization Project at NTNU. Through this project, two CPTU-tests in a large scale chamber were performed with the aim of establishing acceptable and repeatable methods for laboratory procedures to continue into the master's thesis. Because the methods used in this project were developed during the specialization project, this chapter is, therefore, the least edited chapter from the preliminary project report. However, many of the following sections are adapted as the methods were developed and changed during the experiments.

## 3.2 Laboratory set-up

The three experiments consisted of piezocone penetrometer testing in a large scale test chamber. In addition, density tests were taken during the excavation of the chamber. This section will include the methodology of the physical experiments and the laboratory set-up.

### 3.2.1 Chamber

To perform the CPTU-testing, a chamber was used to build in the sand sample. The chamber is 146 cm high, and has a diameter of 120 cm. The chamber consist of two cylindrical concrete elements, where the bottom element consist of cylindrical wall on a concrete slab. The height of the bottom element is 95 cm, while the top element has a height of 51 cm. A rubber gasket was placed along the intersection to make sure that no leakage of water would occur along the joint. A picture of the chamber set-up is presented in figure 3.1.



**Figure 3.1:** Chamber set-up

**Terminology**

The chamber is divided into three 120 degrees sectors, AB, BC and CA as illustrated in figure 4.1. The divisions between the sectors are denoted section a, b and c. The soundings were performed in sections 1, 3a, 3b and 3c. An abbreviation is made for the name of the soundings for each experiment, for example, is experiment 2 and section 3a, named $M2\_3a$.
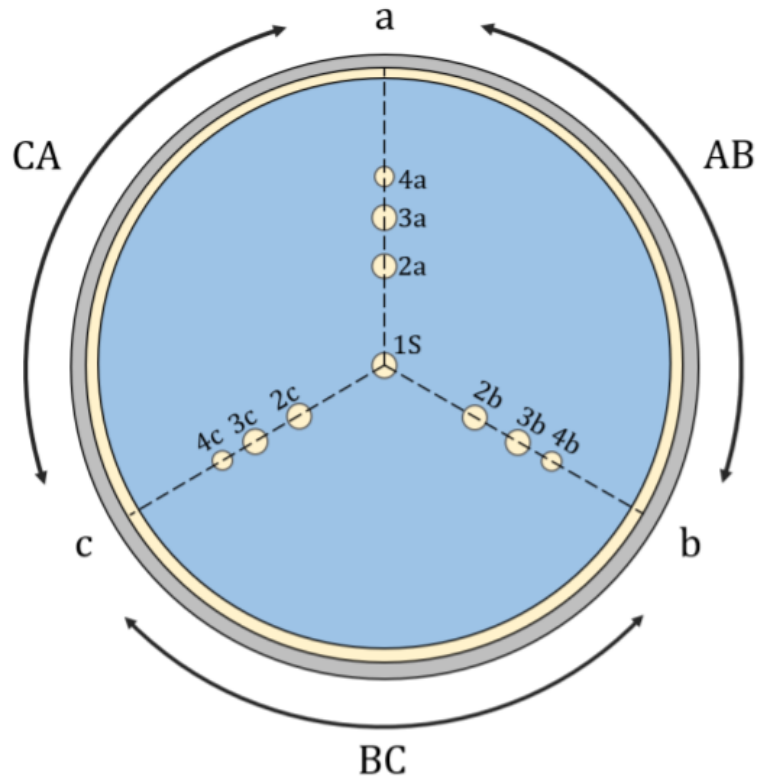


**Figure 3.2:** Chamber divided into sectors AB, BC, CA and sections a, b and c. Soundings were performed in sections 1, 3a, 3b and 3c. Illustration from Skrede (2021).

**Wall treatment**

The concrete chamber was in bad shape after previous experiments, where the wall treatment had flaked off the wall, as shown in figure 3.3a. During the preliminary project, the interior wall of the bottom chamber was sanded down using an angle grinder before being treated with epoxy coating to reduce friction and arching effect as much as possible, to achieve a waterproof interior. The epoxy primer and coating used were the MAPEI Primer SN and MAPEI Mapecoat I. Four layers of the epoxy coating was applied. Treated interior wall are shown in figure 3.3b. The extension chamber element seemed to be in better conditions than the bottom chamber and was therefore not treated in the preliminary project. However, the wall of the top element got worse throughout the experiments. Prior to the experiments in this current project, the extension element was replaced with a new element, and the wall were sanded down and treated with the same epoxy coating as the bottom element.
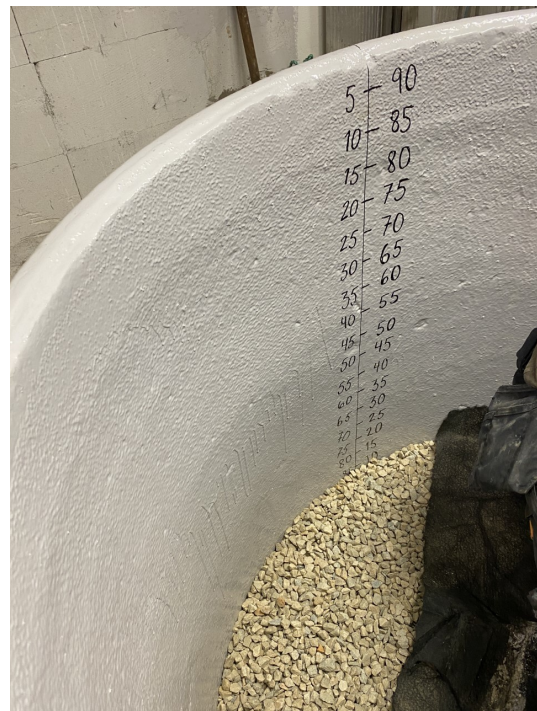


(a)                                                          (b)

**Figure 3.3:** Fig 3.3a: Interior wall prior to treatment. Fig. 3.3b: Interior wall after being sanded and treated with epoxy coating

The silo effects observed during the preliminary project were large. To further limit the arching effects in the chamber, a plastic lining was added to the chamber wall before the sample was built in. The plastic was implemented as two layers, with low friction grease between the plastic sheets. The lining closest to the wall was attached with tape during the entire experiment, while the outer layer was loosened as the sand was built in. This way, the double plastic lining would work as a floating ring, and the outer lining would move down with the sand as it was compressed, reducing the hanging friction working on the wall. The inserted plastic lining in the chamber is shown in figure 3.4



**Figure 3.4:** Plastic lining was inserted to work as a floating ring reducing the arching effects on the wall.

### 3.2.2 Hydraulic system

The hydraulic system of the chamber is presented in Figure 3.5. Valves were located on the bottom of the chamber wall to allow water flow. A pore pressure measurement was installed on the valves to register the pore pressure during the sample building and CPTU-testing. This way, the height of the water table could easily be checked, but while filling, the measured pore pressure was affected by the gradient, and it took a while before the pore pressure stabilized after the filling was stopped. A water reservoir was used as the water source, and the water was transferred to the hydraulic system of the chamber with a water pump. The hydraulic system consisted of a 20-litre container. This container was raised and lowered to control the gradient of the water flow into the chamber. By minimizing the gradient, there would be less sorting of the soil material in the chamber.
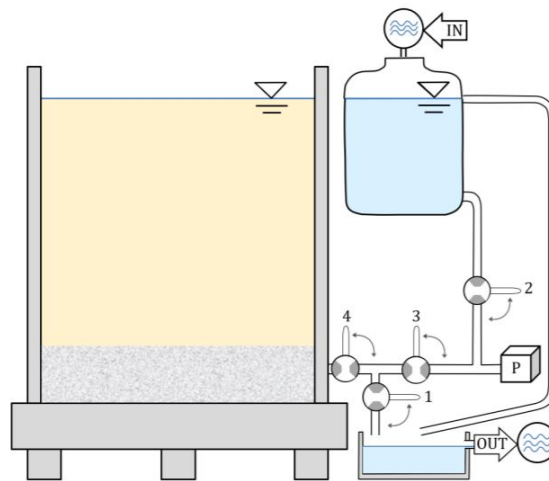
**Figure 3.5:** Hydraulic system in chamber (Skrede, 2021)

### 3.2.3 Additional overburden load

The sand sample was subjected to an overburden load to simulate in-situ stress conditions. A steel framework consisting of a circular disk and three air bellows was implemented by Skrede (2021). The load was applied by increasing air pressure to the bellows. The metal disk has a diameter of 1.15 meters. Ten holes were cut out along sections a, b and c to allow room for the sounding equipment through to the chamber, according to Figure 4.1. The installed framework for overburden load is shown in Figure 3.6.
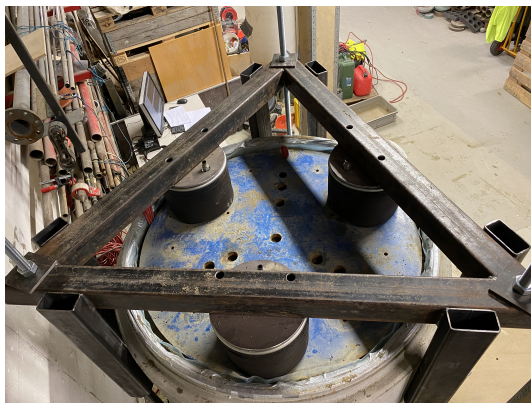


**(a)**

**(b)**

**Figure 3.6:** The loading framework with air bellows for imposing load to the metal disk on top of the sample.

Hammer used in his study an overburden load of 11.4 kPa (Hammer, 2020). Skrede, on the other hand, applied an overburden load of 40 kPa and 80 kPa in his master's thesis (Skrede, 2021). In this study,

a surcharge load of 80 kPa was applied. The loading frame was designed for the applied load, but to ensure no rotational displacement took place, the loading frame was secured with straps.

### 3.2.4 Pressure cells

Five Geokon Model 3500-1 pressure cells were built in the sand sample at the height of approximately 20 cm. The cells were placed to measure the overburden load and indicate the stress distribution in the chamber. One of the pressure cells was placed horizontally to register the horizontal stress conditions in the chamber as a basis to determine the lateral earth pressure coefficient, $K_0$. The pressure cells were placed as shown in Figure 3.7.
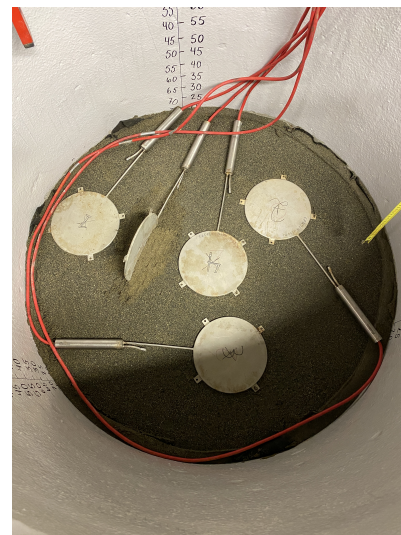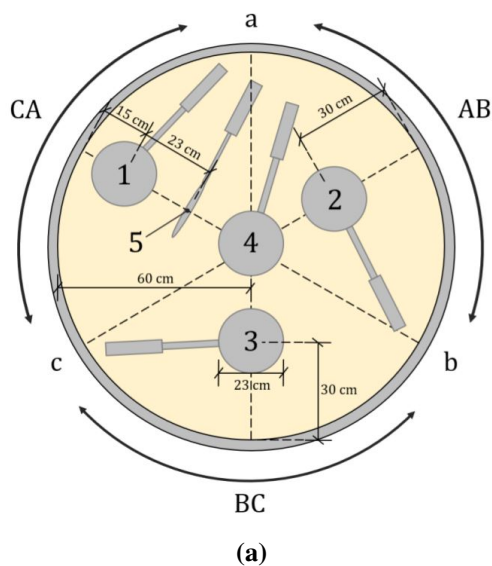


**Figure 3.7:** Placement of pressure cells in test chamber (Skrede, 2021).

A lot of time was spent calibrating the earth pressure cells. Initially, each cell was placed and calibrated in a large chamber filled with water. Despite being calibrated, they showed fluctuating results after being placed in the chamber and reset to zero. The cells were laid horizontally, sand was carefully put around the cells, and water was filled 0.5 cm above the cells before resetting them to zero. The pressure cells have a range of 600 kPa, and the observed variation could be because the load from the static water pressure of 1 m water column generated a limited load that was acting on the cells during calibration relative to the load range. This could lead to low accuracy for higher stress states once the surcharge load was applied to the chamber. An additional cell was placed close to the top of the sample to secure accurate results from the earth pressure cells. The placement of the pressure cells is given in Figure 3.8. A surcharge load of 80 kPa was applied before calibrating the pressure cells to the respective load. Hence, the pressure cells were calibrated for the load to be used throughout the experiments.

Some uncertainties are associated with this approach. It could be that the steel plate in which the load is

applied is too stiff, such that some of the applied load was taken up by the sand surrounding the pressure cell. However, after the calibration, all earth pressure cells showed somewhat expected values for the given overburden load, which was therefore thought to be a good indication of the stress distribution in the chamber.



| (a) | (b) |
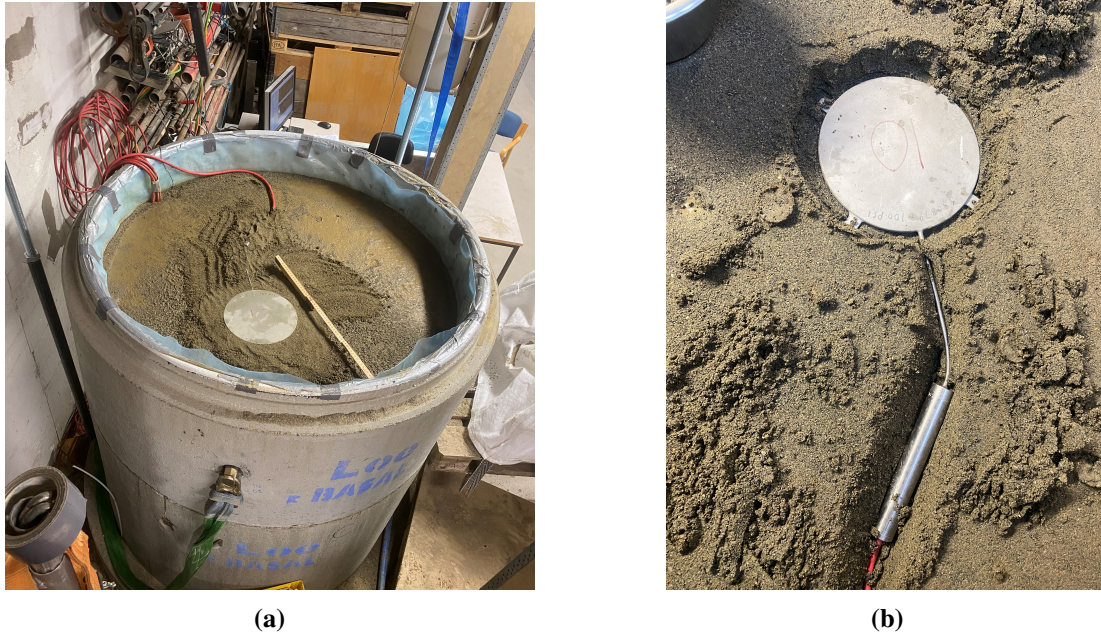
**Figure 3.8:** Placement of earth pressure cell placed close to top of the sample. To calibrate for the load range to be applied during CPTU-testing, the pressure cells were calibrated after a load of 80 kPa was applied.

The earth pressure cells were prone to sensitivity drift due to temperature changes. In the study by Skrede (2021), the pressure cells showed the impact of sensitivity drift over a period with no overburden load, as shown in figure 3.9. Skrede suggested using water at a constant temperature, but due to the laboratory set-up, this proved to be challenging. To limit the drifting in this current project, a water reservoir was implemented to maintain the water at a constant room temperature. The water was then transferred from the reservoir to the hydraulic system using a water pump. In addition, temperature measurement was installed in the chamber to detect any change in temperature.
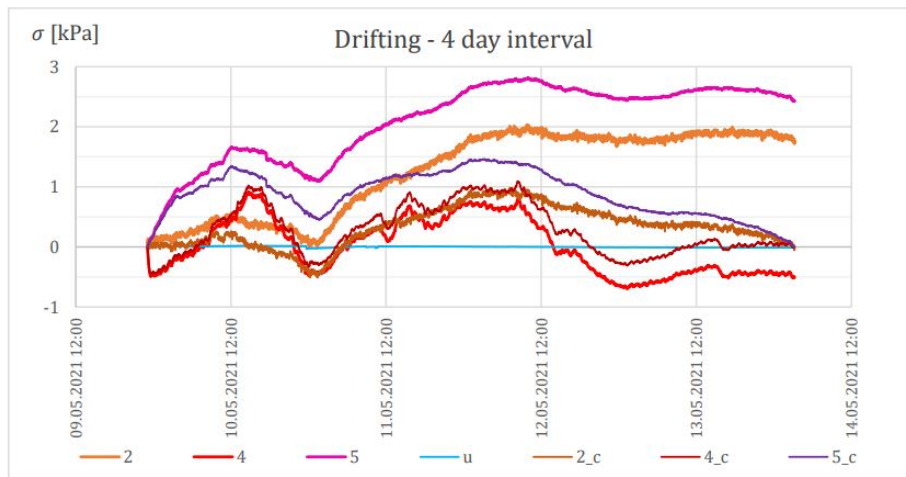
**Figure 3.9:** Sensitivity drift in experiments performed by Skrede (2021) with no imposed load on the cells.

### 3.2.5 Actuator

An actuator with a capacity of 9.5 kN was implemented to press the penetrometer with constant speed into the sample during testing. The actuator was bolted on a steel rack and locked into position with a steel frame attached to the ceiling. In the conducted experiments, the actuator pushed the cone penetrometer through the soil at a constant rate of 15 mm/s. The installed actuator on the metal frame is shown in figure 3.10.

**Figure 3.10:** The actuator installed on metal frames to push the CPT through the sand sample at a constant rate of 15 mm/s.

## 3.3 Sounding equipment

Three Experiments were performed, where four soundings were conducted for each experiment. During this study, two sounding probes were used. This included a standard piezocone penetrometer and a mini piezocone penetrometer.

### 3.3.1 Standard Piezocone penetrometer

The standard piezocone penetrometer used in most experiments was of the type NOVA-sonde by GeoTech. This cone penetrometer follows the requirements of Eurocode NS-EN ISO 22476-1:2012 and has a cross-section area of $10cm^2$ and a cone diameter of 3.57 cm (ISO 22476-1:2012). Before each sounding, the cone was saturated, as described in Chapter 3.3.3. The data was saved on a memory disk installed in the cone during penetration. Afterwards, the memory disk was plugged into a laptop, and the data was copied as a dump file. This is a file with all the data in different columns. The data was interpreted by an excel sheet adapted from Hammer (2020). The depth was logged from the actuator, and the time of start and end was carefully noted to be able to set the correct resistance against the associated depth.

The standard probe registered readings of 64 data points with fixed time intervals of 25 seconds. To achieve as many readings as possible, the penetration rate was set to 15 mm/s, which is the lowest standard penetration rate allowed according to NS-EN 22476-1:2012 (ISO 22476-1:2012). According to Skrede (2021), this would increase the measurement density by 33 % for the same sounding length.

The penetrometer registers readings with reference to time, while regular programs for treating the CPTU-data assign the readings to data sets with reference to specific depth intervals of 1 cm. This could lead to misrepresentation of data (Skrede, 2021). To prevent this, the data registered from the sounding tests are adapted to associated time and depth from the actuator readings.

### 3.3.2  Mini-piezocone penetrometer

To limit the chamber to cone ratio and, therefore, the boundary effects on the cone resistance, it was desirable to use the mini piezoncone penetrometer. The mini-probe penetrometer was of the type 201Xb-d by Geomil Equipment. The cone has a cross-section area of $5cm^2$ and a 2.52 cm diameter. This piezocone was set up with a cable to a data logger, sending the signals to the CPT program on the computer. The depth encoder sent the signals to the same CPT program, and the program plotted tip resistance, side friction and pore pressure by depth. Another program recorded the actuator force and the pressure cells, and all the data were plotted and interpreted using excel. This penetrometer registers data with reference to depth and has a higher reading frequency than the standard piezocone penetrometer.

### 3.3.3  Saturation procedure

To successfully measure the change in pore pressure, ensuring sufficient saturation of the pore pressure system is important. For the standard piezocone penetrometer, the filter is made out of bronze. Prior to the sounding, the filter was saturated using glycerine. Before starting the test, the filter is placed on the probe, and the cavity behind it is saturated.

The mini-probe penetrometer has a plastic filter that was saturated in silicon oil in a vacuum desiccator for 24 hours prior to the sounding. Before each sounding, the filters were placed on the probe, and the pore pressure chamber was saturated. The cone with the inserted filter was then saturated in silicone oil inside a vacuum desiccator for 10 minutes before starting testing. To ensure that the cone was fully saturated when the test started, a rubber membrane was used after the saturation process and removed just before the test started.
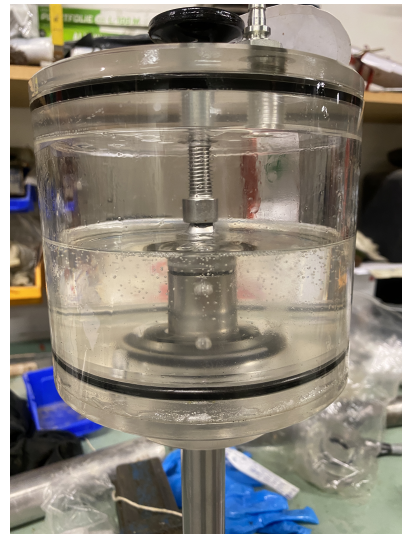
**(a)**                **(b)**

**Figure 3.11:** Fig. 3.11a: Saturated filter placed on cone and saturation of pore pressure chamber. Fig. 3.11b: Cone saturating for 10 min. prior to each sounding.

## 3.4 Supplementary tests on sand

To investigate the material properties of the sand, supplementary tests were performed on the sand. The tests consisted of a grain size distribution test, density tests and determination of void ratio limits, $e_{min}$ and $e_{max}$. In addition, two oedometer tests and two triaxial tests were performed on the sand to determine the strength parameters and the critical state line for the sand material.

The void ratio limits were determined through porosity procedures by both NGI (Norwegian Geotechnical Institute) and DEGEBO (Deutsche Gesellschaft für Bodenmechanik). The results from the tests are presented in chapter 3.5. The NGI approach to determine $e_{max}$ is done by drying the sand and then using a funnel to fill a cylinder with the sand. After filling the cylinder with sand, the cylinder was carefully lifted, and the sand ran out into a small chamber with a known volume and mass. The sand and the chamber were weighed, and $e_{max}$ could be calculated. This test was done five times, and an average from the five tests was used. To determine $e_{min}$, the machine shown in Figure 3.12 was used. The sand was built in five layers and fully saturated, and each layer vibrated for 30 seconds. Afterwards, the sand was dried and weighed.

**Figure 3.12:** The equipment used for determining the void ratio limit, $e_{min}$ according to the procedures suggested by DEGEBO.

### 3.4.1 Oedometer test

The oedometer test was performed to get the stiffness and flexibility parameter. The flexibility parameter $\lambda$ was determined from the modulus number m, determined from the plot of $\sigma'_v$ against module M. $\lambda$ has been essential in finding the critical state line for the Søberg sand. Building in the oedometer ring was conducted with pre-weighed material and 3% water content. The sand was carefully placed inside the ring before a solid cylinder was placed on top of the sand and stamped until the right height was achieved. The solid cylinder was removed, and the oedometer ring was placed in the oedometer cell. The installation and the preparations of the oedometer test were done with well-defined and good routines, with every step documented. The results are presented in Figure 4.25 and Appendix A.
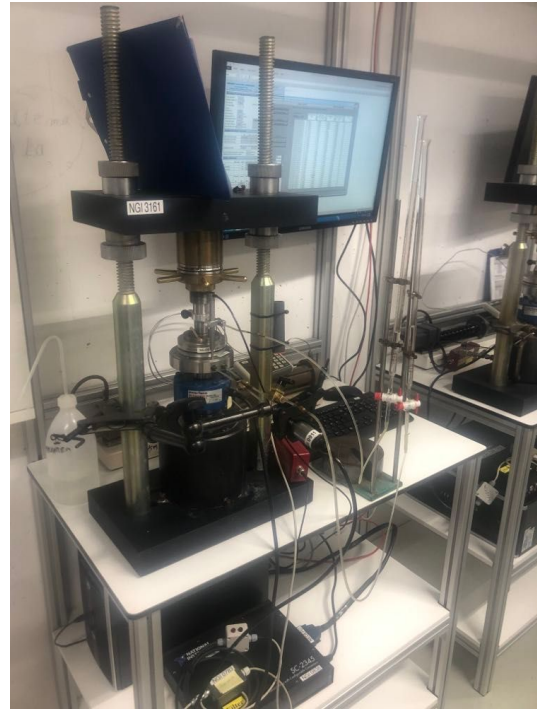
|          |          |
|:--------:|:--------:|
| **(a)**  | **(b)**  |

**Figure 3.13:** Fig. 3.13a: Building in the oedometer ring with pre-weighed material. The sand was carefully put in the ring with a spoon before a solid cylinder was placed on top of the sand and pounded with a club to the right height. Fig. 3.13b: The oedometer ring with the sand sample is mounted in the oedometer cell.

### 3.4.2 Triaxial test

Two triaxial tests were performed on the sand to determine the strength parameter and find a critical state point for the determination of the critical state line of the soil. For the tests, triaxial procedures for sand by NGI were utilized. One of the triaxial tests was performed at the laboratory of NGI to learn the procedures, and one was performed at the laboratory at NTNU. The installation, and the preparations of the triaxial test at NGI were done with well-defined and good routines, and every step was documented.
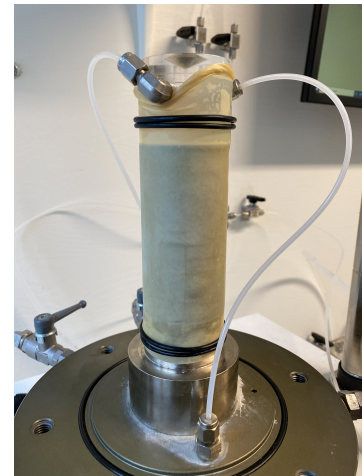
**Figure 3.14:** Fig. 3.14a: Equipment for building in triaxial sample of sand. Cylinder for sample construction, stamping equipment and sand material. Fig. 3.14b: Sand sample built in for triaxial testing.

Six samples of sand with 3% water content were measured out to a specific weight to achieve the desired relative density of the triaxial test sample. The sample was built in with six layers of sand, and the build-in height was calculated for each layer. The sand was stamped into the cylinder for sample construction until the specific height was achieved. The Triaxial results are presented in Appendix B, and the interpreted strength and stiffness parameters are presented in chapter 3.5.

## 3.5 Sand material

To determine the material properties, laboratory tests were performed on the sand; sieve testing, density testing, two oedometer tests and two triaxial tests. The sand used in the project was extracted from Søberg grustak in Melhus municipality. The sand is of the type 0/2, meaning the grain size should be less or equal to 2 mm. The grain size characteristics were determined through sieve testing, which showed that the sand is uniformly graded with 2.95 mass percent of the sand consisting of grains larger than 2 mm. The determined grain characteristics are presented in table 3.1. The grain size distribution chart is presented in Appendix F. The attraction for the sand was set to 1 kPa because the attraction around the cone is assumed to be small. To be consistent, attraction equal to 1 kPa has been used for all the calculations.

**Table 3.1:** Grain size characteristics for Søberg sand.

| $d_{10}$ | $d_{50}$ | $d_{60}$ | $C_u = \frac{d_{60}}{d_{10}}$ |
|:---:|:---:|:---:|:---:|
| [mm] | [mm] | [mm] | [-] |
| 0.19 | 0.58 | 0.74 | 3.89 |

The sand used earlier in the research project at NTNU by Hammer (2020) and Skrede (2021) was extracted from Stokke Grustak, also located in Melhus municipality and labelled 0/2. Additional information on the Stokke sand could be found in the master's theses of Hammer (2020) and Skrede (2021).



**Figure 3.15:** Sand material

Density characteristics, i.e. grain density, $\rho_s$ and the porosity limits, $e_{min}$ and $e_{max}$, were determined through porosity procedures by both NGI and DEGEBO (Deutsche Gesellschaft für Bodenmechanik), and the properties are presented in Table 3.2.

**Table 3.2:** Density characteristics for Søberg sand.

| $\rho_s$ | $e_{min}$ | $e_{max}$ |
|:---:|:---:|:---:|
| $[kg/m^3]$ | [-] | [-] |
| 2.76 | 0.556 | 0.837 |

The strength and stiffness parameters of the sand were determined through two triaxial tests and two oedometer tests. The determined stiffness is presented in Tables 3.3 and 3.4 . The two triaxial tests were executed with a relative density of 50%, or a void ratio of 0.7. In addition, the stiffness parameters for the sand determined by Hammer (2020) are presented in table 3.3. Hammer (2020) performed two triaxial tests on the sand, one very loose sample with a relative density of 0% (e=0.86) and a medium dense sample with a relative density of 60% (e=0.65).

**Table 3.3:** Strength and stiffness parameters of the sand based on triaxial testing. Two of the triaxial tests ($e = 0.86$ and $e = 0.65$) were performed by Hammer (2020) on Stokke sand

| e | $\phi$ | $E_{50}$ |
|---|---|---|
| 0.86 | 24° | 4 MPa |
| 0.65 | 43° | 18 MPa |

**Table 3.4:** Strength and stiffness parameters of the sand based on triaxial testing. Two of the triaxial tests (e=0.7 and e=0.7) were performed in this study on Søberg sand.

| e | $\phi$ | $E_{50}$ |
|---|---|---|
| 0.7 | 35° | 15.8 MPa |
| 0.7 | 33.5° | 16.2 MPa |

Conventional cone penetration testing aims to determine the strength and stiffness parameters, such as the friction angle. During this study, the aim was to investigate the plastified zones in terms of the plastification angle. The friction angles were therefore assumed from the triaxial tests, where it was interpolated between the determined friction angles based on the measured void ratio of the sample.
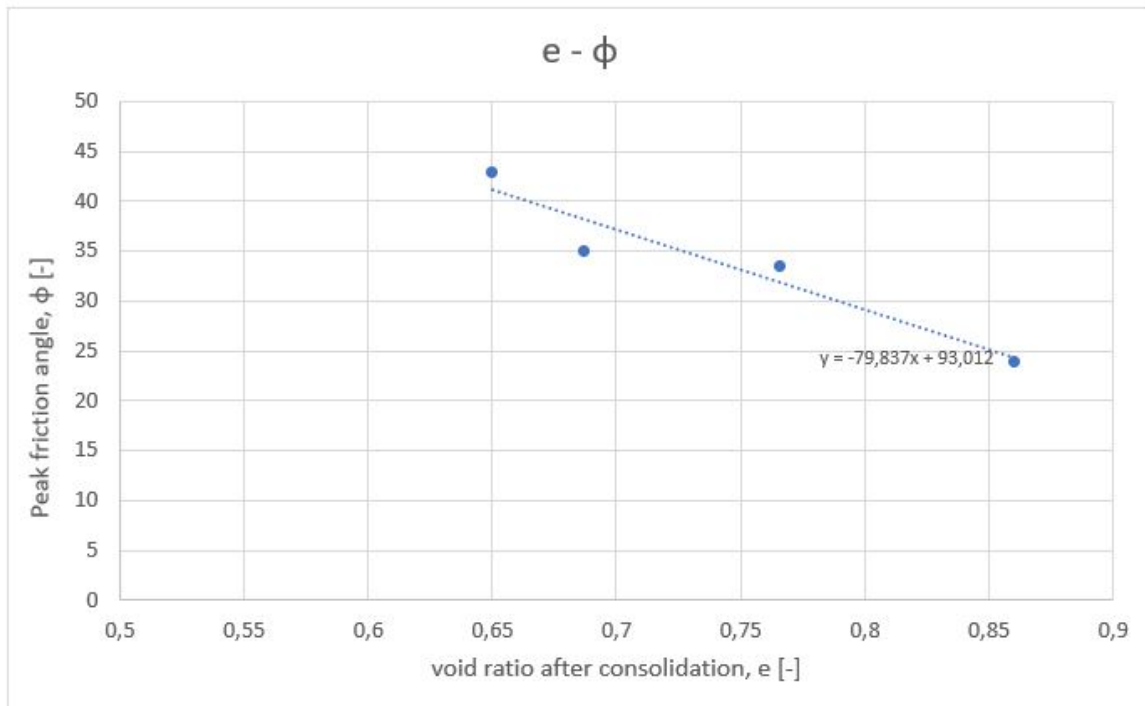
**Figure 3.16:** Void ratio, e, after consolidation of the triaxial sample vs. interpreted peak friction angle from the triaxial results. Determination of friction angle based on linear interpolation of four triaxial tests. Triaxial tests with e=0.86 and e=0.65 were performed by Hammer (2020) (Stokke sand), while triaxial tests with e=0.7 and e=0.7 performed during this current study (Søberg sand).

The critical state line for the sand was determined based on the theory presented in chapter 2.4, where the inclination is based on oedometer tests and the critical state point is based on two triaxial tests. The critical state line for the sand from the Søberg gravel pit is presented in Figure 3.17.
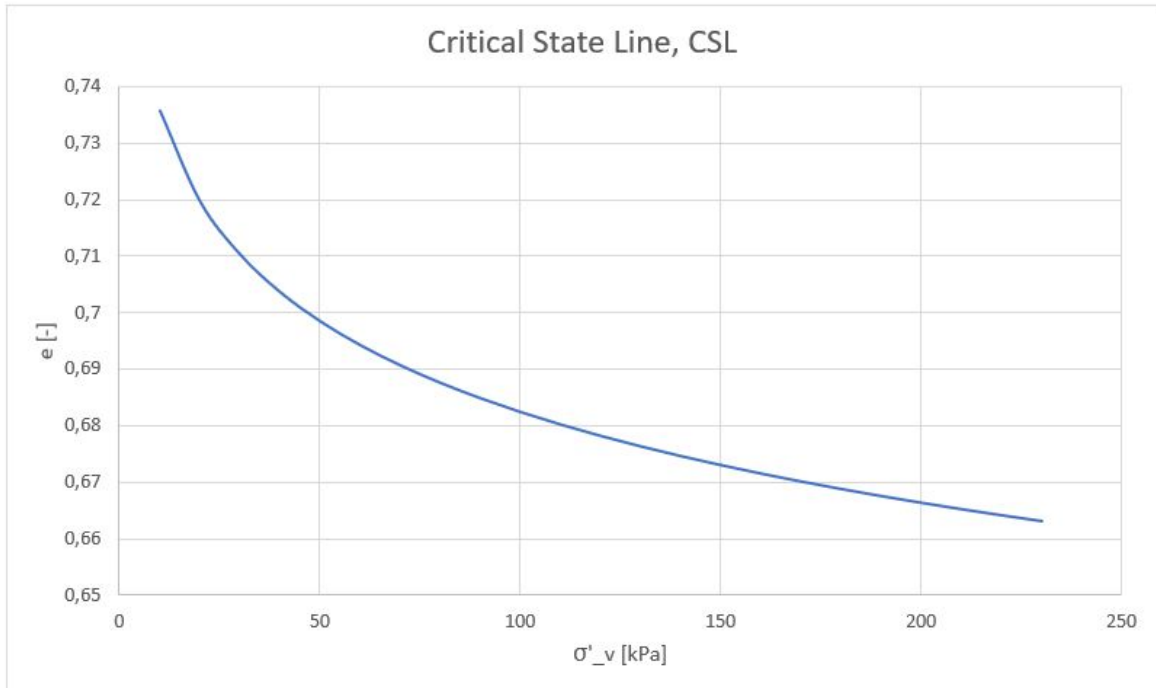
**Figure 3.17:** Critical state line for 0-2 sand from the Søberg gravel pit $\sigma'_v$ - e plot. The critical state line is based on two triaxial tests and two oedometer test. Two critical state points are given by the triaxial tests and the inclination of the critical state line is given by oedometer results.

## 3.6  Experiments and sample set-up

In total, three experiments were performed. All the experiments consisted entirely of sand. The sand preparation procedure was followed as described in Chapter 3.6.1. The test chamber was filled up with eleven layers of approximately 10 cm each above the earth pressure cells. The depth profile is presented in table 3.5. Extra ground pressure or overburden load was applied as described in Chapter 3.2.3. The soundings were performed in sections 1, 3a, 3b and 3c. 80 kPa of extra ground pressure was applied for all the soundings. For sounding $M2\_1$, the overburden load was reduced to 40 kPa, because the maximum capacity of the actuator was reached. The soundings were run to a depth of 1.1 to 1.2 meters. The compaction time was calculated for experiment M1 by the excel sheet presented by Hammer (2020) to prevent over compaction of the bottom layers. This gave a mean void ratio of 0.742 with a standard deviation of 0.038. For experiment M2, the compaction time for each layer was increased by ten seconds to obtain a denser sample. For M2, the mean void ratio was measured at 0.709 with a standard deviation of 0.044. For the last experiment, M3, the compaction time was increased by five seconds relative to M1. This gave a mean void ratio of 0.735 and a standard deviation of 0.038.

**Table 3.5:** Experiment set-up with layering

| Depth | Experiment M1 $H_s$ [cm] | z [cm] | Experiment M2 $H_s$ [cm] | z [cm] | Experiment M3 $H_s$ [cm] | z [cm] |
|---|---|---|---|---|---|---|
| Sand, top level | 138.1 | 7.9 | 139.8 | 6.2 | 139.9 | 6.1 |
| Pressure cells | 18.9 | 127.1 | 20.7 | 125.3 | 21 | 125 |
| Gravel, top | 10 | 136 | 10 | 136 | 10 | 136 |
| Bottom | 0 | 146 | 0 | 146 | 0 | 146 |
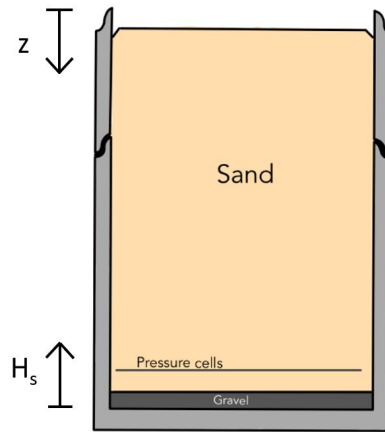


**Figure 3.18:** Experiment set-up for the physical experiments M1, M2 and M3. The depth to the top of the sample with reference from the top of the chamber is denoted z. The height of the sample from the bottom floor of the chamber is denoted $H_s$.

### 3.6.1 Sample preparation

**Base Layer**

At the bottom of the chamber, a 10 cm layer of gravel was placed. This layer was placed to make the sample saturation as homogeneous as possible, allowing for an evenly distributed flow of water. Figure 3.19a and Figure 3.19b show the gravel and the filter cloths, respectively. The filter cloth separates the gravel and the overlying sand and prevents washing of the finer fractions from the chamber. The filter cloths were laid with 20 cm overlap and 10 cm up on the chamber wall.

**Figure 3.19:** Fig 3.19a: First layer consisting of 10 cm gravel. Fig 3.19b: Filter cloths preventing washing of finer fractions

## Sand preparation procedure

The method and the procedure for sand used in this project are based on the method developed by Skrede (2021). The preparation of the sand was done step by step and consistently to make the test specimen as homogeneous as possible. The test specimen is constructed of equally thick layers of 10 cm, except for the layer above the earth pressure cells, which is 20 cm. First, the sand was shovelled from the bags into the chamber and levelled evenly. The second step was to saturate the sample and then level it evenly again. For the third step, the water was discharged, which gave a downward gradient and settlements named $\Delta h_s$. The fourth and last step was conducted by using a plate vibrator to achieve further compaction of the sample. The vibration time was increased for each new layer to prevent any over-compaction of the previous layers. The vibration time necessary to avoid over compaction was calculated based on the thickness of the layer and the depth to the bottom of the chamber. The formula of vibration time is given by Hammer (2020). The settlement generated by the plate vibrator is called $\Delta h_c$. Figure 3.20a shows a fully saturated layer, and figure 3.20b shows the plate vibrator and the wooden plate. For each step, the height from the top of the chamber down to the current level was measured.
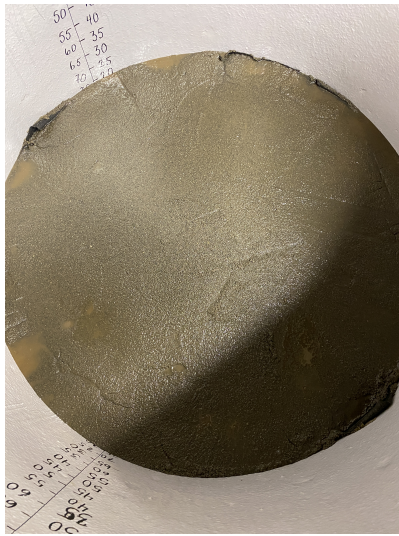
**(a)**                      **(b)**

**Figure 3.20:** Fig 3.20a: The sand was fully saturated and emptied to compact the sand. Fig 3.20b: Each layer were compacted with a plate vibrator on a wooden plate to distribute the vibration evenly.

### Excavation and density sampling

During the excavation, density tests of the sand were taken for 10 cm depth intervals for each of the sectors AB, BC and AC. The density samples were collected in a steel cylinder with a diameter of 7,2 cm. The tests were taken approximately 28 cm from the interior wall by pushing the cylinder into the sand and carefully excavating the sample. The weight of the sand was then measured before placing the samples in the oven. From the weight of the dried samples, the void ratio and relative density were calculated according to equations 3.1 and 3.2.

$$e = \frac{\rho_s}{\rho_d} - 1 \tag{3.1}$$

$$D_r = \frac{e_{max} - e}{e_{max} - e_{min}} \tag{3.2}$$

<div align="center">(a)          (b)</div>

**Figure 3.21:** Density sampling performed every 10 cm of depth in the chamber to measure void ratio and relative density.

## 3.7 Analysis

### 3.7.1 Interpretation of CPTU data

The readings from the soundings and other data collected during this study are processed using Excel. The CPTU-measurements, $q_c$, $f_s$ and $u$, were assessed as described in chapter 2.1.1. Because the pore pressure generated by the advancing cone is assumed to be insignificant in the sand material, the cone resistance, $q_c$, is not corrected for the unequal effect in this study. The CPTU-results were further analysed based on the NTH method to find the plastification angle, $\beta$. This is described in the following section.

### 3.7.2 Analysis of the stress field

During this study, the behaviour of sand during cone penetration testing is investigated. The effective stress based bearing capacity solutions (NTH-method) developed by Janbu et al. (1989) is used as the theoretical framework for the investigation of the deformation pattern that occurs around the advancing cone. Conventionally, the NTH method is used to assess the friction angle, $\phi$. However, if the friction angle was assumed to be known, the plastification angle could be assessed to learn more about the plastified zones around the cone tip. In this study, the friction angle of the sand is assumed based on linear interpolation from triaxial tests based on measured void ratio as described in chapter 3.5. The plastification angle is then determined from back-calculation of the bearing capacity formulas.

From the assumption of friction angle, the plastification angle, $\beta$, can be estimated if the bearing capacity factor, $N_q$, is known. Under fully drained conditions, no excess pore pressure will occur, and the pore pressure ratio, $B_q$, will equal zero. Hence, the cone resistance number, $N_m$, could be simplified as:

$$N_m = N_q - 1 \tag{3.3}$$

This would allow the bearing capacity factor, $N_q$, to be estimated from the tip resistance, $q_c$, through the cone resistance number, $N_m$. Considering equation 3.4, the plastification angle, $\beta$, could be expressed by equation 3.6

$$N_q = N_f \cdot e^{(\pi - 2\beta)\tan\phi} \tag{3.4}$$

where:

$$N_f = \tan^2(45 + \frac{\phi}{2}) \tag{3.5}$$

$$\beta = \frac{\pi \tan\phi \cdot \ln\left[\frac{N_q}{N_f}\right]}{2\tan\phi} \tag{3.6}$$

The plastification angle is a measure of the geometric size of the plastified zones and around the advancing cone. However, this parameter is difficult to assess, and the typical values based on stiffness and soil type are associated with a lot of uncertainties. To further study the failure mechanism around the cone tip during penetration, it would be desirable to investigate the influencing parameters of the plastification angle. This way, a more accurate method for assessing the plastification angle could be developed. The relative density is a common soil parameter, describing the density of the soil in relation to the void ratio limits, $e_{min}$ and $e_{max}$. Although the relative density is a commonly used parameter to describe soil behaviour, there are many uncertainties associated with the accuracy of determining the relative density of the soil. This is because of the uncertainties concerning the procedures when determining the void ratio limits, which vary from one laboratory to the next. A slight inaccuracy of the void ratio would lead to a significant inaccuracy in the relative density. In addition, the stress conditions affecting the soil are too complex to be described by the relative density alone, as the stress is not taken into account. Because of this, it was desirable to investigate whether there exists any correlation between the plastification angle and the state parameter, which considers the stress affecting the soil. In addition, to bypass the uncertainties with the relative density altogether, all calculations are based on the measured void ratio instead of the relative density. This way, the uncertainties associated with the determination of the void ratio limits do not affect the results in this study.

The relative density does not take into account the compressibility of the soil. According to P. K. Robertson and R. G. Campanella (1983), the cone resistance of the soil is affected by the sand density, vertical and horizontal stress and compressibility. When penetrating the cone through the sand, the sand would be compressed. This would affect the zone of plastification around the cone tip, and hence also the plastification angle. when implementing the state parameter approach, the compressibility would be taken into account, as the slope of the critical state line is an indirect measure of the compressibility of the soil (Lunne et al., 1997).

**Incorporation of state parameter: Simplified relation**

The relation between the angle of plastification, $\beta$, and the state parameter, $\psi_{BJ}$, may be made probable by simplifying equations 3.12 and 2.15 and roughly pragmatic, neglecting some parameters, considering the full foundation pressure in equation 3.7.

$$\sigma'_{vn} = (N_q - 1) \cdot (p' + a) + \frac{1}{2}\overline{\gamma}N_\gamma B_0 \tag{3.7}$$

For a cone penetration test, high stresses occur, and the effect of the attraction becomes very small, and $B_0$ is very small so these parameters may be neglected. Equation 3.7 can be updated to equation 3.8, where $p' = \sigma'_v$ and $\sigma'_{vn} = q_{net} = q_n$

$$q_n = (N_q - 1) \cdot \sigma'_v \tag{3.8}$$

The equation 3.8 is then divided by $\sigma'_v$ on both sides of the equation, such that $q_n = q_c - \sigma_v$. $N_q = N \cdot e^{(\pi - 2\beta)\tan\phi}$, where $N = \tan^2(45 + \frac{\phi}{2})$. Roughly pragmatic may $(-1)$ be neglected for high values of $N_q$. Now the equation can be written:

$$\frac{q_c - \sigma_v}{\sigma'_v} = N \cdot e^{(\pi - 2\beta)\tan\phi} \tag{3.9}$$

Equation 3.9 is now compared with equation 3.10 from Been et al. (1987).

$$\frac{q_c - p}{p'} = k \cdot e^{-m\psi_{BJ}} \tag{3.10}$$

Equation 3.9 is rewritten to equation 3.11. $\frac{q_c - \sigma_v}{\sigma'_v}$ expresses the same concept and meaning as $\frac{q_c - p}{p'}$. Therefor are the two expressions directly compared.

$$\frac{q_c - \sigma_v}{\sigma'_v} = N \cdot e^{\pi\tan\phi} \cdot e^{-2\beta\tan\phi} \tag{3.11}$$

The two equations 3.10 and 3.11 look very similar, where k is assumed to equal $N \cdot e^{\pi \tan \phi}$, and $m\psi_{BJ}$ is assumed to equal $2\beta \tan \phi$.

To comment on the results, it is known that k from Been et al. (1987) is a constant for a given sand material, while $N \cdot e^{\pi \tan \phi}$ will vary because $\phi$ is dependent on stress and void ratio. k is the normalized $q_c$ value at $\psi_{BJ} = 0$. This could be interpreted so that $\phi$ actually is $\phi_{cs}$, which gives $k = N \cdot e^{\pi \tan \phi_{cs}}$ and makes it a constant. The other option is that k is dependent on $\phi$ and will vary with the friction. $2\beta \tan \phi$ is in the same order of magnitude as $m\psi_{BJ}$, and both vary. $\beta$ must be in radians when used in the formulas.

**Full relation**

The relation between $\beta$ and $\psi_{BJ}$ can theoretically be derived from equation 2.15 and equation 3.12. The two equations are set equal to each other and solved for $\beta$. The relation is presented in equation 3.13. Equation 3.12 is an adaption of equation 2.19 and equation 2.21, where $N_f = \tan^2(45 + \frac{\phi}{2})$.

$$q_n = (N_f e^{(\pi - 2\beta) \tan \phi} - 1)\sigma'_{v0} \tag{3.12}$$

Further $q_n = q_c - \sigma_v$ and $\sigma'_v$ is divided on both sides. For high values of $N_q$, $(-1)$ can be neglected.

$$\beta = \frac{\pi}{2} - \frac{1}{2 \tan \phi} ln \left[ \frac{p'k e^{-m\psi_{BJ}} + p - \sigma_{v0}}{N_f(\sigma'_{v0})} \right] \tag{3.13}$$

Equation 3.13 has been plotted against state parameter $\psi_{BJ}$ for all the soundings conducted in the experiments and compared to a plot with $\beta$ from equation 3.6 vs the state parameter $\psi_{BJ}$. This comparison of the two graphs gives a good correlation between the two theories, as shown in Figures 4.17 and 4.19.

### 3.7.3   Numerical Analysis

The stress field around the advancing cone is also investigated through numerical analysis using the material point method. A numerical model of the CPT was developed, and three simulations of the cone penetration in sand material were computed. The simulations were run using high-performance computing (HPC) from Sigma2. The material properties used for the sand material were the same as for the sand used in the physical experiments, except for the stiffness of the soil, where the bulk modulus was set very low, to 830 kPa, to minimize the computational cost. This reduction in stiffness took the computation time from a few days to a few hours. Simulations were run for sand material denser than critical ($\psi = +3°$), looser than critical ($\psi = -3°$) and at critical state ($\psi = 0°$). The different simulations were run with the same friction angle, not to vary too many parameters.

The sand behaviour is described by the Mohr-Coulomb model. The material is assumed to be linear elastic until it reaches failure, and after failure, it is assumed to be perfectly plastic. Failure is given by Mohr-Coulomb. From the simulations, the shear strain and the volumetric strain were used to try to locate the stress field around the cone tip. This was then compared to the stress field determined from the laboratory experiments using the NTH method. The aim was to investigate whether any discrepancies or similarities could be detected between the numerical and the empirical stress field.

# Chapter 4

# Results

The following chapter will present the results obtained from this study. The results presented in this chapter will consist of the CPTU sounding measurements from the three test cases and the interpretation results in terms of the plastification angle, $\beta$, the investigated relation and correlation between the NTH method and the state parameter approach. The results from supplementary laboratory tests on the sand material consisting of oedometer test results and interpretation will also be presented. Triaxial test results are presented in Appendix B. Lastly, the numerical analysis of the stress field around the cone will be presented. In this chapter, the results are presented based on a division into Experiment M1, M2 or M3, and positioning in the chamber according to figure 4.1.
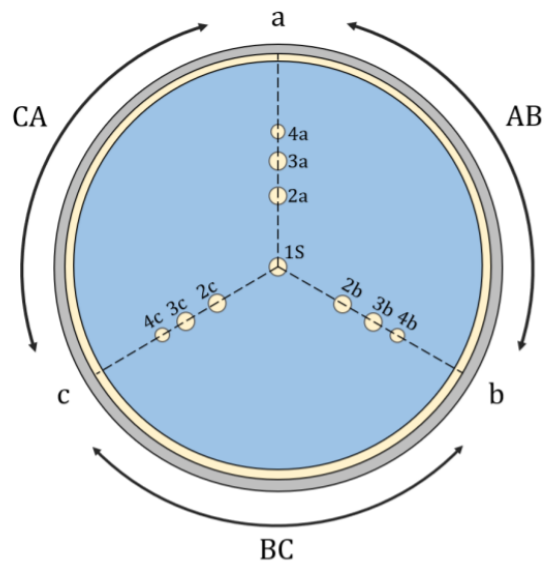


**Figure 4.1:** Chamber divided into sectors AB, BC, CA and sections a, b and c.

## 4.1 Measurements of CPTU soundings

The measurements of the CPTU soundings from the three experiments are presented in the following sections. The sounding data are acquired and treated according to the description in chapter 3.7.1, and further assessment is done according to chapter 3.7.2. All soundings are performed using a standard probe piezocone penetrometer, except from Experiment 1, section 3c, where the mini probe piezocone penetrometer was utilized. The mini-probe was not further used in the project due to equipment issues.

The sounding results are presented separately for the three experiments. Because of the high cone resistance relative to the generated pore pressures in sands, the cone resistance is not corrected for the unequal area effect. This effect is assumed to be low for coarse-grained material, and all cone resistance is presented by cone resistance, $q_c$. Sounding results are presented along with interpreted measured relative density. The relative density is also assessed from cone resistance, $q_c$, using both the method developed by Christoffersen and Lunne (1983) and the method developed at NGI called the NGI99 method.

The results show variations close to the top and bottom of the sample. This is due to the boundary effects close to the bottom and the steel disc with the applied surcharge load, affecting the void ratio in the sample close to the top and the bottom. Because of this effect, the variations close to the boundaries are neglected. A selection range in the middle of the sample is chosen to be further investigated in the analysis as the sand behaviour during cone penetration is of interest, and not the effects and variations caused by the surcharge load and boundary effects. The selection range is presented in the chart for cone resistance, $q_c$ in Figures 4.2, 4.3 and 4.4.

### 4.1.1 Experiment M1
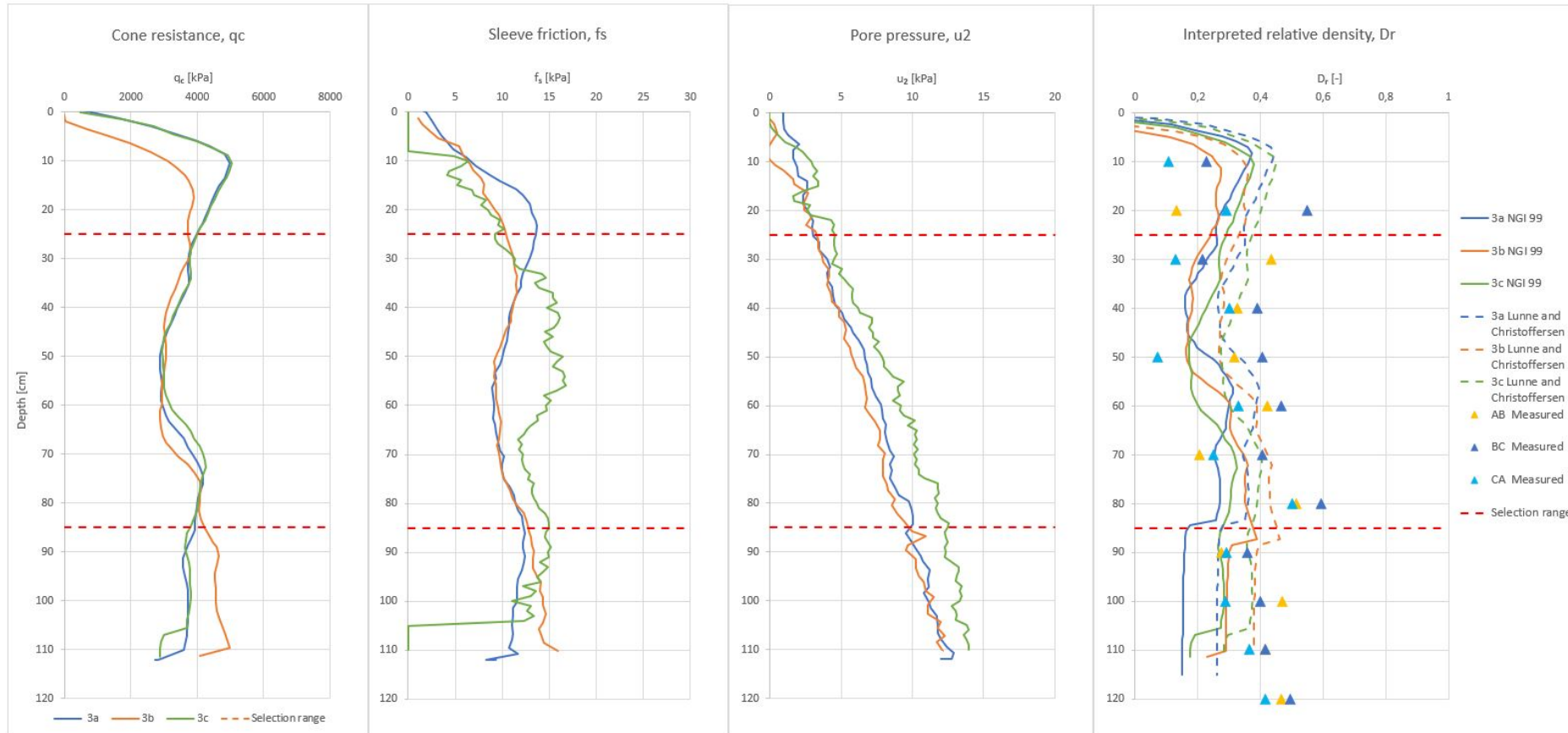


**Figure 4.2:** CPTU profiles with $q_c$, $f_s$ and $u_2$ from experiment M1. Interpreted relative density, $D_r$, using the NGI99 approach (solid lines) and the method developed by Lunne and Christoffersen (1983) (dashed lines), in addition to the measured relative density from laboratory experiments (triangle). The selection range that will be used further in the analysis (From depth 25 cm to 85 cm) are shown in the figure.

### 4.1.2 Experiment M2
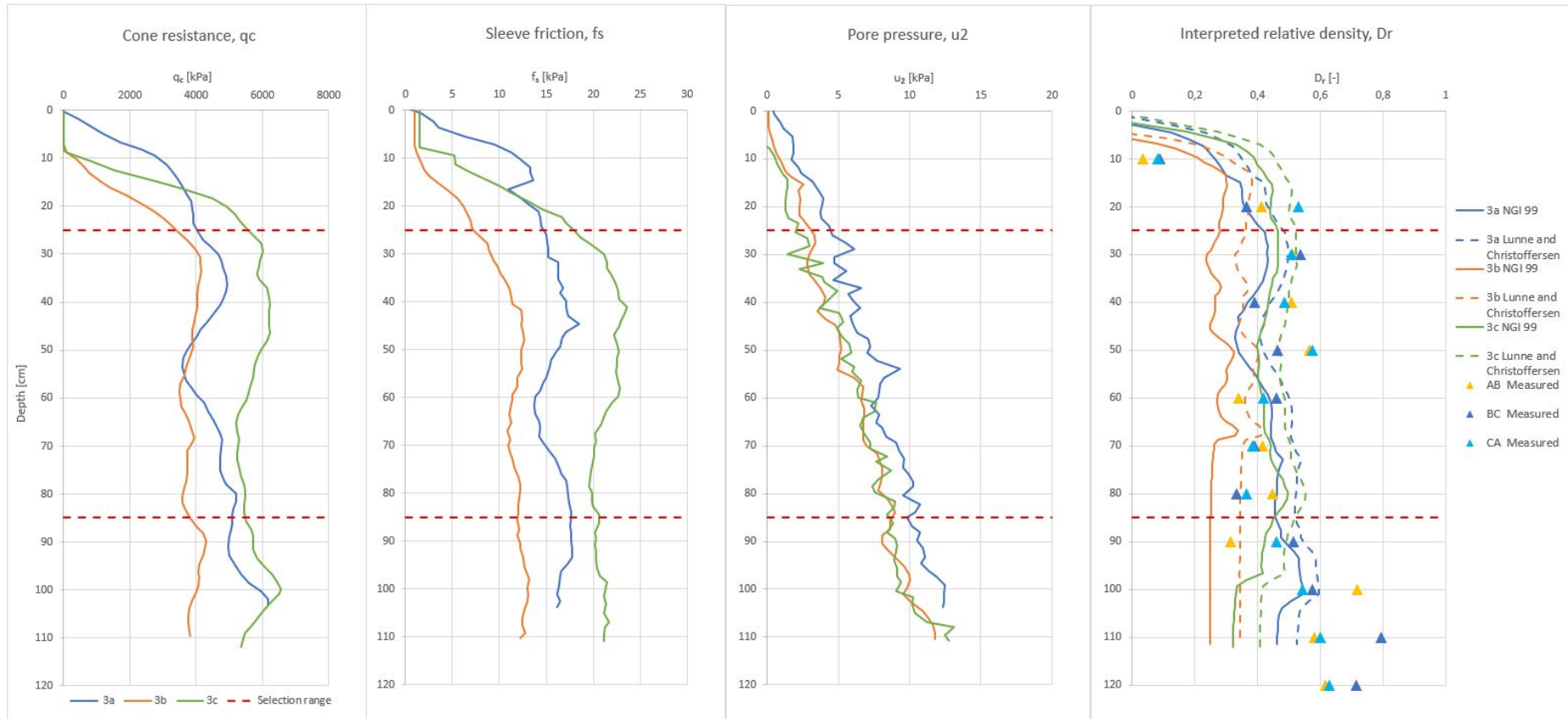


**Figure 4.3:** CPTU profiles with $q_c$, $f_s$ and $u_2$ from experiment M2. Interpreted relative density, $D_r$, using the NGI99 approach (solid lines) and the method developed by Lunne and Christoffersen (1983) (dashed lines), in addition to the measured relative density from laboratory experiments (triangle). The selection range that will be used further in the analysis (from depth 25 cm to 85 cm) are shown in the figure.

### 4.1.3 Experiment M3



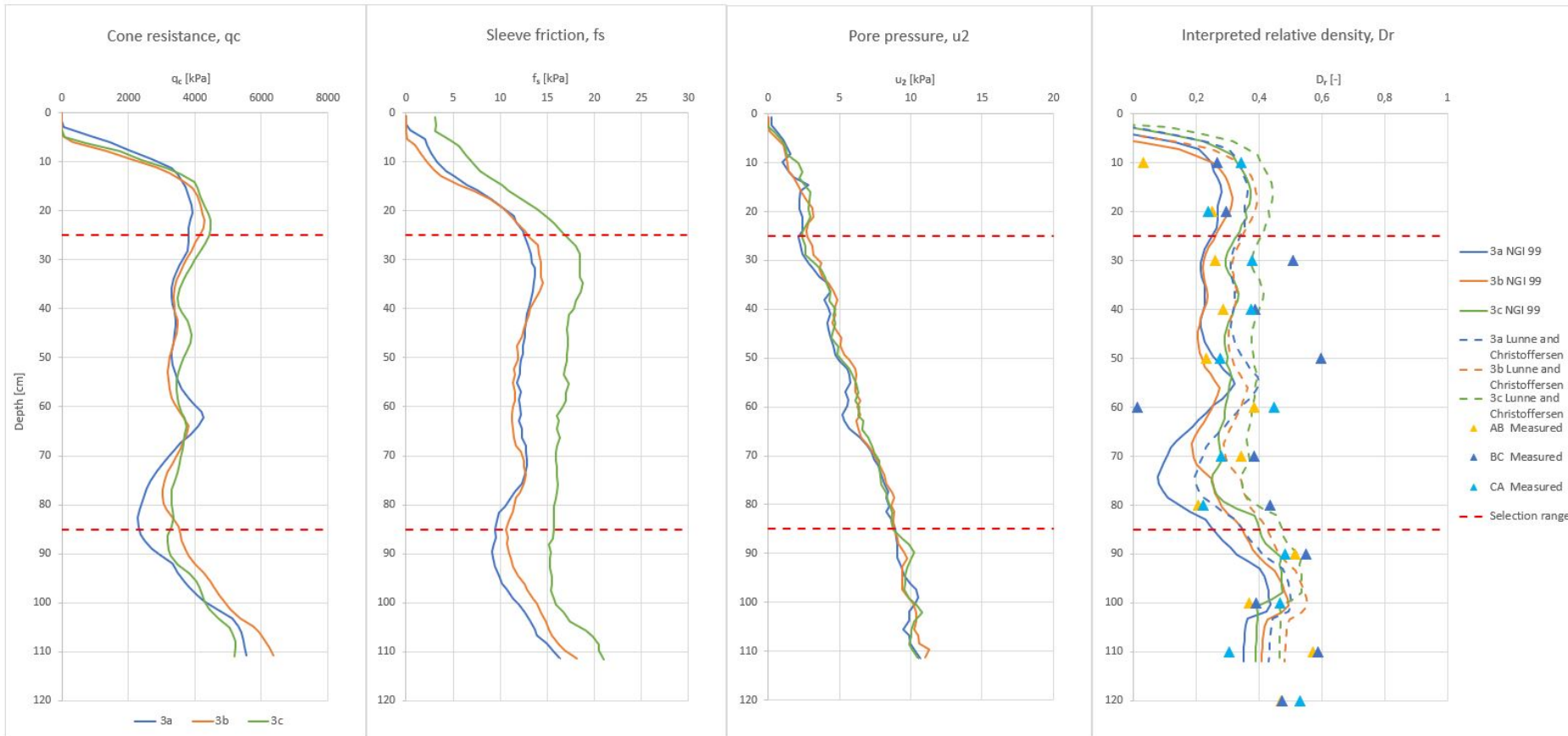**Figure 4.4:** CPTU profiles with $q_c$, $f_s$ and $u_2$ from experiment M3. Interpreted relative density, $D_r$, using the NGI99 approach (solid lines) and the method developed by Lunne and Christoffersen (1983) (dashed lines), in addition to the measured relative density from laboratory experiments (triangle). The selection range that will be used further in the analysis (from depth 25 cm to 85 cm) are shown in the figure.

## 4.2 Density tests

The results from the density samples taken during the excavation of the chamber are presented in this chapter in terms of relative density $D_r$ and void ratio, e. The void ratio is presented with the void ratio limits, $e_{min}$ and $e_{max}$ determined for the sand through procedures from DEGEBO and NGI.

As mentioned, the density results show some variations close to the top and bottom of the sample, and a selection range in the middle of the sample (depth 25-85cm) is chosen. The relative density and void ratio for the selection range of experiment M1, M2 and M3 are presented in figure 4.5, 4.6 and 4.7. The void ratio is also presented by an average void ratio of the three positions in the chamber, AB, BC and CA. The calculations and the results for the entire sample depth are presented in Appendix E.
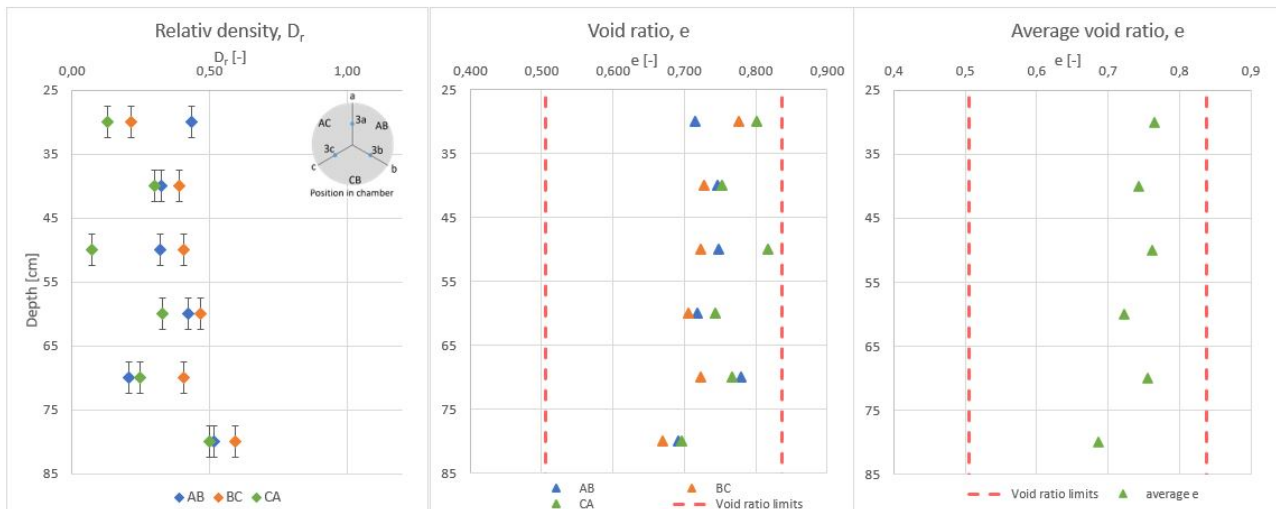


**Figure 4.5:** Measured relative density of selection range from cylinder samples taken during excavation of test chamber for experiment M1. Average value of void ratio based on measurements in section AB, BC, CA.
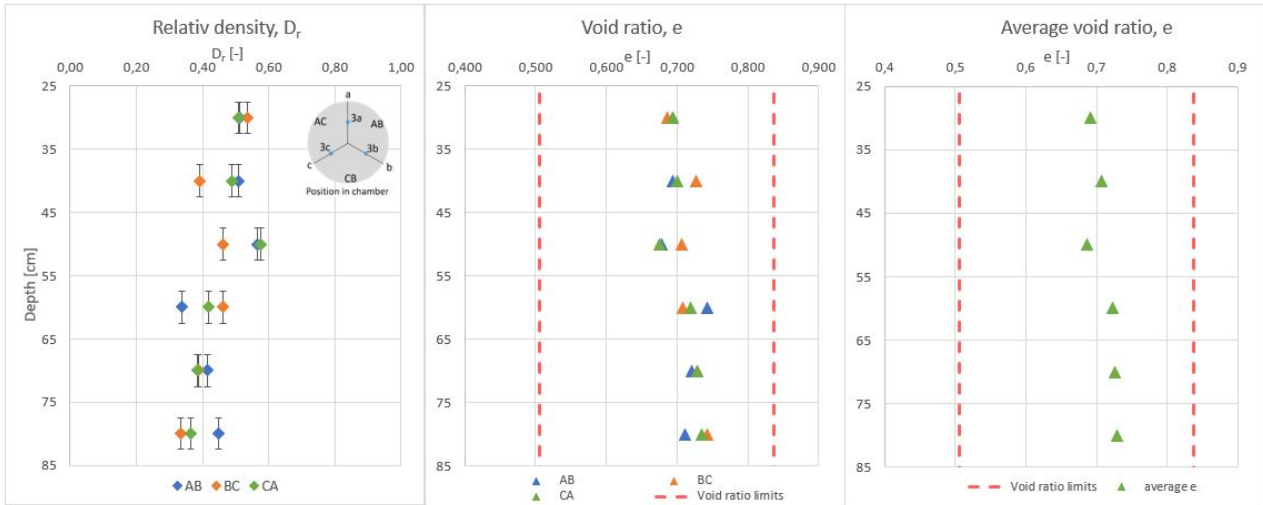
**Figure 4.6:** Measured relative density of selection range from cylinder samples taken during excavation of test chamber for experiment M2. Average value of void ratio based on measurements in section AB, BC, CA.
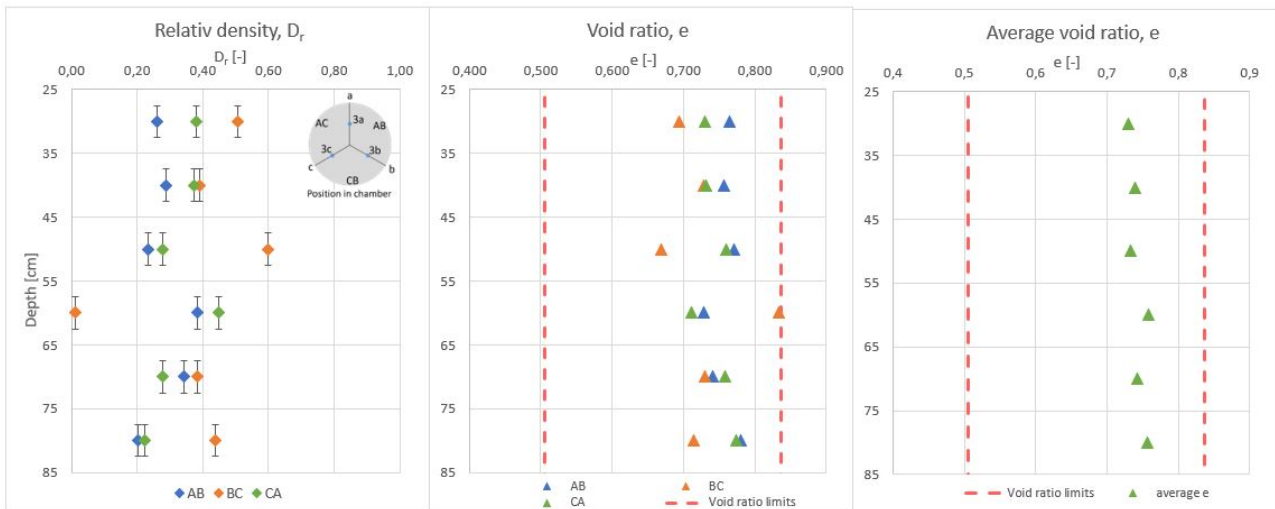


**Figure 4.7:** Measured relative density of selection range from cylinder samples taken during excavation of test chamber for experiment M3. Average value of void ratio based on measurements in section AB, BC, CA.

## 4.3 Interpretation of CPTU-data

### 4.3.1 Plastification angle, $\beta$

Based on the selected range, The plastification angle for experiments M1, M2 and M3, determined through back-calculation using NTH method is presented in figure 4.8. The plastification angle, $\beta$ for the entire sample depth is presented in Appendix D. It is calculated based on the interpreted bearing capacity factor, $N_q$, and interpolation of friction angle based on triaxial test results.
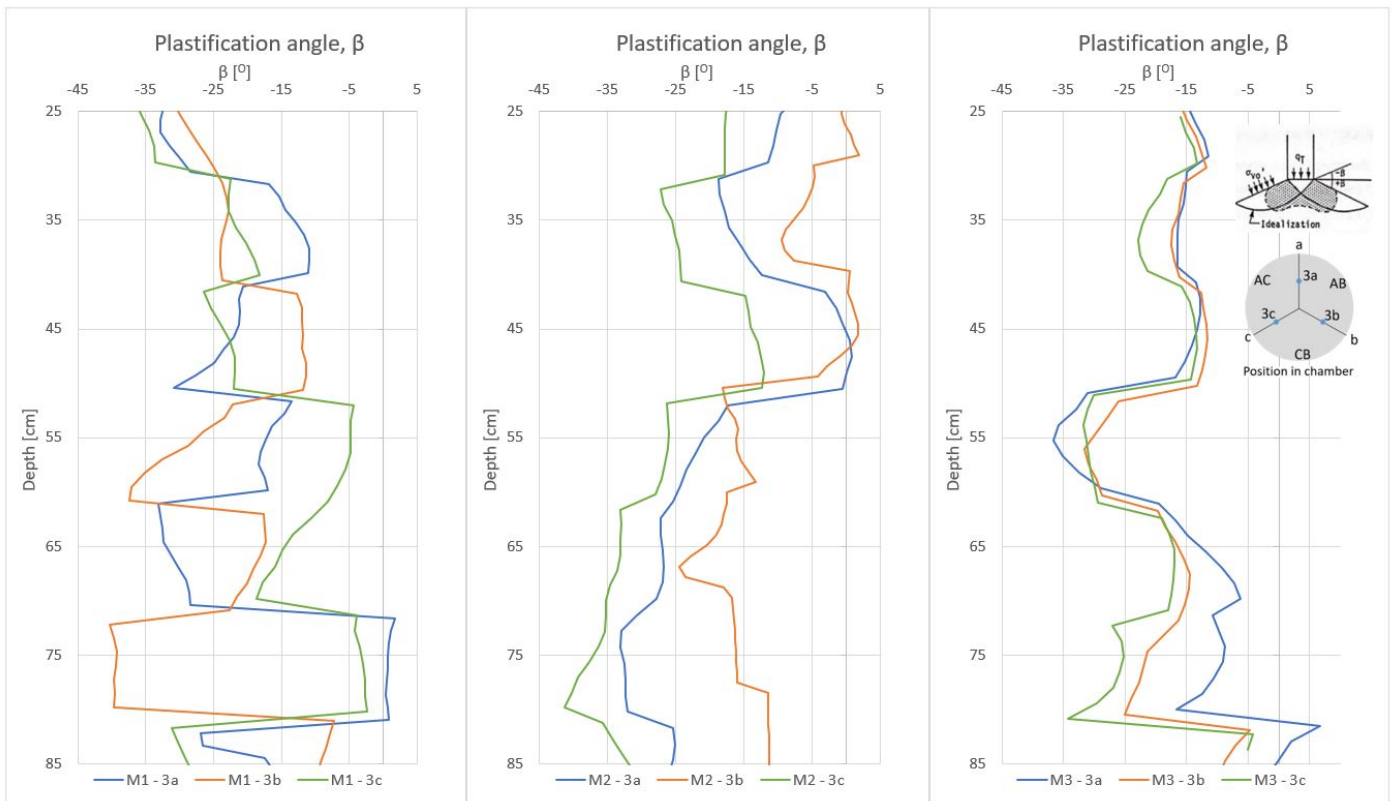


**Figure 4.8:** Determined plastification angle based on back calculation of $\beta$ using the NTH-method for Experiment M1 (left), M2 (middle) and M3 (right). The plastification angle is dependent on the friction angle from triaxial result interpolated based on measured void ratio in the chamber, and interpreted bearing capacity factor $N_q$ based on the NTH-method, which in turn is dependent on cone resistance and stress distribution in the chamber.

### 4.3.2 State parameter

**Critical state line**
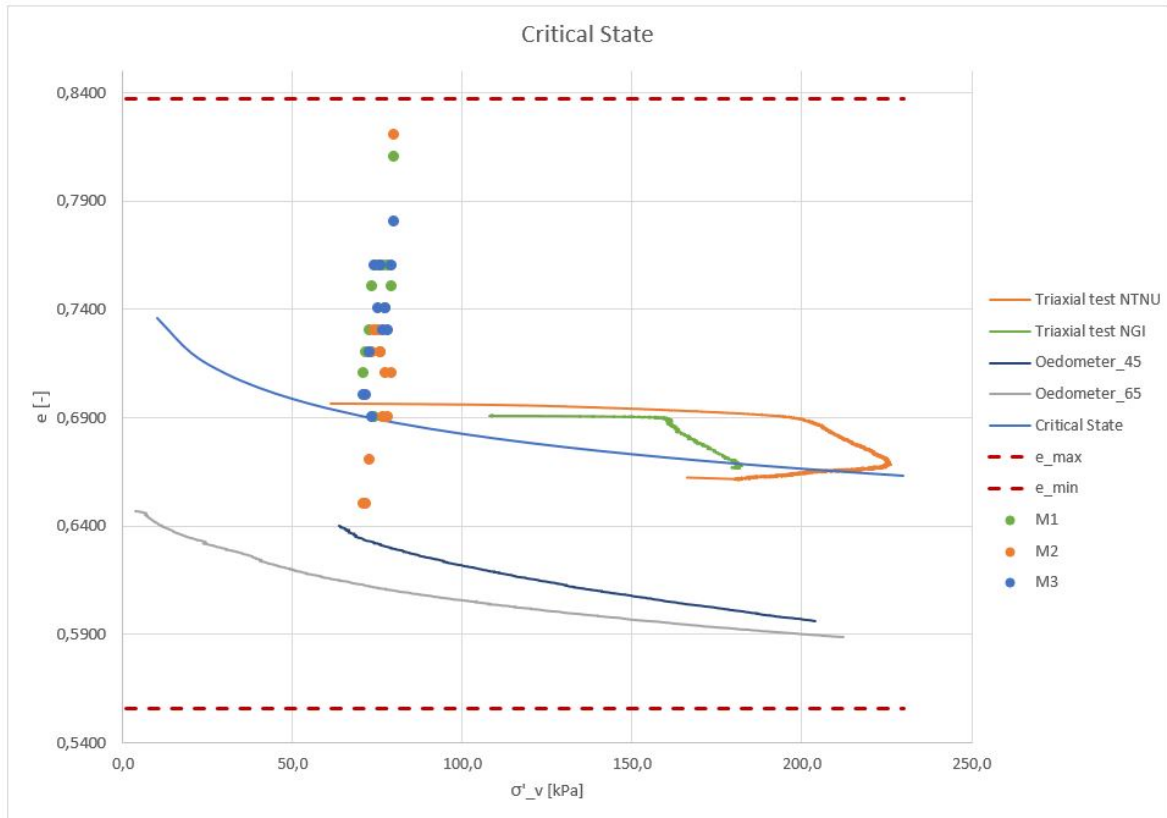


**Figure 4.9:** Critical state line for 0-2 sand from Søberg gravelpit in a $\sigma'_v$ - e plot. The critical state line is based on two triaxial tests from NTNU and NGI and two oedometer test from NGI. Two critical state points are given by the triaxial test and the inclination of the critical state line is given by oedometer results. This plot is a $\sigma'_v$ - e plot and the oedometer curves, the minimum and maximum void ratio and the state in the test chamber is plotted.
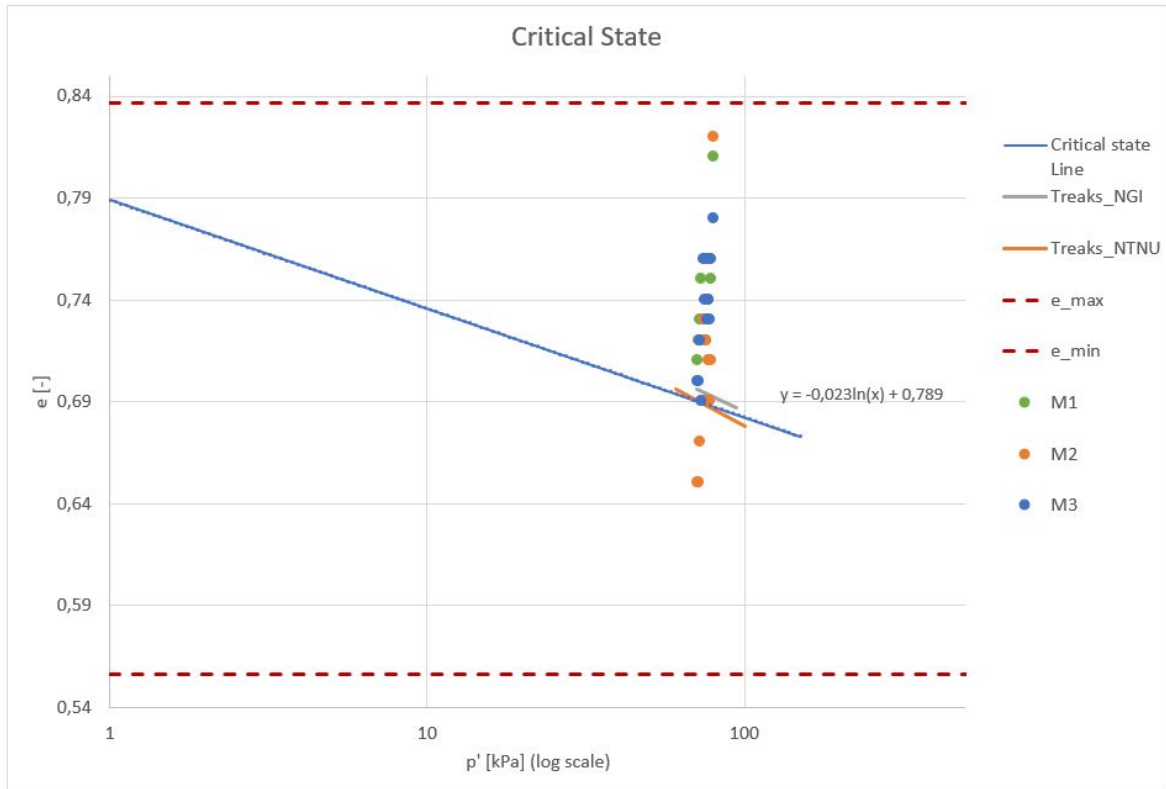
**Figure 4.10:** Critical state line for 0-2 sand from Søberg gravelpit in a p - e plot. The critical state line is based on two triaxial tests from NTNU and NGI and two oedometer test from NGI. Two critical state points are given by the triaxial test and the inclination of the critical state line is given by oedometer results. This plot is a p - e plot and the minimum and maximum void ratio and the state in the test chamber is plotted.

**State parameter**

The state parameter, $\psi_{BJ}$, is interpreted and determined using two methods. Firstly, the state parameter is interpreted through the state parameter approach, where Been et al. (1987) suggested an empirical correlation from cone resistance, presented in chapter 2.2.3. Secondly, the state is determined based on its definition, being the distance between the void ratio and the critical state line. This is determined based on the mean void ratios measured during excavation. The result of state parameter is presented in figures 4.11, 4.12 and 4.13 for experiment M1, M2 and M3, respectively. It is presented based on both methods for determining the state parameter. The state parameter for the entire sample depth is given in Appendix C.
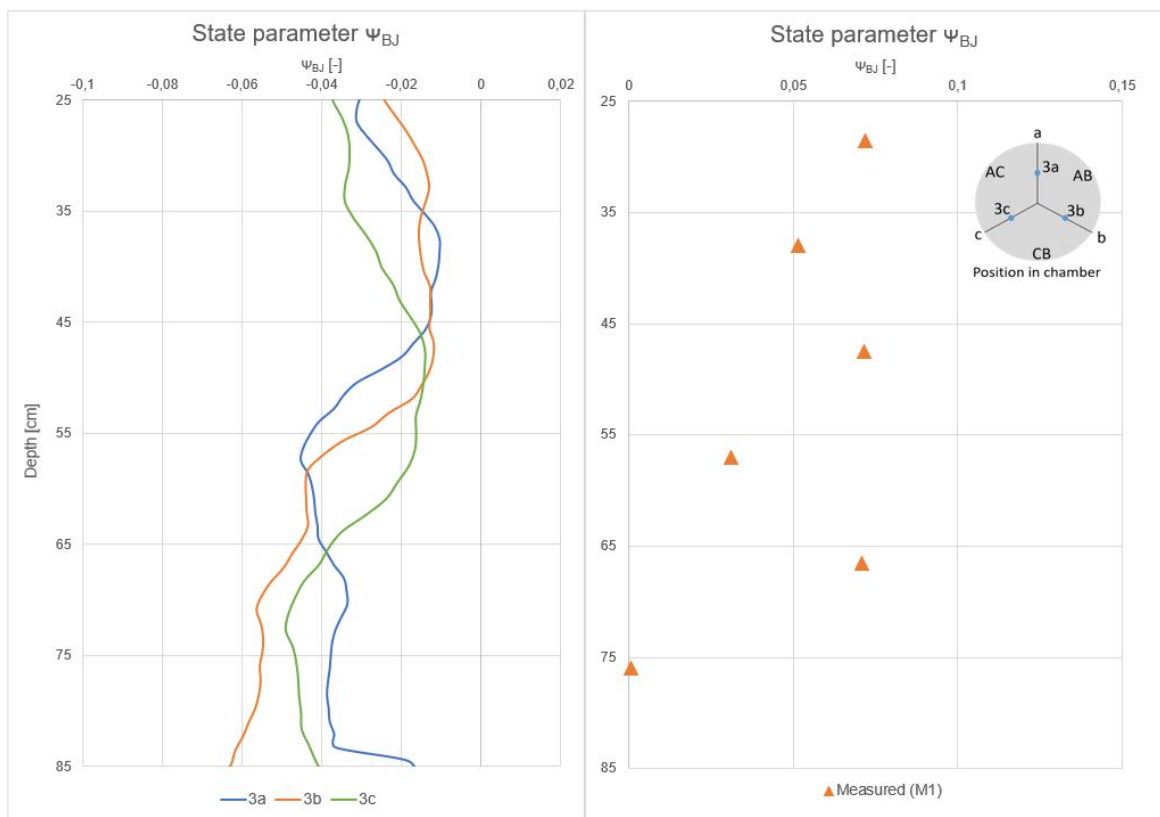


**Figure 4.11:** Determined state parameter for Experiment M1 based on the empirical correlation to cone resistance suggested by Been et al. (1987) (left) and determined state parameter from definition based on measured mean void ratio in chamber (right).
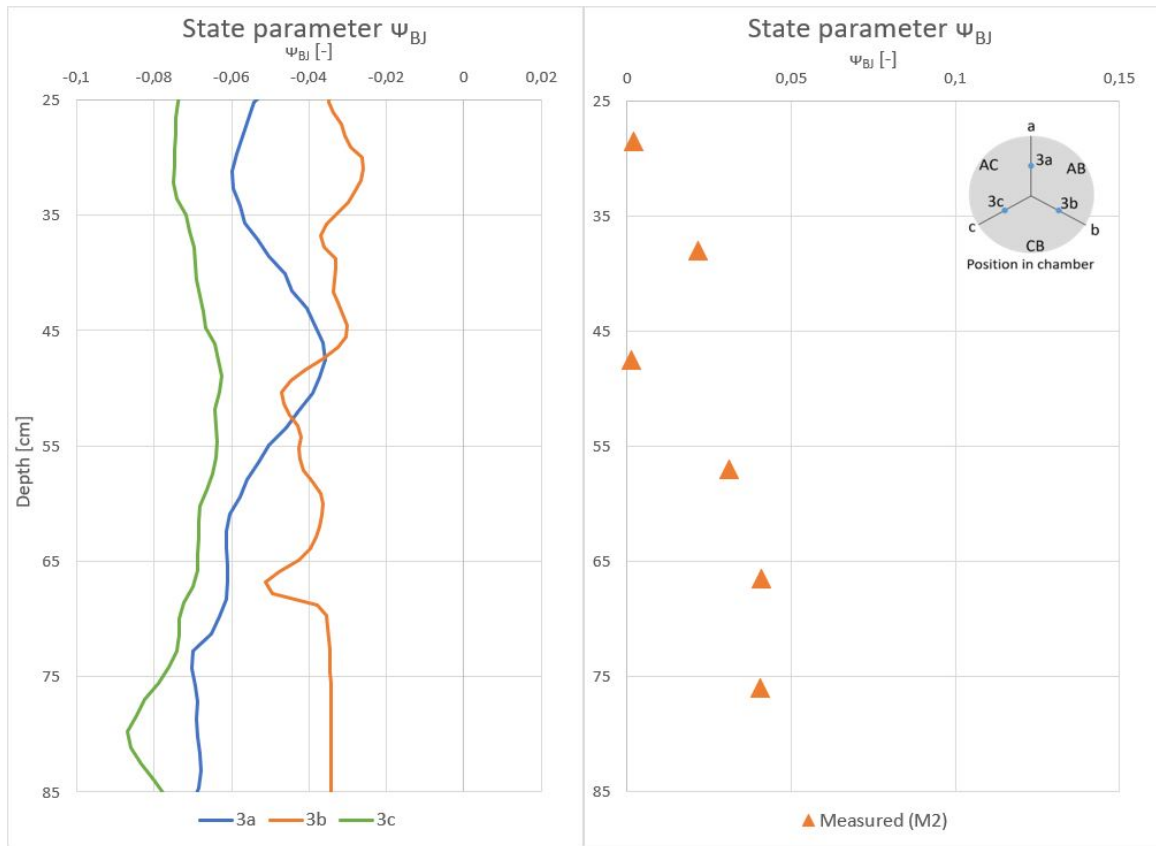
**Figure 4.12:** Determined state parameter for Experiment M2 based on the empirical correlation to cone resistance suggested by Been et al. (1987) (left) and determined state parameter from definition based on measured mean void ratio in chamber (right).
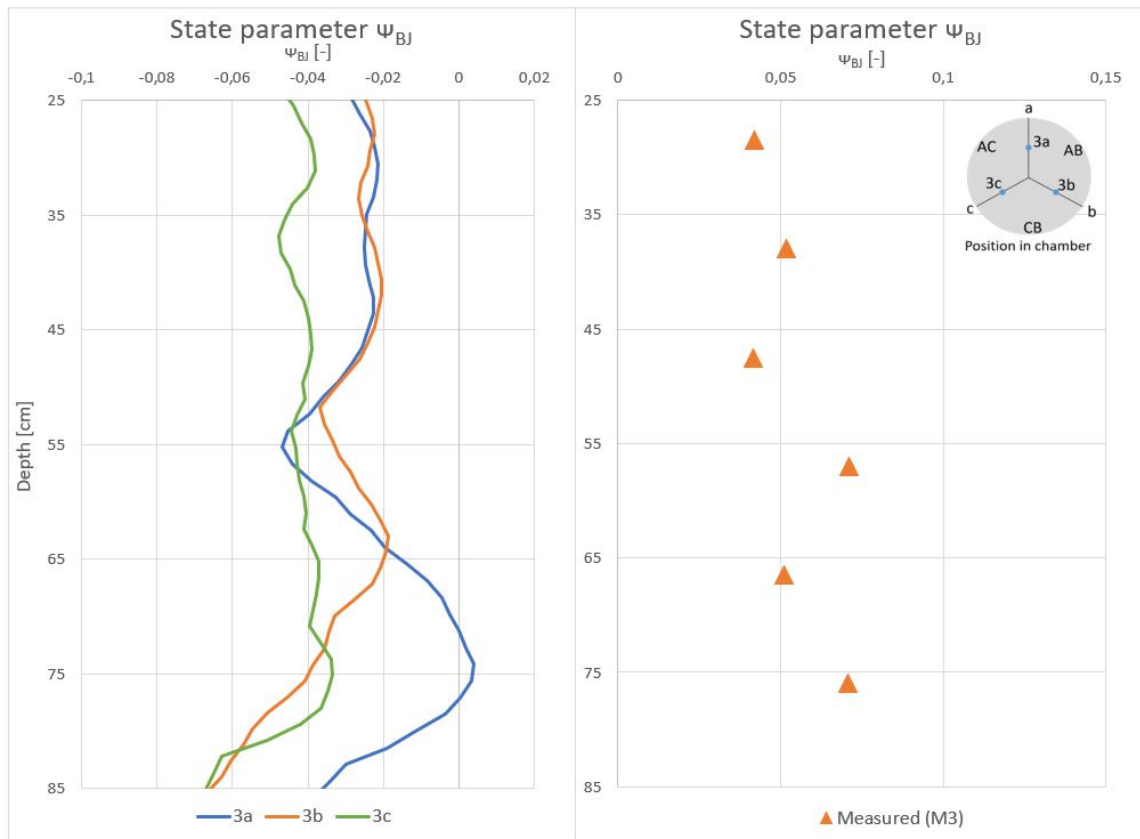
**Figure 4.13:** Determined state parameter for Experiment M3 based on the empirical correlation to cone resistance suggested by Been et al. (1987) (left) and determined state parameter from definition based on measured mean void ratio in chamber (right).

### 4.3.3 Bearing capacity diagrams from Janbu, $N_q - \tan(\phi)$ charts

The bearing capacity diagrams from Janbu are used to check if the data obtained fits the theory of the NTH method. Some of the data fit fairly good, especially for experiments M1 and M3. The results are slightly off compared to the experience-based relation in the shaded area suggested by Janbu and Senneset (1974).
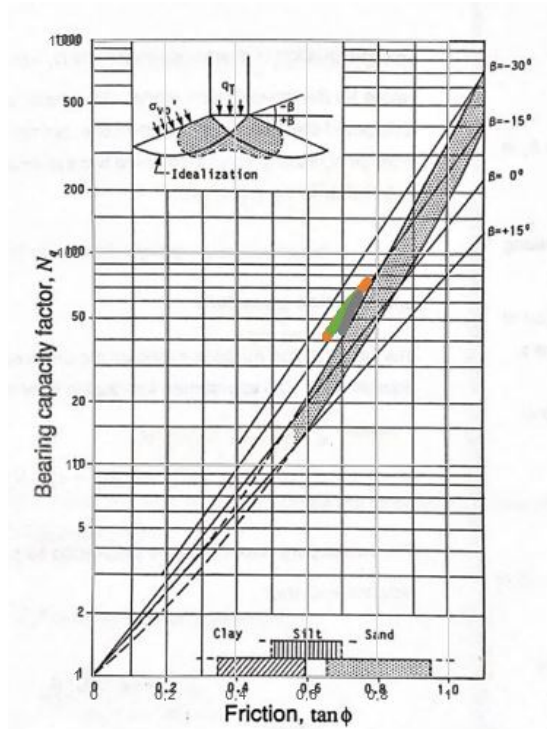
• M1_3a tan(φ) from Been and Jeff.  • M1_3b tan(φ) from Been and Jeff

• M1_3c tan(φ) from Been and Jeff.  • average tan(φ) from current study

**(a)**
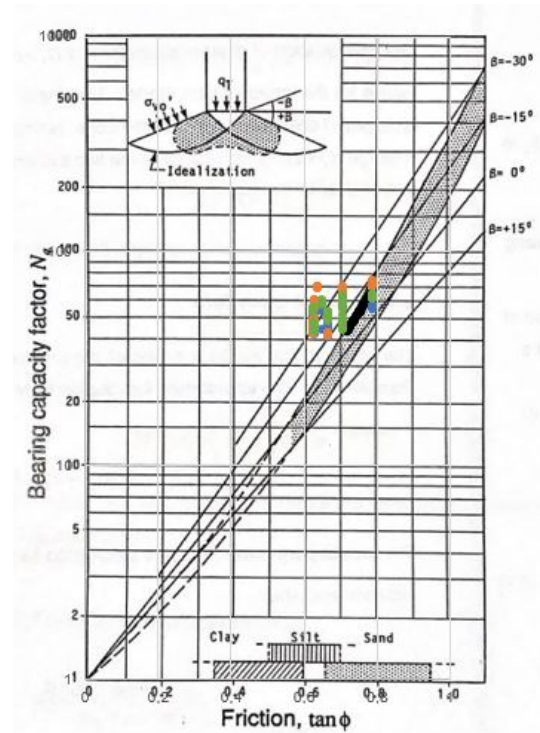
• Campanella  • M1_3a  • M1_3b  • M1_3c

**(b)**

**Figure 4.14:**

**(a)** The figure shows $\tan\phi$ estimated from the state parameter Been et al. (1987) plotted against $N_q$ for all the sections in M1. The average $\tan\phi$, based on the correlation from Figure 4.21 is plotted against $N_q$.

**(b)** The figure shows $\tan\phi$ estimated from triaxial test and interpolated with void ratio plotted against $N_q$ for all the sections in M1. $\tan\phi$ determined from the theory of P. Robertson and R. Campanella (1983) is plotted against $N_q$.
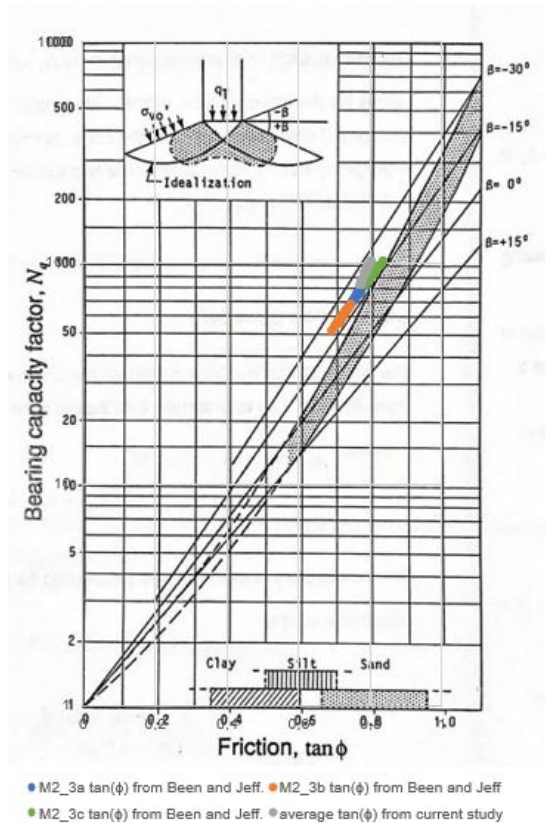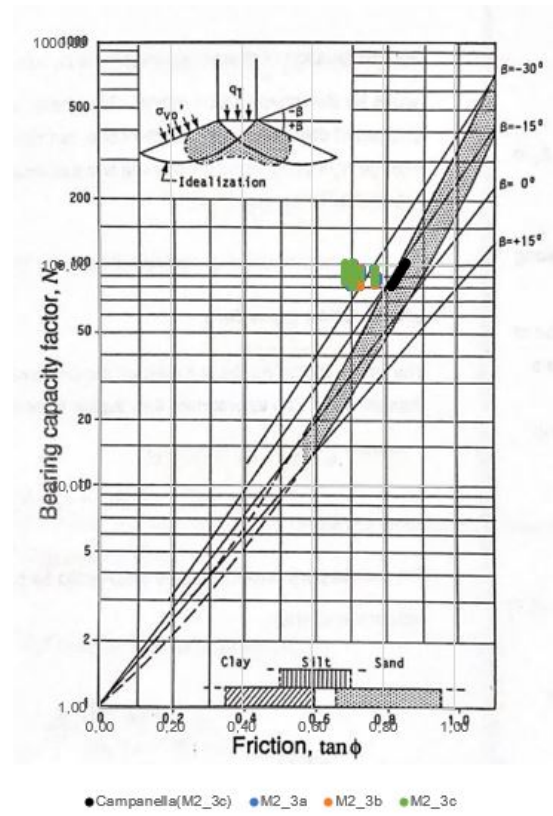
**(a)**  **(b)**

**Figure 4.15:**
**(a)** The figure shows $\tan\phi$ estimated from the state parameter Been et al. (1987) plotted against $N_q$ for all the sections in M2. The average $\tan\phi$ based on the correlation from Figure 4.21 is plotted against $N_q$.
**(b)** The figure shows $\tan\phi$ estimated from triaxial test and interpolated with void ratio plotted against $N_q$ for all the sections in M2. $\tan\phi$ determined from the theory of P. Robertson and R. Campanella (1983) is plotted against $N_q$.
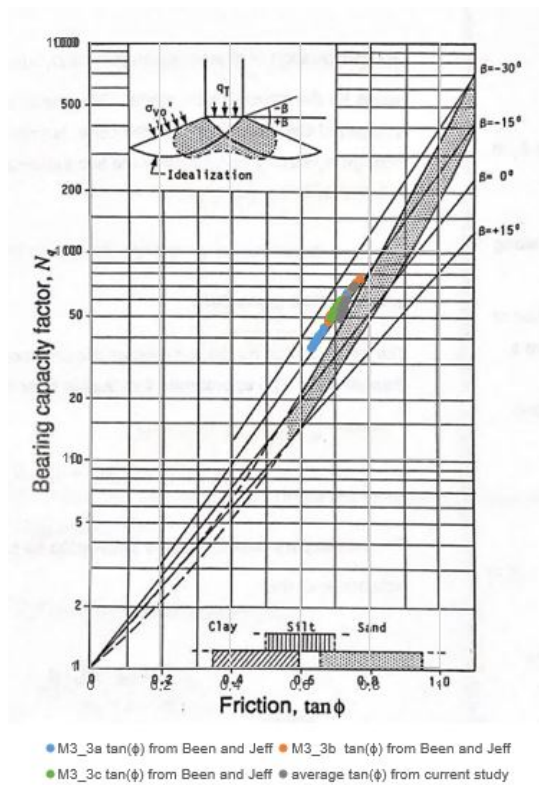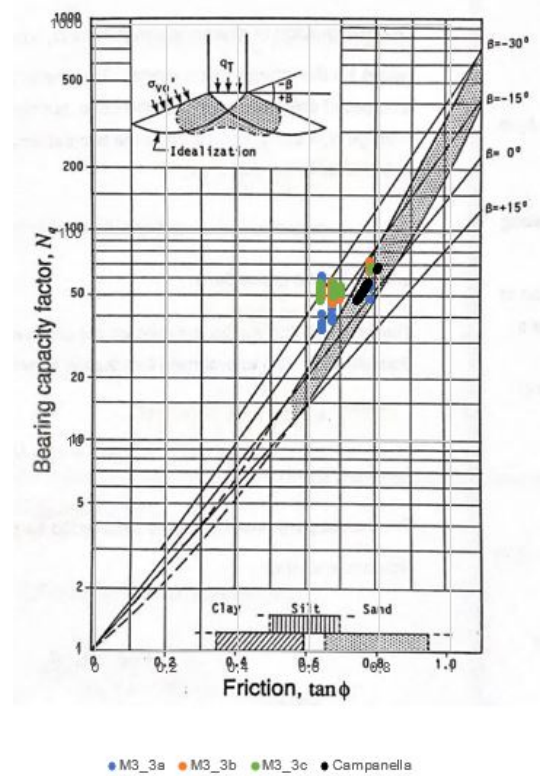
**(a)**                                                                 **(b)**

**Figure 4.16:**

**(a)** The figure shows $\tan\phi$ estimated from the state parameter Been et al. (1987) plotted against $N_q$ for all the sections in M3. The average $\tan\phi$ based on the correlation from Figure 4.21 is plotted against $N_q$.

**(b)** The figure shows $\tan\phi$ estimated from triaxial test and interpolated with void ratio plotted against $N_q$ for all the sections in M3. $\tan\phi$ determined from the theory of P. Robertson and R. Campanella (1983) is plotted against $N_q$.

### 4.3.4 Correlation between state parameter and plastification angle

The correlation between state parameter $\psi_{BJ}$ and plastification angle $\beta$ is presented in this chapter. The correlation is based on different methods of obtaining $\beta$ and $\psi_{BJ}$. The plastification angle is determined by back-calculation using the NTH method and calculating it from $\psi_{BJ}$. The state parameter $\psi_{BJ}$ is based on the formula given by Been et al. (1987) and the distance from the measured void ratio to the critical state line. The correlation is investigated for the chosen selection range of sample depth between 25 cm and 85 cm, and the figures show the correlation from measurements of all experiments M1, M2 and M3. Equation 4.1 expresses the state parameter for sand $\psi_{BJ}$, and equation 4.2 expresses the plastification angle determined from back-calculation using the NTH method. Equation 4.3 is the theoretical relation between $\beta$ and $\psi_{BJ}$, determined during this study. Calculating different $\beta$-values by using Equation 4.2 and Equation 4.3 generates very similar results. This support that a correlation between $\beta$ and $\psi_{BJ}$ exists.

$$\psi_{BJ} = -\frac{1}{(8,1 - ln\lambda ss)} * ln[\frac{q_c - p}{p'}(8 + \frac{0,55}{\lambda_{ss} - 0,01})^{-1}] \tag{4.1}$$

$$\beta = \frac{\pi \tan\phi \cdot \ln\left[\frac{N_q}{N_f}\right]}{2\tan\phi} \tag{4.2}$$

$$\beta = \frac{\pi}{2} - \frac{1}{2tan\phi}ln\left[\frac{p'ke^{-m\psi_{BJ}} + p - \sigma_{v0}}{N_f(\sigma'_{v0})}\right] \tag{4.3}$$

**Figure 4.17:** Correlation between plastification angle, $\beta$ and state parameter $\psi_{BJ}$. $\beta$ based on back-calculation using NTH-method. State parameter is based on empirical correlation to Cone resistance, $q_c$ suggested by Been et al. (1987). Showing results for experiment M1, M2 and M3.
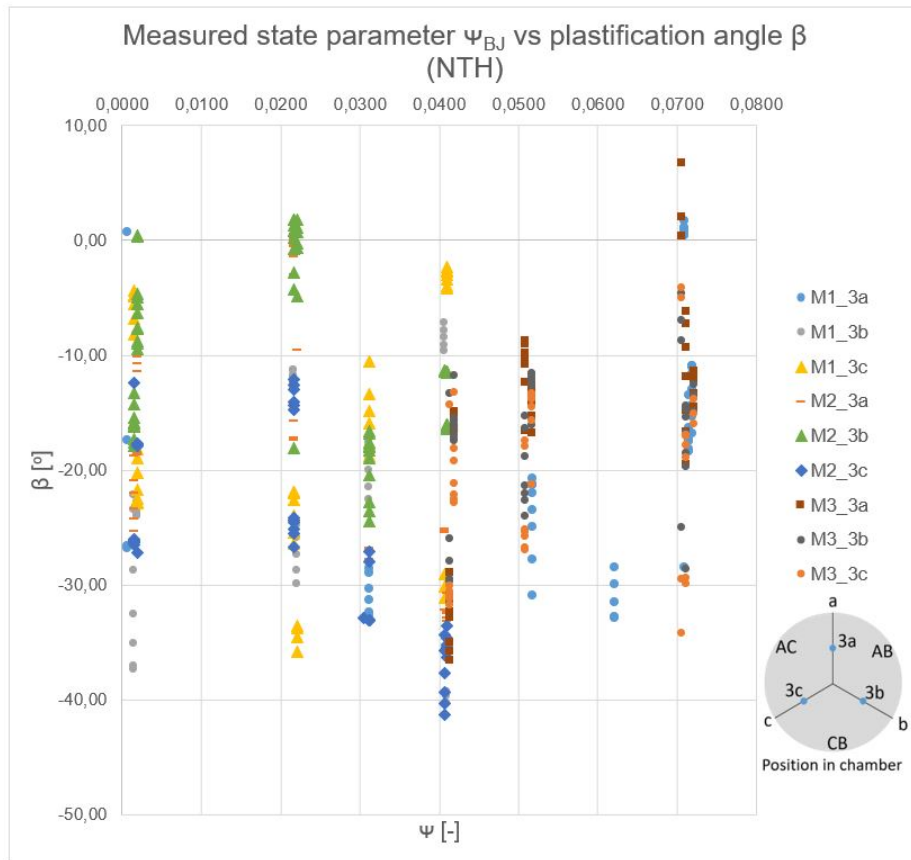
**Figure 4.18:** Correlation between plastification angle, $\beta$ and state parameter $\psi_{BJ}$. Plastification angel $\beta$ based on back-calculation using NTH-method. The state parameter $\psi_{BJ}$ is based on the distance from measured void ratio to the critical state line. Showing results for experiment M1, M2 and M3.
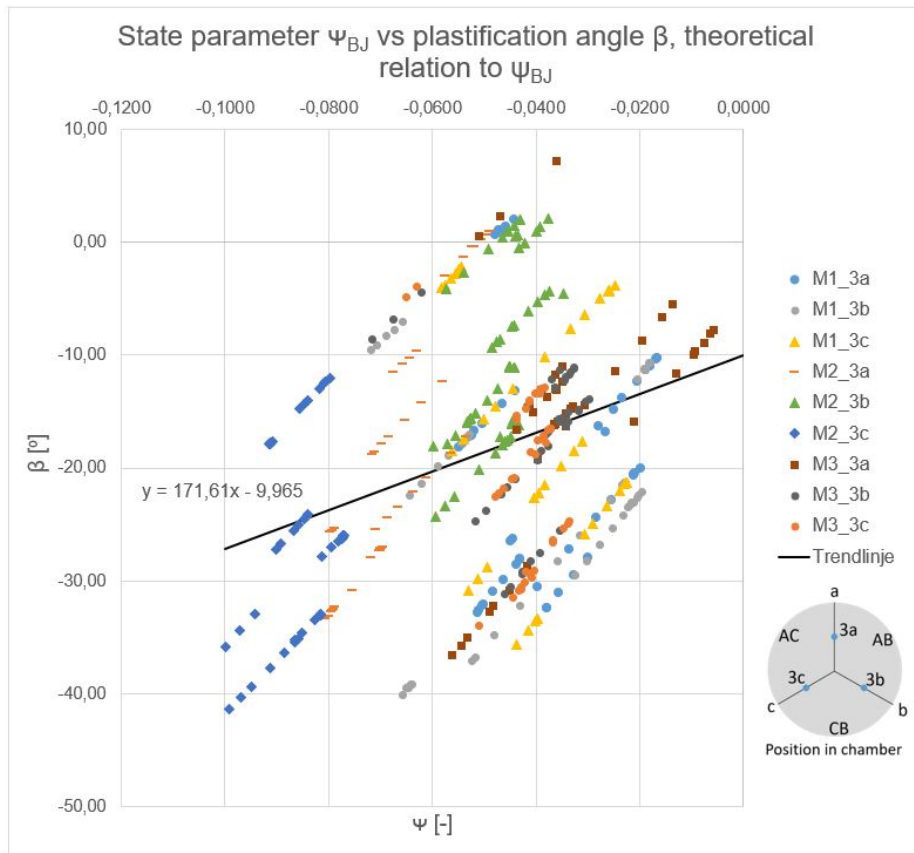
**Figure 4.19:** Correlation between plastification angle, $\beta$ and state parameter $\psi_{BJ}$. $\beta$ is calculated from $\psi_{BJ}$. State parameter is based on empirical correlation to Cone resistance, $q_c$ suggested by Been et al. (1987). Showing results for experiment M1, M2 and M3.
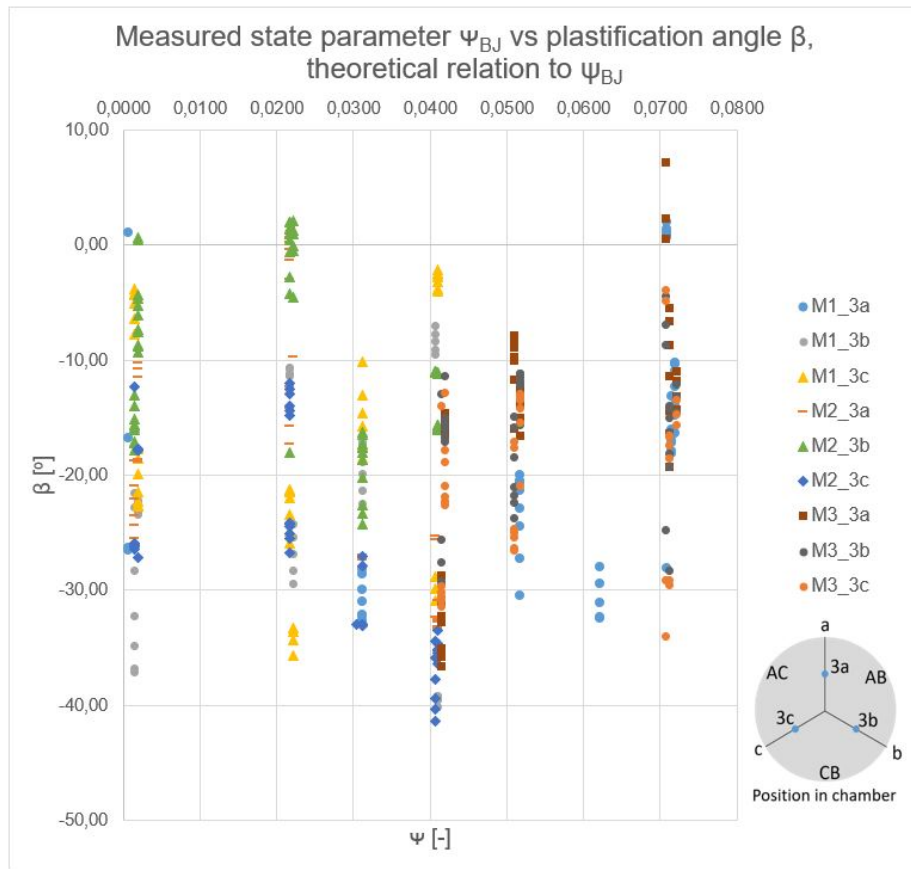
**Figure 4.20:** Correlation between plastification angle, $\beta$ and state parameter $\psi_{BJ}$. $\beta$ is calculated from $\psi_{BJ}$. The state parameter $\psi_{BJ}$ is based on the distance from measured void ratio to the critical state line. Showing results for experiment M1, M2 and M3.
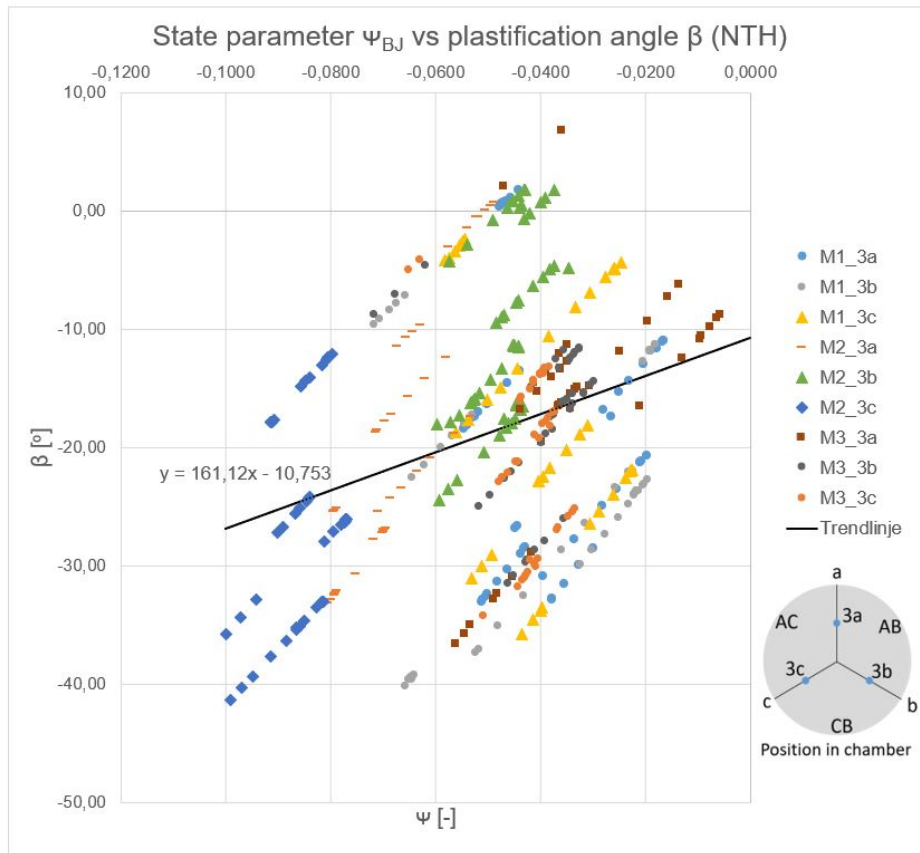
## 4.4    Correlation between state parameter and friction angle

The correlation between the state parameter and friction angle is presented in figure 4.21. The friction angle is determined from interpolation of triaxial results based on measured void ratio in the chamber through sampling. The state parameter is determined through the state parameter approach suggested by Been et al. (1987). It is presented for the 25-85 cm depth selection range for each experiment M1, M2 and M3.
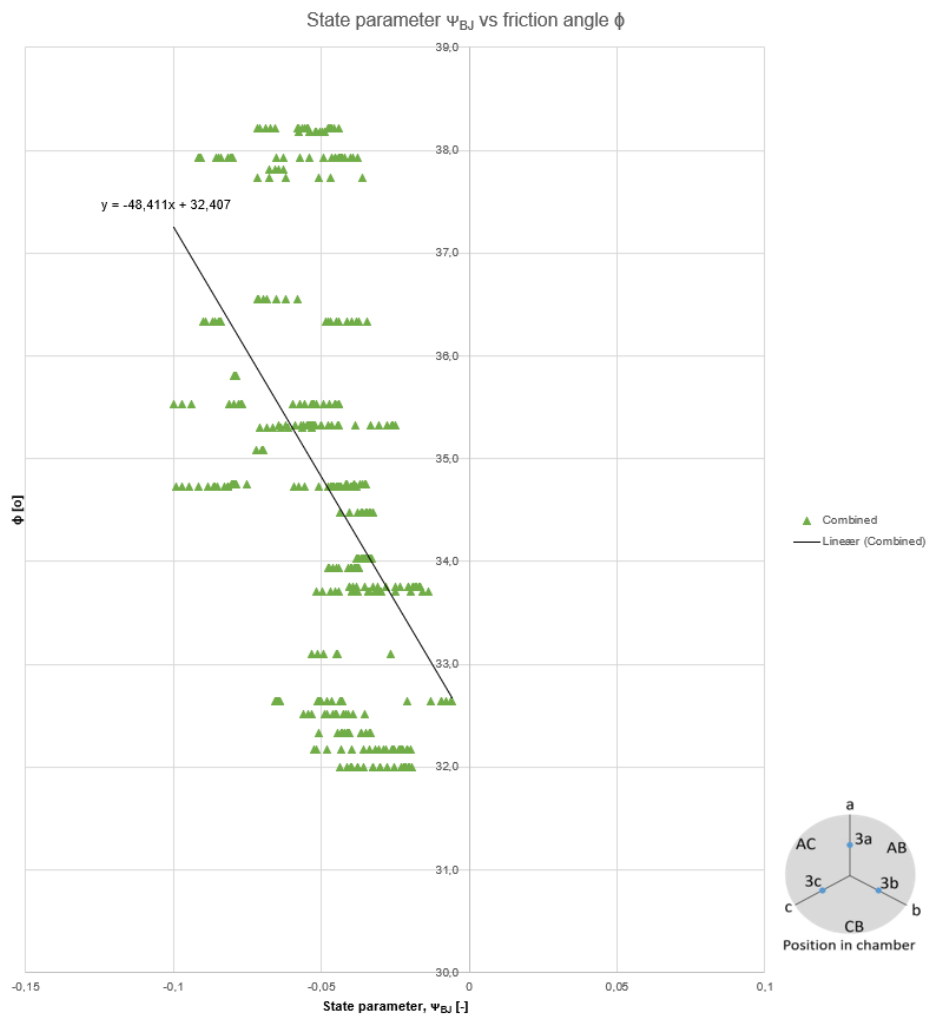


**Figure 4.21:** Correlation between state parameter, $\psi_{BJ}$ and friction angle $\phi$. Friction angle based on triaxial result and the state parameter is based on empirical correlation to cone resistance, $q_c$ suggested by Been et al. (1987). Showing results for experiment M1, M2 and M3.

## 4.5 Stress distribution in chamber

In this section, the results from the earth pressure cells are presented. Figures 4.22, 4.23 and 4.22 show the vertical and horizontal stresses in the chamber based on the readings from the pressure cells. These results are also the basis for calculating the lateral earth pressure coefficient, $K_0$. Based on the measurements, $K_0$ is determined to be approximately 0.5 for all the experiments.
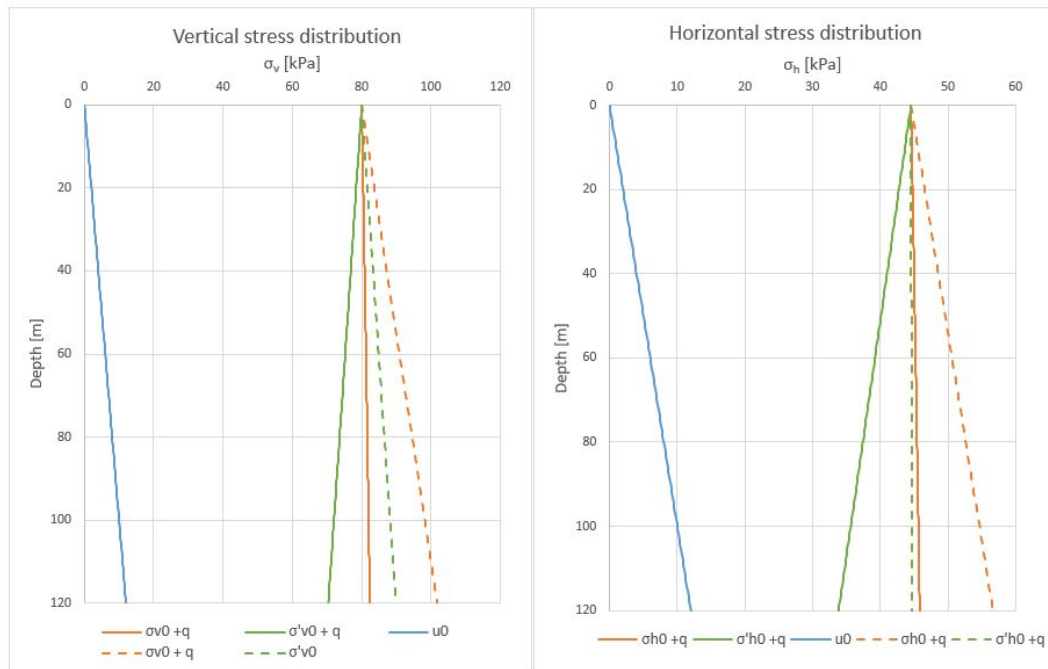


**Figure 4.22:** Stress distribution in test chamber for experiment M1. Showing idealized stress distribution with no friction along chamber wall, r=0 (dashed line) and stress distribution measured in chamber including the boundary effects on the wall (solid line).
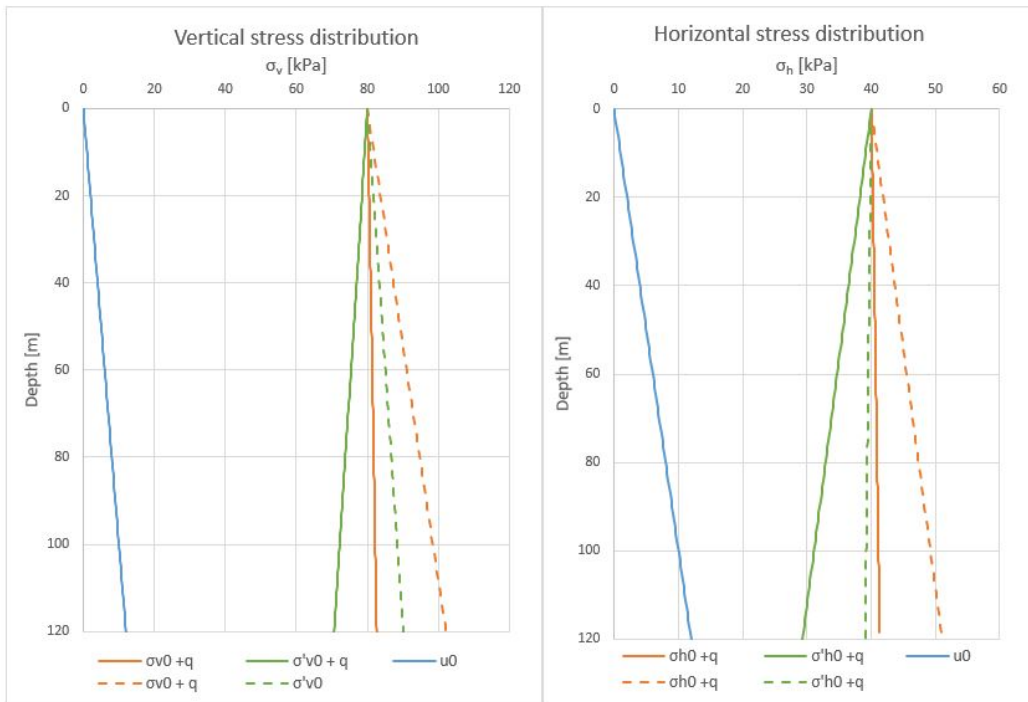
**Figure 4.23:** Stress distribution in test chamber for experiment M2. Showing idealized stress distribution with no friction along chamber wall, r=0 (dashed line) and stress distribution measured in chamber including the boundary effects on the wall (solid line).
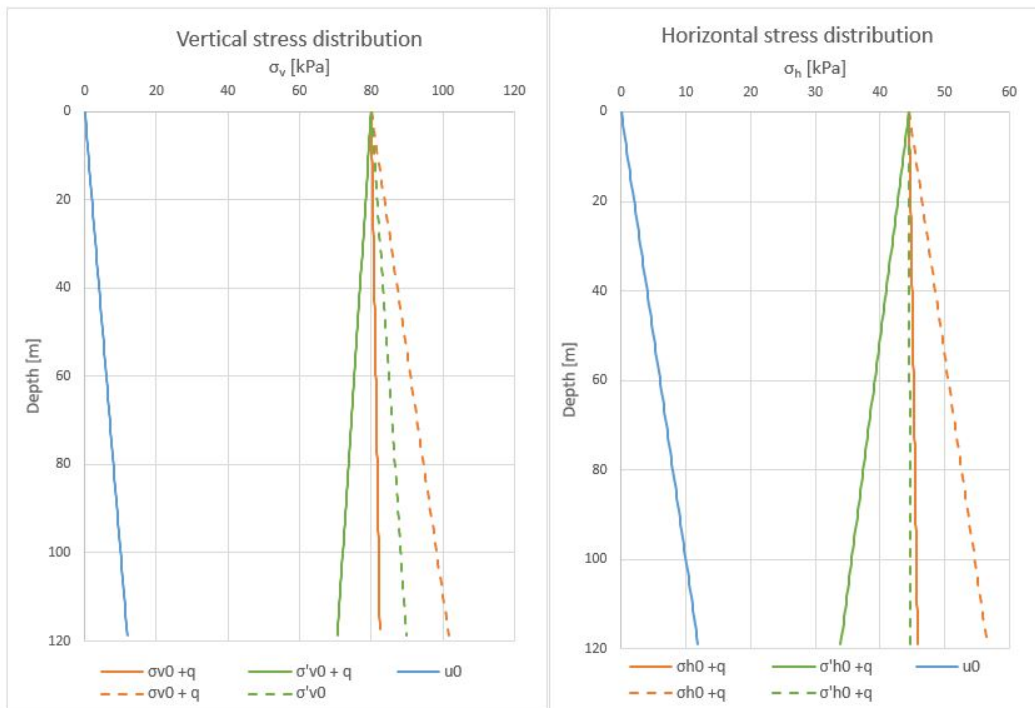


**Figure 4.24:** Stress distribution in test chamber for experiment M3. Showing idealized stress distribution with no friction along chamber wall, r=0 (dashed line) and stress distribution measured in chamber including the boundary effects on the wall (solid line).

### 4.5.1 Oedometer test results

In this chapter, some of the oedometer results are presented. The rest of the plotted results can be found in Appendix A. The oedometer tests were conducted at NGI's laboratory in Oslo. This is an experienced laboratory, and the routines are very well established. The oedometer results are used to determine the modulus number for the sand in the range from $0 - 200kPa$. The modulus number is further used to calculate the flexibility parameter $\lambda$ after equation 2.32. The calculated flexibility parameter, $\lambda$, equals 0.0231.
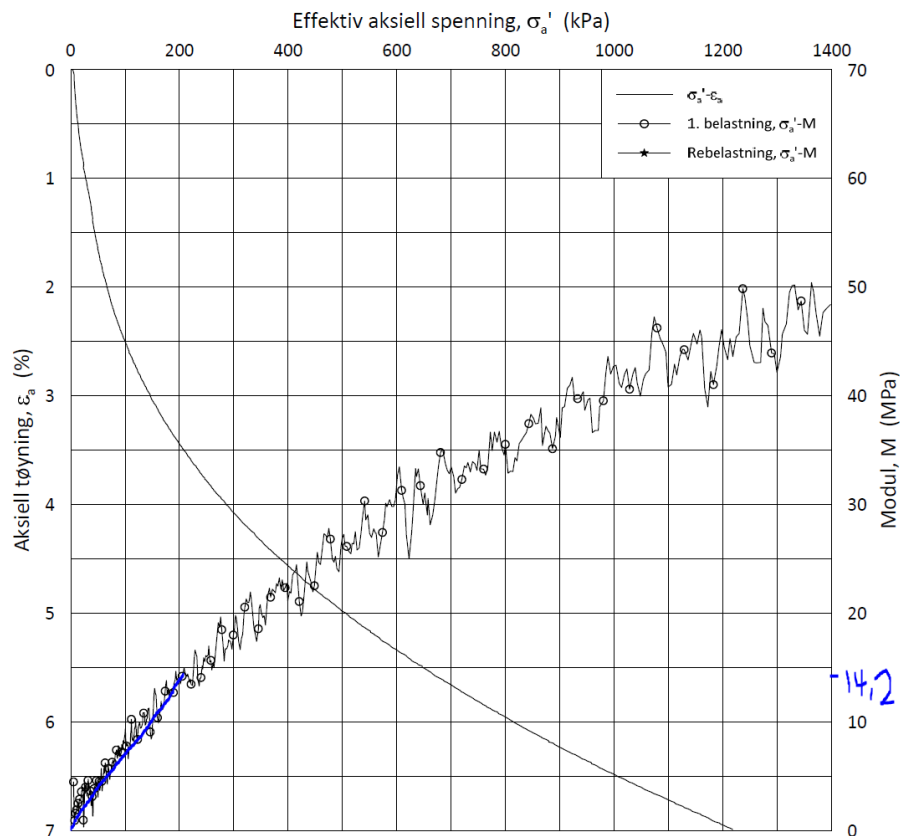


**Figure 4.25:** $\sigma'_a \, vs \, Modul, M$ plot from oedometer test conducted at NGI in Oslo. The build-in void ratio was 0.64 and the blue line drawn in the plot, is the line used to calculate the modulus number.

### 4.5.2 Results from the Material point method

An attempt was made to interpret the plastification angle, $\beta$, from the observed stress field, based on different states in terms of dilatancy angles, but no clear identification was observed. The affected area under the cone seems to vary in size for the different dilatancy angles, but this can not confirm or refute the empirical results. The results show that the different dilatancy angles cause the material to dilate or contract on the surface. For dilatancy angle equal to $3°$ the surface is lifted upwards when penetrating the cone. When the dilatancy angle is equal to $-3°$ a sinking can be observed in the surface, and the material contract. For a dilatancy angle equal to zero, the surface has a slight sinking, and it seems to be just in between the other two.
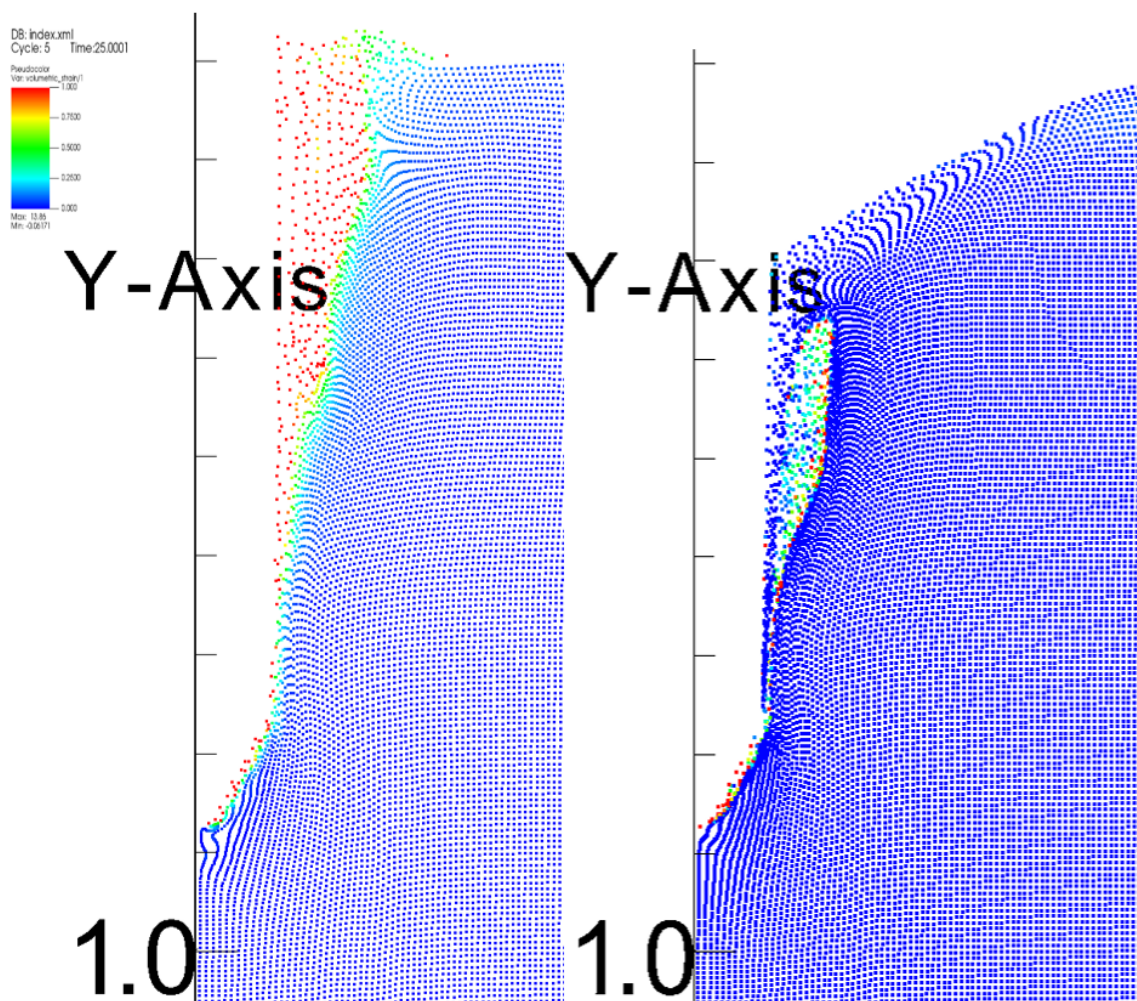


**Figure 4.26:** The volumetric strain is drawn for the analytical solution conducted with MPM. To the left the dilatancy angle is $3°$ and to the right the dilatancy angle is $-3°$
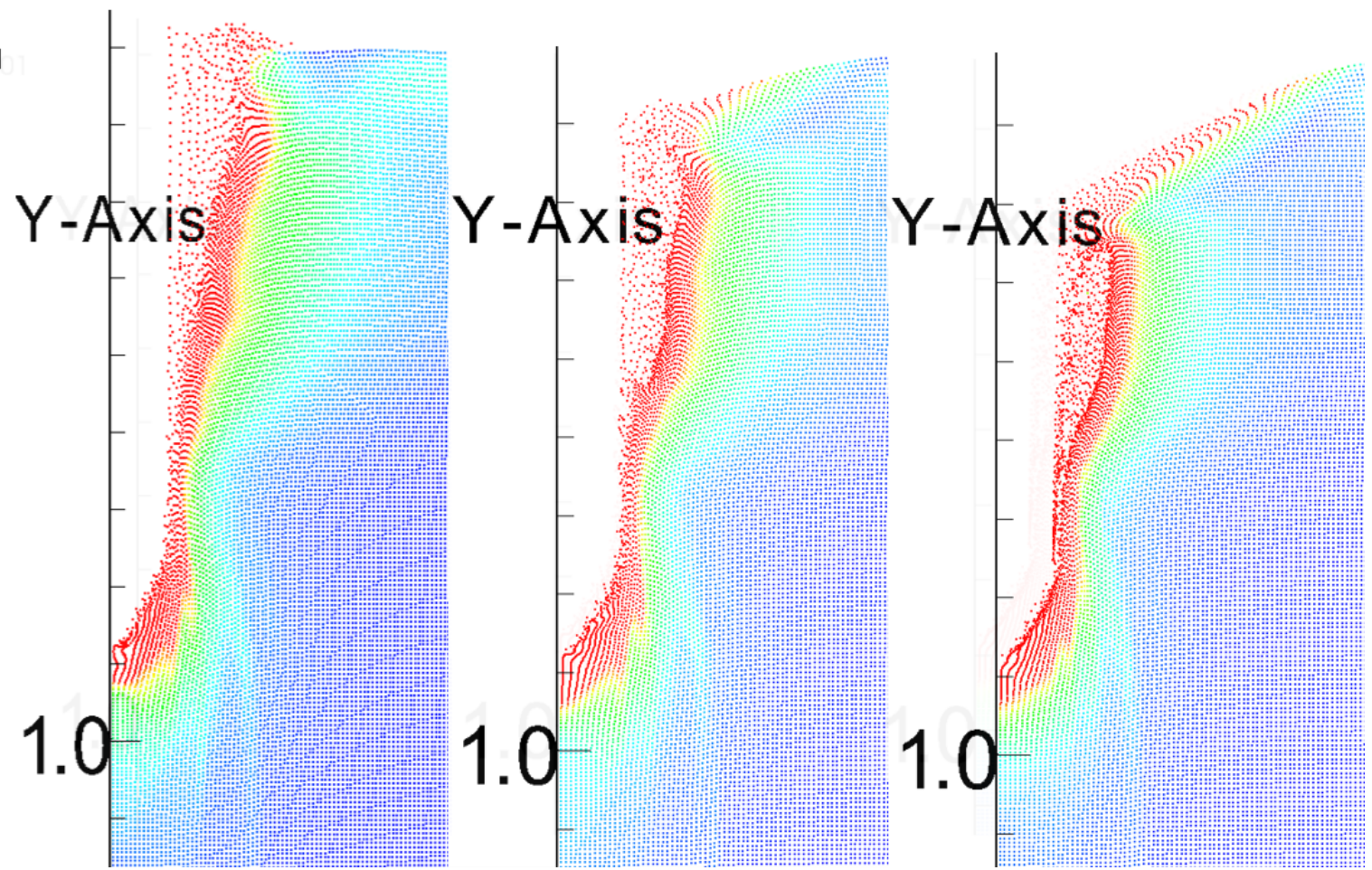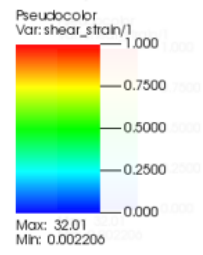
**Figure 4.27:** The shear strain is drawn for the analytical solution conducted with MPM. To the left the dilatancy angle is 3°, in the middle the dilatancy angle equal zero and to the right the dilatancy angle is −3°

# Chapter 5

# Discussion

This chapter will present a discussion of the results and the objectives of this study. The chapter is divided into three sections. Firstly, the laboratory set-up and procedures will be addressed, and how it affects the results. Secondly, a discussion of the cone penetrometer testing in sand will be presented. Lastly, a discussion of the analysis of sand behaviour around the cone tip will be given. This section will be divided into an analysis based on the laboratory work and the numerical analysis using the Material point method. All three sections will be a discussion of the results and the objectives of this project.

## 5.1 Laboratory set up and sample construction

### 5.1.1 Sample construction

Hammer (2020) and Skrede (2021) developed good methods for building in a large scale chamber sample of sand. However, there are a lot of uncertainties associated with a reconstituted sand sample in a chamber. Firstly, it is challenging to obtain a homogeneous sample in terms of relative density. The relative density is an important parameter for CPTU interpretation, being a controlling parameter for the interpretation of the friction angle when using the CPTU-test. Using the methods developed by Hammer and Skrede, an attempt to create three homogeneous sand samples with different relative densities was made. However, to achieve the exact desired relative density and a more homogeneous sample, the sand would first have to be weighed, which is challenging for the large amount of sand used in the sample.

Instead, for the first experiment, M1, the compaction time was calculated and increased per layer to avoid over-compaction at the bottom of the chamber. The compaction time was increased for experiments M2 and M3 to achieve greater relative density for the next experiments. After the excavation and sampling of density, an over-compaction of the sand at the bottom of the chamber was observed. This

95

is also reflected in the resulting cone resistance of the two experiments, as it increases with depth at the bottom of the sample. This is shown in figures 4.3 and 4.4. For further studies in the research project at NTNU, it would be beneficial to develop methods for weighing the sand prior to sample building. At the top of the sample, the relative density is also higher due to the extra overburden load applied to simulate in situ conditions with higher earth pressure. The build-in procedure may explain the variations in sample density and void ratio. When building in the sample, the sand is shovelled into the chamber, and the sand gets more packed in the area where the sand gets piled when shovelling. When using the plate vibrator, it is hard to keep the vibrator for an equal amount of time over the whole area. When emptying the water after saturation of each layer, it is hard to know when the water level is low enough to start vibrating. Sometimes the water level was too high, and when starting the plate vibrator, the water rose to the surface, the applied stress was taken by the pore pressure, and the effective stress was not increased as much as desired.

### 5.1.2   Boundary conditions in chamber and pressure cells

A second challenge when running tests in a chamber is the boundary effects along the chamber wall, making it challenging to simulate in situ conditions effectively. These boundary effects are illustrated through Janssen's formula for the silo effect in chapter 4.5. The pressure reading after the imposed load of 80 kPa is presented in figures 4.22, 4.23 and 4.24. The results show that the effective vertical stress in the chamber is slowly decreasing with depth due to the silo effects. A slight increase can be observed in the total vertical stress. To minimize the boundary effects, the chamber was treated with epoxy coating, and a plastic lining was added to the chamber wall. The plastic lining was implemented in two layers, with a low friction grease between the two plastic layers. When the sand was being compressed to achieve the desired density, the outer plastic lining was loosened such that the lining would work as a floating ring minimizing the friction working on the wall. This showed to be effective as a decrease of the silo effect can be observed after the plastic lining was implemented. This is illustrated in figure 5.1. The Figure shows a comparison of the vertical stress distribution of experiment F1 conducted in conjunction with TBA 4510 Specialization project and the stress distribution of experiment M3 conducted during this current study.
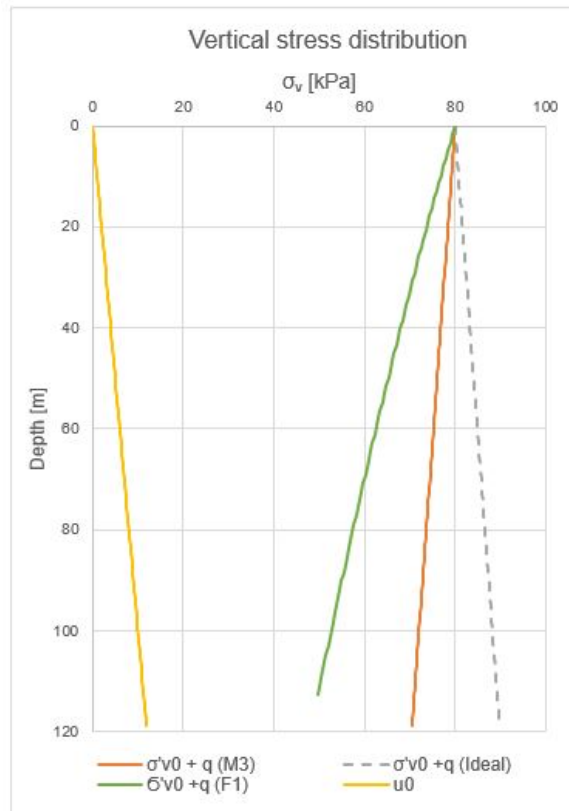
**Figure 5.1:** Comparison for plastic lining vs. no plastic lining. Stress distribution from experiment F1 (from preliminary project) without plastic, and experiment M3 with plastic added. Shows clear improvement of the silo effect in the chamber from adding plastic lining.

Skrede (2021) emphasized the impact of sensitivity drift affecting the readings of the earth pressure cells as described in chapter 3.2.4. To limit this, the water reservoir was implemented to sustain constant temperature and ambient conditions in the chamber. In addition, the temperature measurement was installed so that any change in temperature could be observed. As shown in figure 5.2, this was seemingly effective, as the sensitivity drift decreased after implementing these procedures relative to the sensitivity drift observed by Skrede (2021) in figure 3.9.
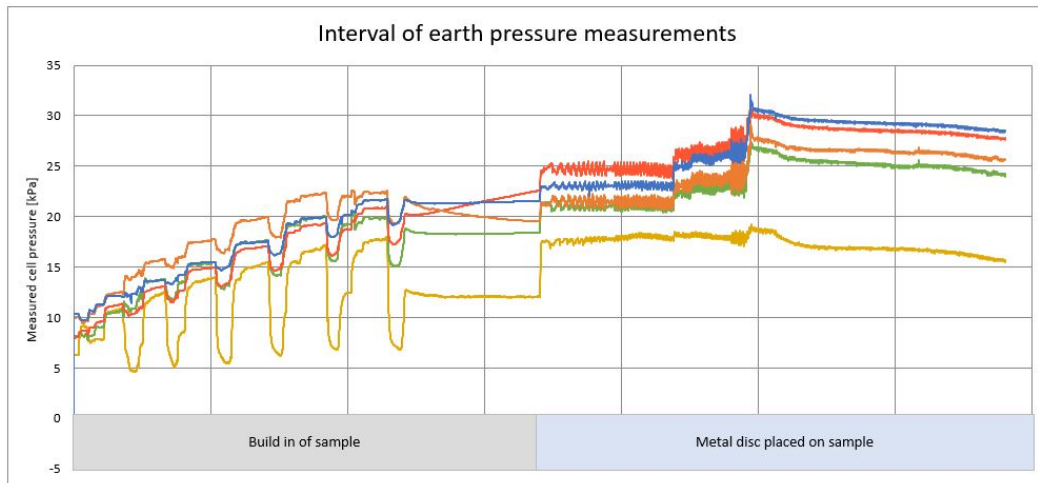
**Figure 5.2:** Earth pressure readings during sample building. Shows less sensitivity drift after water reservoir was implemented.

Some noise was observed in the measured earth pressure when the sounding equipment was installed in the chamber. Time was spent investigating and trying to eliminate this effect, but with no success. To avoid the effects from the registered noise, an average of the pressure readings were used when calculating the stress distribution in the chamber.

### 5.1.3 Challenges related to filling of water

Even though the implementation of a plastic lining led to a decrease in the arching effects in the chamber, the implementation of the plastic lining in the chamber was not without complications. When saturating the sample, water was collected between the two plastic sheets. The plastic started to warp inwards due to the volume and weight of the water. In some cases, water was overflowing at the top of the plastic lining into the sample, causing a disturbance of the sample close to the perimeter of the sample. In a future project, this has to be addressed.

**(a)**                      **(b)**

**Figure 5.3:** Fig 5.3a: The plastic lining leading to a collection of water between the two layers along the wall, disturbing the sample close to the chamber wall. 5.3b: Plastic lining warping due to water collection.

During the experiments, leakage occurred between the two chamber elements. During the first experiment, M1, the leakage was small and was believed to be due to the plastic lining being attached with tape along the edge of the bottom chamber, causing water to travel along the tape. Therefore, no other measures than attaching the plastic further away from the joints were therefore made for the next experiment. For experiment M2, the leakage was greater, and the filling of the chamber became time-consuming. The rubber ring between the two chamber elements was replaced for the next experiment, M3, but it was inefficient. With further investigation of the water leakage, it seemed to be a defect in the top element. The leakage was fixed temporarily using tec7. In future projects, it would be preferable to replace the chamber to avoid future leakage.

**(a)**                                                     **(b)**

**Figure 5.4:** Fig 5.4a: Leaking of the chamber due to a defect in the top element. 5.4b: Leakage temporarily fixed with tec7.

## 5.2    Cone penetration testing and interpretation parameters

Initially, in order to further minimize the boundary effects, it was desirable to use the mini probe penetrometer to increase the chamber to cone ratio. Inevitably, problems with the registration of sounding data occurred, thus making it difficult to use the mini probe for testing. A lot of time was spent in the laboratory working on examining the problem with the mini-probe and trying to establish a connection between the cone and the data acquisition system. The problem could not be fixed, and in consultation with Geomil Equipment, it was decided that the cone would be submitted for repair. The decision to use the standard cone penetrometer for the rest of the experiments was made to secure progress in the project due to the limited time. For future projects, it is desirable to use the mini probe penetrometer if possible to increase the chamber to cone ratio.

Because of the problem with the mini probe, the sounding results from section 1 in the center of the chamber for experiment M1 were not obtained. In fact, the sounding results of section 1 were lost for all experiments. For experiment M2 the sounding was not obtained due to the overburden stress exceeding the capacity of the actuator. For this experiment, the aim was to achieve a more dense sample with greater density than the prior experiment. Hence, the compaction time was increased by 10 seconds per built-in layer. The actuator has a capacity of 9.5 kN, and with the increase in compaction time and the surcharge load of 80 kPa, the capacity was exceeded. Consequently, during the sounding of section 1, the capacity was reached, resulting in the emergency stop of the actuator being activated. The surcharge load was unloaded from 80 kPa to 40 kPa before proceeding with the sounding. However, the sounding

result was not optimal and is therefore disregarded. For the remaining sounding for experiment M2, it was expected that the influence of the spacing of the sections would mean that the cone resistance would not exceed the capacity of the actuator. It was therefore decided that the surcharge load could again be increased to 80 kPa for the soundings of the remaining sections 3a, 3b and 3c.
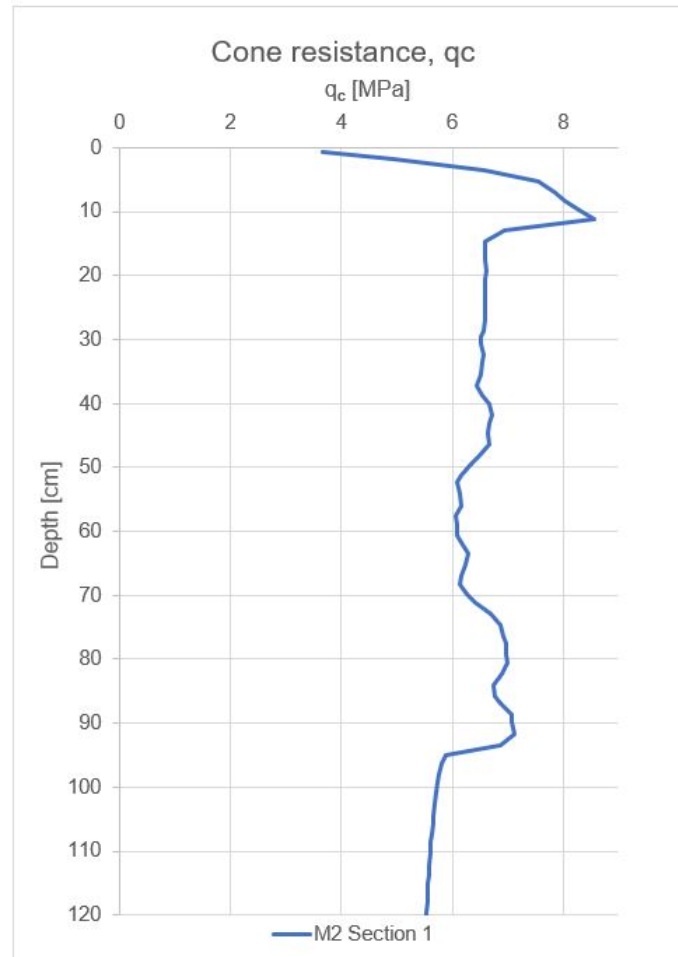


**Figure 5.5:** The cone resistance, qt, for Experiment M2, section 1 in the center of the chamber. Cone resistance exceeded the capacity for the actuator of 9.5 MPa, whereas the emergency stop for the actuator caused a disruption in the sounding at approximately 20 cm depth. The chamber was unloaded from 80 to 40 kPa before proceeding the sounding.

The CPTU results from section 1 showed, however, that the cone resistance was influenced by the spacing between the soundings. The cone resistance from section 1 is presented in figure 5.5. The sounding from the center shows that the cone resistance exceeds 9.5 MPa, and the cone resistance line does not show any signs that the peak cone resistance was reached and could therefore be higher than 9.5 MPa. When using a cone with an area of $10cm^2$, this results in an axial load for the actuator of $9,5kN$, which was the maximum axial load before the emergency stop was activated. In addition, the cone resistance after unloading the surcharge load from 80 kPa to 40 kPa shows a cone resistance of

about 7 MPa, which is higher than the cone resistance of the remaining sections. This shows that there are some effects because of the distance between the soundings. The first sounding will influence the next, leading to a decrease in tip resistance. This effect will influence the results. In this study, the parameters measured and compared are all taken inside the same chamber. In addition, the sand under the cone tip will more or less behave the same for the same stresses. The stiff wall of the chamber could lead to higher measured tip resistance, a bigger zone of plastification, and a more negative $\beta$ under the advancing cone. These influences make no difference in achieving the goals of the research work. In other words, it does not matter whether the stresses are higher or lower in free field conditions because the sand will act the same for the same stresses. Therefore, the tip resistance is not adjusted for boundary effects and is presented just as measured.

To ensure that the capacity of the actuator is not exceeded in future experiments, the density should be determined prior to sample construction by weighing the sand and building in with the respective height to the desired void ratio. In addition, an actuator with a larger capacity could also be used to conduct experiments with higher density samples. This would, however, lead to the actuator having to be lifted by the hoist because of the size of the actuator, which would lead to more labor during laboratory work.

For the last experiment, M3, the soundings from the center of the chamber showed way less cone resistance than expected with the given density of the sample and the overburden load of 80 kPa. This could be due to the cone not being adequately saturated or calibrated. It was therefore chosen to disregard these results in their entirety.

The cone penetration results show increasing tip resistance and side friction in the first $20 - 25cm$. This is caused by the extra load applied on top of the test specimen. This results in inhomogeneous conditions in the top compared to the next $60 - 65cm$. The same is for the bottom of the test specimen, where one can see a tendency of over compaction and increasing tip resistance towards a firmer layer in the bottom of the chamber. Based on this, the results from $25 - 85cm$ were mainly used for interpretation. The selected part of the test specimen is indicated in Figure 4.2, 4.3 and 4.4.

Even by neglecting the outermost points from the results, there were still some variations in tip resistance and side friction. As discussed in the previous chapter, this is caused by the build-in procedure, which makes it challenging to achieve a homogeneous test sample. The variations are relatively small, between 25 and 85 cm and the tip resistance is more or less 4 MPa in positions 3a, 3b and 3c for the three experiments. The side friction varies from 10 - 20 kPa in the same positions. As described in Chapter 3.6.1, the test specimen is built in layers. All the layers are saturated with an upward acting gradient. When the water expelled on the surface, very fine material sediment on the top of each layer. The fine material on the top of one layer is shown in Figure 5.6. This process could have caused a variation in density and void ratio, which leads to higher resistance in some parts and lower resistance in other parts. The small variations in tip resistance and side friction between $25 - 85$ cm could also be caused by the soundings affecting each other. The first sounding shows a higher tip resistance and side friction than the second and third sounding, which indicates that there is more space to push the ma-

terial away in the second and third sounding, leading to less resistance. The pore pressure is increasing hydrostatic by depth as expected.



(a)                  (b)
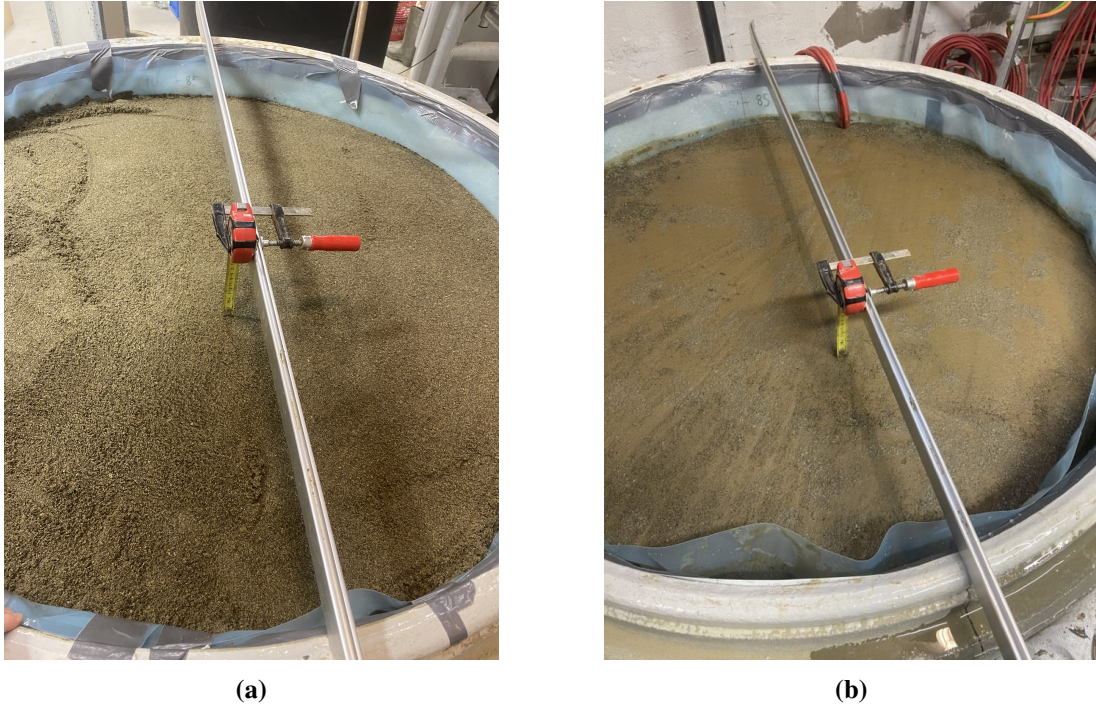
**Figure 5.6:** Fig 5.6a: Sand sample before saturated with water. Fig 5.6b: Fine material on top of one layer caused by the upward acting gradient for saturation of the sand from the bottom of the chamber.

## 5.2.1 Relative density and void ratio

After the sounding, the test specimen is unloaded, and the sand is excavated in layers of 10 cm. For every 10 cm, one density test is taken from each section in the chamber AB, BC and AC. From these measurements, one can see the same variations and tendency as in the tip resistance. Relative density, void ratio and average void ratio are presented in Chapter 4.2. The relative density seems to vary more than the void ratio. The reason might be that the relative density relay on the $e_{max}$ and the $e_{min}$ values. These values are determine by a test and this creates more uncertainty in the results. The measured relative density is plotted against empirical solutions for the relative density like NGI-99 approach Karlsrud et al. (2005) and from Lunne and Christoffersen (1983), see Figure 4.2. Some of the measured points are right on top of the empirical solutions, and some are higher and some are lower, but the tendency is more or less the same. The measured relative density increase with increasing tip resistance and decrease with decreasing tip resistance. As mentioned, there is more uncertainty to relative density than the void ratio, and therefore is the void ratio more used in this work than the relative density.

The void ratio is more consistent, and by taking an average of the void ratios from each sector for the same depth, one gets even more consistent results. The results show that ta higher relative density or

lower void ratio, the measurements differ less. For example, experiment M2 shows less variation in void ratio compared to experiment M1. The reason could be that the material is easier to keep in the testing cylinder when it is denser. If material fall out of the testing cylinder or the test cylinder is not fully filled, the weight of the mass in the cylinder will be too small and the void ratio too high. Other conditions affecting the void ratio could be that the test specimen is unloaded, and some sand is dug out when the density tests are taken, which again leads to swelling. This results in high measurements of the void ratio compared to the tip resistance, which again leads to a smaller friction angle $\phi$, estimated from the void ratio. When plotting $\phi$, based on void ratio, against $N_q$ in a bearing capacity diagram after Janbu and Senneset one can see that $\phi$ is underestimated compared to $N_q$. The results lie above the gray area which indicates the expected results. Figure 4.15b shows the results and as mentioned, one can see that the points are too high up compared to the shaded area. The measurements of void ratio should have been much more precise, but unfortunately they are not, so this needs to be accounted for and taken into consideration when using void ratio in other calculations and before the conclusion. Comparing $\phi$, estimated from the triaxial tests and interpolated with void ratio, with the empirical solution from P. Robertson and R. Campanella (1983), one can see that also this indicates that $\phi$ is underestimated when using measured void ratio. This is seen from Figure **??** where $\phi$ estimated from P. Robertson and R. Campanella (1983) gives points in the shaded area when it is compared to $N_q$, and the other results do not.

## 5.3  Analysis of soil behaviour

Literature shows how the relative density has been used as the governing parameter to determine the friction angle $\phi$. The relative density describes how dense the soil is packed and the denser material, the higher friction. There are many empirical solutions where one can determine the relative density of the tip resistance from a CPT. These empirical solutions give a fairly good prediction of the friction angle, but relative density does not take into account the stress conditions, in the sense that a given relative density is not directly associated with a certain stress. Sand behavior is stress dependent and to get a better understanding of the sand, the stress dependent state parameter, $\psi_{BJ}$ is evaluated. Clay has been studied quite a bit for many years due to the risk of geohazards, while the investigations of sand have been somewhat disregarded. The understanding of sand behavior is also very important to understand thin layers of clay in sand and the transition between these two materials. The state parameter $\psi_{BJ}$ is the difference in void ratio from a given state to the critical state for a given stress. This parameter is stress dependent and will take into account a different behavior for a different stress and will be quite useful to get a better understanding of the behavior of sand. The state parameter is determined from the measured void ratio and the critical state line for the same stress. The critical state line is determined from two triaxial tests and the inclination comes from one oedometer test of the investigated sand. The different measured void ratios are compared to the critical state line and state parameters can be plotted against depth and compared to other parameters. This is further discussed in the next chapter.

Under the advancing cone, some of the material is compressed elastically, and some of the material gets plastic deformations. How much of the material gets elastic deformation and plastic deformations depends on the stress and how dense the material is packed. The transition is expressed by the plastification angle, $\beta$. The state parameter takes into account the stress and the density and tells a lot about how the soil will interact with the penetrating cone.

### 5.3.1 Critical state and state parameter

The state parameter results are presented in two graphs for each experiment. One graph contains the empirical results from Been et al. (1987), and the other contains the measured state parameter from the chamber tests (see Figures 4.11, 4.12 and 4.13). These results show that the measured state parameter is slightly positive, and the empirical solution from Been et al. (1987) is slightly negative. The same tendency can, in some parts, be found by comparing the two results. A state parameter close to zero means that the actual state is close to the critical state, and the material will not dilate or contract when it is exposed to great shear stresses. The three different graphs in Figures 4.11, 4.12 and 4.13 based on Been et al. (1987) vary slightly from each other by depth. This is related to the tip resistance, and it can be observed that the higher the tip resistance, the more negative state. These variations come from the same reasons as discussed earlier, such as the build-in procedure and the different sounding's impact on each other. To comment on the result from the measured state, these results depend on many factors. The measured state parameter depends on the critical state line and the measured void ratio from the chamber tests. These two factors again depend on many other factors with some amount of uncertainty. For example, the inclination of the critical state line $\lambda_{ss}$, the critical state points from the triaxial tests, and the uncertainty coming with the measured void ratio due to human error. The reason for discussing this is not to understate the results but to show awareness of the possible sources of uncertainties. This could be the reason why the measured state parameters are slightly positive because too high a value of void ratio gives a too high value of the state parameter. This is important to take into consideration when concluding on the objectives on this thesis.

It is also worth mentioning that Been et al. (1987) based their theory on undrained triaxial tests, CIU and CAU, run until liquefaction. Figure 5.7 shows an example of a state diagram for Kogyuk 350/2 sand from Been and Jefferies (1985). The figure shows the critical state line based on CIU and CAU test and some CID tests after consolidation. The work done in this project is based on CID, drained triaxial test that was run to large vertical strain. Considering these two quite different tests defining the same concept of the critical state, one could question whether the results from the two tests could be considered to be the same state. The concept of the critical state is large shear strains without any change in volume or effective stress. A CIU or CAU test is run undrained, with no change in volume, and when liquefaction occurs, there is no change in effective stress. Hence, the requirements are fulfilled, and the critical state is reached. A CID test is run to large axial strain, up to 30%, until the volume and the shear stress converge towards a constant value. Thus the requirements are also fulfilled for this test. Even though both tests fulfill the requirements for the critical state, some difference in the results for

the critical state line is expected. In the undrained test, the sand particles float in water, while in the drained test, the water is pushed out, and the water content is smaller. Another perspective is that in an undrained test, most of the sample liquefies at the same time, and an average void ratio of the whole sample is a good estimation for the liquefied material. In a drained test, there is only the shear band that reaches the critical state, and it is impossible to determine the void ratio for the shear band alone. This implies that the fit of the average void ratio is not as good for the drained test as for the undrained test. Results for the same type of tests vary; therefore, the results from two different types of tests are expected to vary.
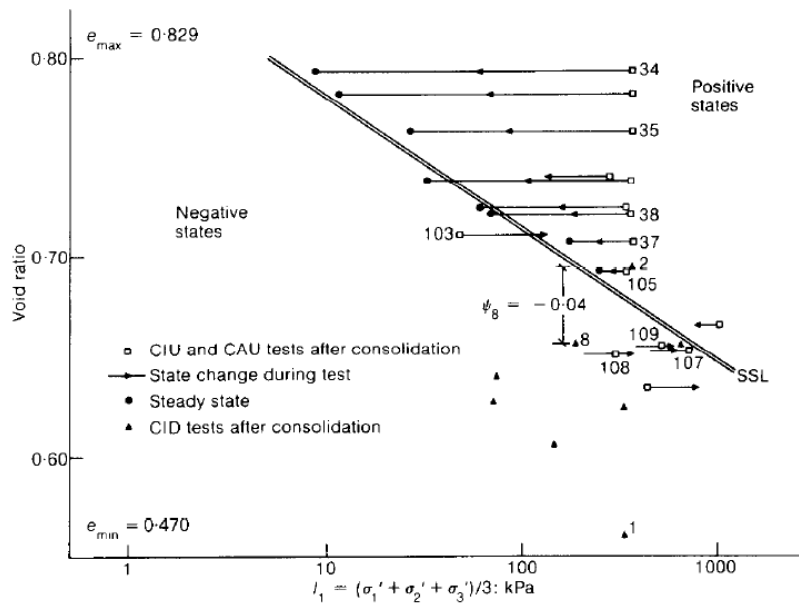


**Figure 5.7:** State diagram for Kogyuk 350/2 sand Been and Jefferies (1985).

The triaxial and oedometer tests are plotted in the same plot as the critical state line (see Figure 4.9). The two triaxial tests give two points on the critical state line, and the inclination of the critical state line is given by the oedometer test with relative density of 65%. This method for determination of the flexibility parameter $\lambda$ is done according to the theory presented in Chapter 2.4. The oedometer test that was built in with a relative density of 45% collapsed when the sample was saturated in the oedometer cell. This made a drop in the $\sigma'_a$ - Module curve, and the inclination for the first 200 kPa was hard to determine. Therefore, the modulus number is only based on the oedometer test with a relative density of 65%. The collapse of the loosest sample was expected. When adding water to a loose and dry sand sample, the sand will contract because of the apparent attraction occurring. When the sample collapse, the axial stress drops, and because the piston is strain-controlled, this results in a drop in the curve, as mentioned. The critical state line could also be found by determining many critical state points from a series of different triaxial tests. This method was not possible due to the limited time and an already large laboratory schedule. The first triaxial test was conducted at NGI in Oslo. The intention was to build in a test with a relative density of 65%, but it ended up with a relative density of about 50% and

106

a void ratio of 0.7. The triaxial test conducted at NTNU had the same build in density but slightly less mean stress p'. Both of the tests were run to great axial strain. The test at NTNU was run to 30% axial strain, and the test at NGI was run to 20% axial strain. It is important to run the tests to great axial strain to ensure that the critical state is reached.

The resulting critical state parameters are briefly discussed in the previous paragraph. The graphs in Figures 4.11, 4.12 and 4.13 show a state parameter around zero, or slightly over or under the critical state. A state parameter around zero indicates no volumetric change of the material when shear stress is applied. The sand is loose to medium dense with a void ratio from 0.8 to 0.65. However, as mentioned, the measured void ratio is probably overestimated. Medium dense sand could possibly be at a critical state and not dilate or contract when shearing. The triaxial tests are built in with a void ratio of 0.7, and the results show no significant change in void ratio when approaching critical state. The void ratio changes about 0.02 in the triaxial tests, which is just slightly less than $\psi_{BJ}$ presented in the graphs based on Been et al. (1987), see Figure 4.12. Comparing the results obtained from this work to the studies conducted by Been et al. (1987), this sand is close to the Ottawa and the Monterey no. zero sand. Figure 2.18 and Table 2.2 shows the results for Ottawa and Monterey no. 0. The sand studied in this work has m, k and $\lambda_{ss}$ equal 11.86, 49.88 and 0.0231, respectively.

### 5.3.2 The reliability of the state parameter approach

The state parameter approach is relatively new, and the method could need further validation. Sladen (1989) questioned the linear relationship for interpreting the state parameter from cone resistance suggested by Been et al. (1987). This was due to the small range of $9.9 - 11.7$ for the parameter m, which is the gradient of the normalized $(q_c - p)/p' - \psi_{BJ}$-space. Sladen stated that since the state parameter along the x-axis was plotted on a logarithmic scale, any small scatter in the state parameter would lead to the normalized $q_c$ varying with a factor of 3. A clear linear relationship could be observed. However, it might not be uniquely defined for all stress levels.
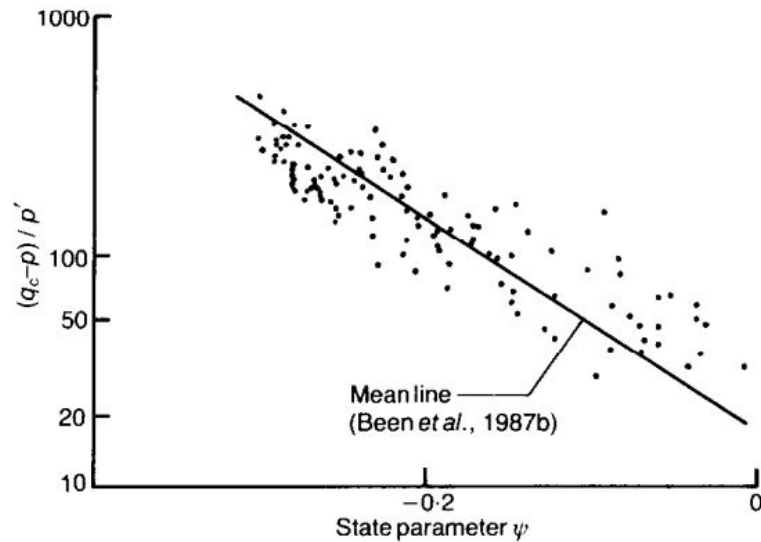
**Figure 5.8:** Normalized tip resistance, $q_c$ - state parameter $\psi_{BJ}$ for normally consolidated Ticino sand. Based on chamber testing by Baldi et. al. (1986). The critical state line presented by Been et al. (1987). Shows some scatter which would lead to greater variations for normalized $q_c$. From Sladen (1989).

The gradient, m, of the normalized $q_c$ - $\psi_{BJ}$ - space was determined for the Søberg sand to try to validate that the correlation suggested by Been et al. (1987) can be applied to Søberg sand. The thought was that if the gradient, m, lies within the same range as the sand materials investigated by Been et al. (1987), then the correlation would apply to the Søberg sand. As the gradient was determined to be 11.87, it is assumed that the correlation is applicable in this study.

### 5.3.3   Correlation between state parameter and plastification angle

Using the bearing capacity theory, the plastification angle is an important parameter for the stress field around the cone, as it limits the plastified soil deformation during cone penetration. Therefore, it was an obvious parameter to investigate when the soil behaviour during cone penetration was to be studied. Instead of assuming the plastification angle when interpreting the CPTU-results using the NTH method as done today, the goal of this thesis is to determine a more accurate and realistic plastification angle to be again able to determine a correct friction angle. The correlation between $\beta$ and the state parameter $\psi_{BJ}$ is investigated by plotting the two parameters against each other by depth. The theoretical relation is also investigated by setting equations 3.12 and 2.15 equal to each other, see Chapter 3.7.2. The correlation determined through this study is based on the empirical solutions suggested by Been et al. (1987) and on the definition of state by measured void ratio is presented in Figures 4.17 and 4.18, respectively.

$\beta$ is plotted against depth in Figure 4.8, and some variations for the different soundings are observed. Some parts looks $\beta$ quite different for the different soundings in the same experiment, for example M1.

$\beta$ is dependent on the friction angle determined from triaxial tests and interpolated with void ratio and the bearing capacity factor $N_q$. When the friction angle estimated from the void ratio does not fit very well with $N_q$, the impact on the results in $\beta$ is very significant, which could explain the variations in $\beta$. $\beta$ seems to mainly vary between 0 and $-25$ and at least in experiment M2 $\beta$ decrease, gets more negative by depth, as expected. Experiment M2 was the densest packed experiment, and the void ratio measurements were better for M2 than M1 and M3. Experiment M3 also tends to decrease $\beta$ by depth, but experiment M1 does not seem to have a clear tendency. The results in $\beta$ are a little bit surprising, where the results of the plastification field was expected to be smaller because the state parameter, $\psi_{BJ}$, is around zero. After studying the results, it is logical that $\beta$ is negative. To generate a positive plastification angle, the surrounding material should be quite loose and have enough voids for the soil to have room to compress when the material is pushed aside by the cone.

Based on the empirical solutions for determining the state parameter, the results presented in Figure 4.17 show a linear correlation between the plastification angle and the state parameter. The state parameter describes whether the soil is dilative or contractive when exposed to more significant strains. For a dense sand sample, the soil being displaced by the cone will dilate. This will result in a larger plastification field because the sand around the cone would need a larger volume to dilate, and the plastification angle would hence be a larger negative value. A sand sample with greater density would also generate a larger negative state parameter because the void ratio of the sand would be smaller, and the soil would be less than the critical state. Logically, there would exist a linear correlation as observed. This linear correlation is confirmed by the derivation done in Chapter 3.7.2.

When it comes to the state parameter based on measured void ratio, the correlation to the plastification angle is a bit more challenging to determine. This could be explained by the fact that the void ratio is measured incrementally for each layer of 10 cm during the excavation of the chamber. Due to the incremental measurements, a jump is observed for the state parameter in figure 4.18. In reality, the void ratio would vary continuously with depth, and it can be assumed that the correlation would show the same trend as for the empirical solution for the state parameter presented in Figure 4.17. The exact correlation is, however, difficult to determine.

### 5.3.4 Correlation between the state parameter and friction angle

Based on the state parameter approach developed by Been et al. (1987), the friction angle can be assessed through the state parameter. The correlation found through this study is presented in figure 4.21. The results show the same tendencies of correlation as for Been et al. (1987).

This linear relationship between the measured state parameter $\psi_{BJ}$ and the friction angle $\phi$ shows some underestimation of the friction angle when plotting the friction in the NTH charts, as shown in figures 4.14a, 4.15a and 4.16a. This could also be due to the overestimation of the void ratio during sampling, as mentioned earlier. According to the $N_q$-$\tan\phi$-chart, the friction is too low compared to the bearing capacity factor, $N_q$. The friction can therefore be assumed to be higher. This also correlates

with the results from the triaxial test. According to the triaxial test, the given built-in void ratio of e= 0.7 gave an interpreted friction angle of 34°. The critical state line in Figure 4.10 shows that the given void ratio of 0.7 and the stress applied during triaxial testing of 60 kPa, give a void ratio close to the critical state line, and the state parameter should hence be close to zero. Looking at Figure 4.21, a state parameter of zero only generates a friction angle of 32.4°. In contrast, the friction angle for the given void ratio is determined to be 34° in the triaxial test. This suggests that all measured void ratios would generate approximately a friction angle of 2 degrees less than the actual friction for the given sand material, based on the linear interpolation from the triaxial test. In this case, the linear trend line presented in Figure 4.21 could be adjusted approximately two degrees higher. This would lead to a better fit in the $N_q$-tan$\phi$ chart and with the NTH method. The adjusted trend line is shown in figure 5.9.
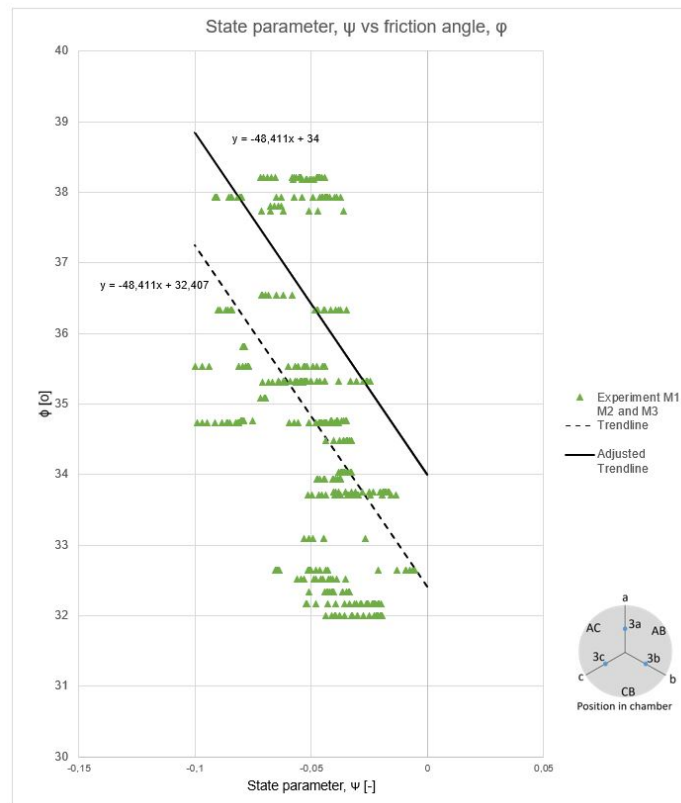


**Figure 5.9:** Correlation between the state parameter $\psi$ and friction angle $\beta$ adjusted for overestimation of void ratio.

### 5.3.5   Numerical Analysis

A numerical analysis was conducted using the Material point method. Unfortunately, the results did not confirm or refute the empirical results. The affected field around the cone is presented in Figure 4.26 and 4.27 by volumetric strain and shear strain, respectively. As commented in Chapter 4.5.2 the

material dilates or contracts depending on the dilatancy angle. Comparing the results obtained in this study with the results from Paniagua et al. (2018), she is able to locate the different zones from the volumetric strain, see Figure 2.8. This is not possible with the analytical results from the material point method. The visualization of the volumetric strain in Figure 4.26 does not identify the zones as the results do in Figure 2.8.

The analytical solution used in this study does not describe the soil behaviour quite correctly. A code for simulating soil accounting for density is under development and would give a more realistic soil behaviour. The new code will hopefully give better results and somehow confirm the empirical results.

# Chapter 6

# Conclusion

The cone penetration test is an important field test for assessing in situ design parameters due to its availability, cost-effectiveness, and simplicity. Although the CPTU-test is most commonly used on clay, in situ tests are also crucial for sand. This is because of the challenges in taking undisturbed samples of cohesionless soils for laboratory tests. In addition, the understanding of soil behaviour in sands during cone penetration could lead to better methods for the detection and accurate characterization of thin, weak layers in sand. The failure mechanism around the advancing cone tip is complex, and understanding this failure mechanism could improve the interpretation of the layering effects and the soil behaviour affecting the cone resistance between two layers.

The behaviour of sand is affected by the strength and stiffness of the sand. Both are influenced and controlled by the stress level and the porosity. A relative porosity may be used or possibly even more consistently, the state parameter for sand, $\psi_{BJ}$, defined by Been and Jefferies (1985). The plastification angle, $\beta$, used in the NTH method, depends on how loose or dense the sand is, and as such, it also varies with the friction angle. The obtained results in this work show a clear tendency of correlation between the state parameter, $\psi_{BJ}$ and the plastification angle, $\beta$. The correlation is valid for the range of stress applied in this study. The linear relationship can be used to assess the plastification angle, $\beta$, from the state parameter, $\psi_{BJ}$. It would significantly improve the NTH method, as the estimation of the plastification angle can be more theoretically consistent and less purely empirical. The observed correlation between the state parameter, $\psi_{BJ}$ and plastification angle, $\beta$, in addition to information on porosity or void ratio has given a better understanding of the sand behaviour under the advancing cone. A dilatancy angle will be around zero for a state parameter close to zero due to no volume change. Through these experiments, it is observed that the plastification angle will be negative at critical state. Small dilatancy or contraction occurs, and the stress field around the cone may be expressed by a critical state friction angle. The concept of considering the friction angle as a sum of a critical state friction angle and a dilatancy angle seems to work well. At a density higher than critical, the material dilates upon shearing, and the friction angle is the critical state friction angle plus the dilatancy angle. In our tests, the density is not very high, and friction may be close to the friction angle at critical state. The plastification field increases when the state parameter becomes negative, making $\beta$ less positive or even negative. Then the dilatancy angle is negative, and the soil material dilates. In the other case, when the state parameter becomes positive, the plastification field decrease, and the dilatancy angle is

negative, and the material dilates. These results are important factors to consider when detecting thin and weak layers in sand deposits.

The knowledge of how much the material contract or dilate, depending on the stress state, expressed by the state parameter and plastification angle, $\beta$, could be very helpful in further studies. This knowledge is fundamental when determining the design parameter. A theoretical relation is determined during this study, which expresses the plastification angle, $\beta$, with $\psi_{BJ}$. The $\beta$-values generated using this relation is very similar to the $\beta$-values determined from back-calculation using the NTH method. Thus supporting the applicability of implementing the state parameter approach to the NTH method.

The three chamber tests generated a large amount of data from the cone penetration test and the sampled density tests. A valuable and sufficient database was gathered with the results from triaxial tests, oedometer tests, and other supplementary laboratory tests. In some cases, the data was considered to be slightly off, like the measured void ratio. The results for void ratio plotted against depth confirm that the build-in procedure and the control of the density must be improved. However, even though there are some uncertainties in the measured void ratio, the behaviour of the sand can be analyzed from the observed trends and tendencies from the gathered data.

Analytical solutions were obtained using the Material Point Method, but these results do not confirm or refute the determined plastification angle, $\beta$, from the experimental work. As expected, the analytical results indicate dilation for a positive dilatancy angle, $\psi$, and contraction for a negative dilation angle.

## 6.1 Recommendations for Further Work

The laboratory set-up was successfully improved with a new surface treatment, epoxy coating, and a double layer of plastic lining with some low-friction oil between the two layers. These improvements showed to be effective in reducing the silo effect (chamber wall friction). This method is described in Chapter 3.3 and is highly recommended for future experiments.

It is found that it is challenging to build a homogeneous sand sample with the same density all through the sample. The density, void ratio, porosity or relative porosity did vary more than expected over the sample height. This makes high accuracy in the interpretation of the state parameter rather challenging. A variation in the state parameter and, consequently, the plastification angle must be expected over the height of the sample. It is found that the variation is less if the measurements close to the bottom of the chamber and close to the lid on top are left out. For further research, it is recommended to improve the procedure for building the sand into the chamber. The wetting and tamping process layer by layer should be carefully evaluated and improved.

The numerical model needs improvement, and a model that considers the density of the soil is under development. This model could simulate the plastification field around a penetrating cone more realistically, and it could be of great interest to conduct further simulations when such a model is developed.

# Bibliography

Been, K, JHA Crooks, DE Becker and MG Jefferies. 1986. 'The cone penetration test in sands: part I, state parameter interpretation'. *Geotechnique* 36 (2): 239–249.

Been, K, MG Jefferies, JHA Crooks and Leo Rothenburg. 1987. 'The cone penetration test in sands: part II, general inference of state'. *Geotechnique* 37 (3): 285–299.

Been, K, MG Jefferies and J Hachey. 1991. 'The critical state of sands'. *Geotechnique* 41 (3): 365–381.

Been, K., and M. G. Jefferies. 1985. 'A state parameter for sands'. *Géotechnique* 35 (2): 99–112.

Campanella, R.G., D. Gillespie and P. Robertson. 1982. 'Pore pressures during cone penetration testing.' *ESOPT II 2nd European Symposium on Penetration Testing* (January).

Emdal, Arnfinn. 2020. *Cone Penetration Test (CPTU) - TBA4110 Geotech Field and Laboratory Investigations* [in eng]. Trondheim.

Geoteknikk, Faggruppe for. 2020. *Compendium TBA4105 Geoteknikk Beregningsmetoder.*

Hammer, Hallvard Berner. 2020. 'Physical experiments on CPTU thin layer effects of thin clay layers embedded in sand'. Master's thesis, NTNU.

Hammer, Hallvard Berner, Steinar Nordal and Jean-Sebastien L'Heureux. In press(a). 'Detection of thin clay layers in sand using a standard CPTU probe'. *20th International Conference on Soil Mechanics and Geotechnical Engineering (ICSMGE).*

———. In press(b). 'Thin-layer detection from the cone resistance rate of change'. *20th International Conference on Soil Mechanics and Geotechnical Engineering (ICSMGE).*

Hill, R. 1950. 'The mathematical theory of plasticity, Clarendon'. *Oxford* 613:614.

ISO 22476-1:2012. *Geotechnical investigation and testing Field testing. In Part 1: Electrical cone and piezocone penetration test.* (Standard Norge).

Janbu, Nilmar, and Kåre Senneset. 1974. *Effective stress interpretation of in situ static penetration tests* [in eng].

Janbu, Nilmar, Kåre Senneset and Rolf Sandven. 1989. 'Evaluation of soil parameters from piezocone tests'. *Transportation research record,* no. 1235.

Jansscn, HA. 1895. 'Versuche uber getreidedruck in silozellen'. *Z,* 1045–1049.

Karlsrud, Kjell, C.J.F. Clausen and P.M. Aas. 2005. 'Bearing capacity of driven piles in clay, the NGI approach' (August): 775–782. https://doi.org/10.1201/NOE0415390637.ch88.
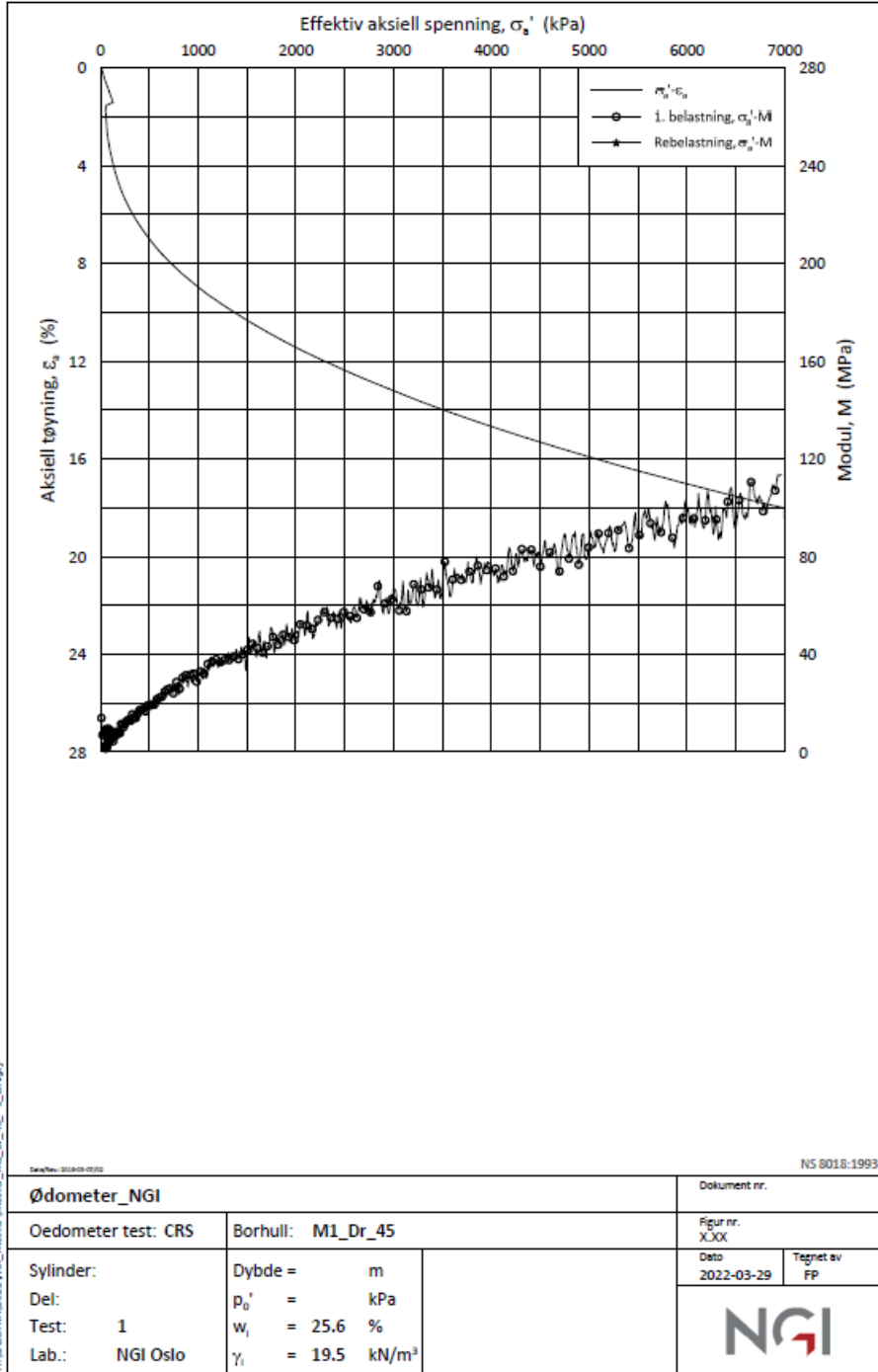
L'Heureux, J.S., Hansen. L, O Longva, A Emdal and L.O. Grande. 2010. 'A multidisciplinary study of submarine landslides at the Nidelva fjord delta, Central Norway - Implications for geohazard assessment' [in eng]. *Norwegian Journal of Geology* 90:1–20. issn: 029-196X.

*Interpretation of Cone Penetrometer Data for Offshore Sands.* 1983. Vol. All Days. OTC Offshore Technology Conference. OTC-4464-MS. May. https://doi.org/10.4043/4464-MS. eprint: https://onepetro.org/OTCONF/proceedings-pdf/83OTC/All-83OTC/OTC-4464-MS/2031919/otc-4464-ms.pdf. https://doi.org/10.4043/4464-MS.

Lunne, Tom, P.K Robertson and J.M. Powell. 1997. *Cone penetration testing in geotechnical practice* [in eng]. London.

Mayne, P. 1991. 'Calibration chamber database and boundary effects correction for CPT data'. In *Proc. 1st Int Symp. on Calibration Chamber Testing,* 257–264.

Mayne, Paul. 2-14th June 2019. *Ideas by professor Paul Mayne presented at discussion sessions at NGTS symposium.* Oslo.

Nordal, S. 2020. *Compendium. TBA4116: Geotechnical engineering, Advanced course.*

Ouyang, Zhongkun, and Paul W Mayne. 2019. 'Modified NTH Method for Assessing Effective Friction Angle of Normally Consolidated and Overconsolidated Clays from Piezocone Tests'. *Journal of geotechnical and geoenvironmental engineering* 145 (10): 4019067. issn: 1090-0241.

Paniagua, Priscilla, Arnfinn Emdal and Steinar Nordal. 2014. 'Failure mechanism and interpretation of CPTU in silty soils'. May.

Paniagua, Priscilla, Joana Fonseca, Anders Gylland and Steinar Nordal. 2018. 'Investigation of the change in soil fabric during cone penetration in silt using 2D measurements'. *Acta Geotechnica* 13 (1): 135–148. https://doi.org/10.1007/s11440-017-0559-8. https://doi.org/10.1007/s11440-017-0559-8.

Paniagua López, Ana Priscilla. 2014. *Model testing of cone penetration in silt with numerical simulations* [in eng]. Trondheim.

Parkin, AK, and T Lunne. 1982. 'Boundary effects in the laboratory calibration of a cone penetrometer for sand'. *Norwegian Geotechnical institute publication,* no. 138.

Robertson, P. K. 2009. 'Interpretation of cone penetration tests a unified approach' [in eng]. *Canadian geotechnical journal* (OTTAWA) 46 (11): 1337–1355. issn: 0008-3674.

Robertson, P. K, and R. G Campanella. 1983. 'Interpretation of cone penetration tests. Part II: Clay' [in eng]. *Canadian geotechnical journal* (Ottawa, Canada) 20 (4): 734–745. issn: 0008-3674.

Robertson, Peter, and R Campanella. 1983. 'Interpretation of cone penetration tests. Part I: Sand'. *Canadian geotechnical journal* 20 (4): 718–733.

Sandven, Rolf. 1990. *Strength and deformation properties of fine grained soils obtained from piezocone tests* [in eng]. Trondheim.

Sandven, K. Senneset, A. Emdal, S. Nordal, N. Janbu, L Grande and H.A. Amundsen. 2017. *Compendium. TBA4110: Geotechnics, Field and laboratory Investigations.*

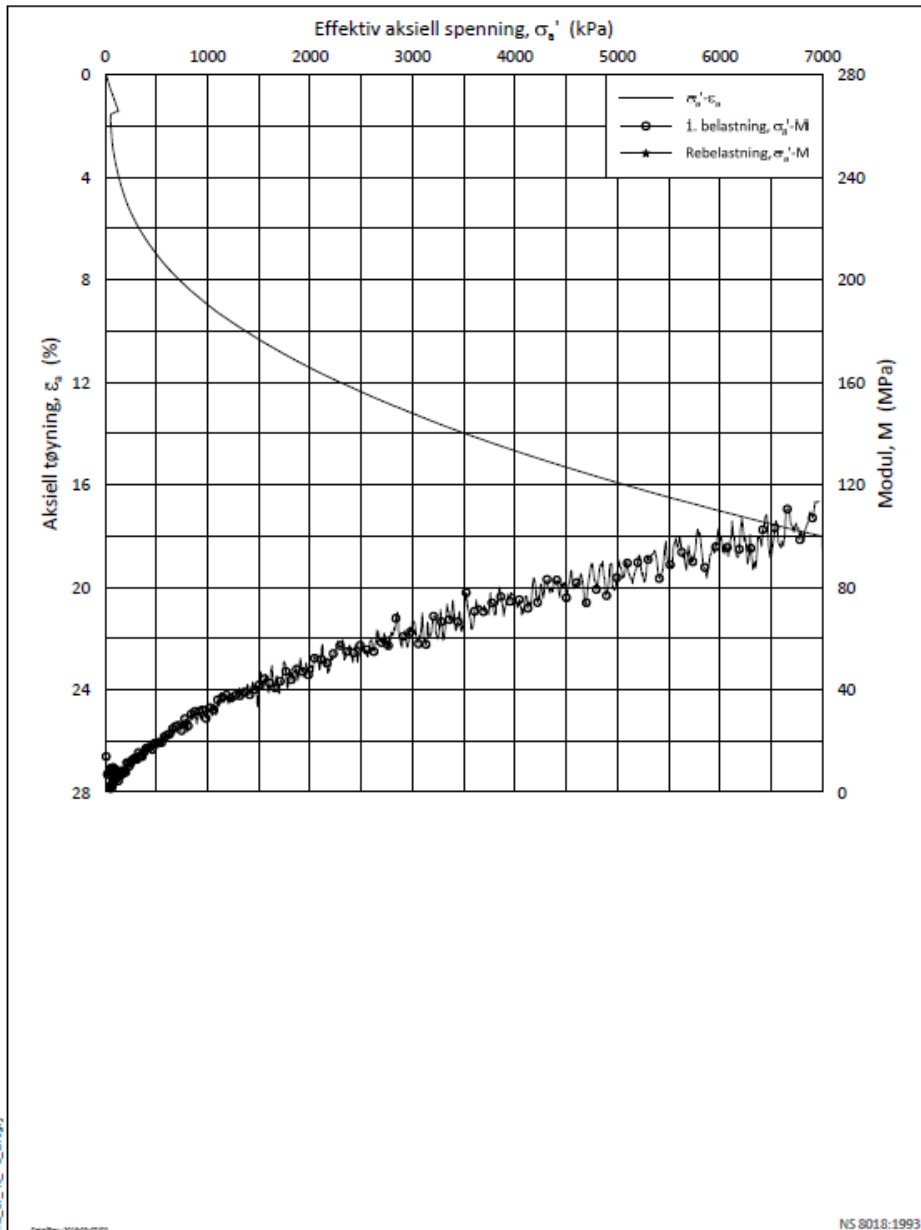Sandven, Kåre Senneset and Nilmar Janbu. 1988. *Interpretation of piezocone test in cohesive soils* [in und]. Trondheim.

Skrede, Hallvard. 2021. 'CPTU-detection of thin clay layers in sand'. Master's thesis, NTNU.

Sladen, J.A. 1989. 'Problems with interpretation of sand state from cone penetration test' [in eng]. *Géotechnique* (LONDON) 39 (2): 323–332. issn: 0016-8505.

Sulsky, Deborah, Zhen Chen and Howard L Schreyer. 1994. 'A particle method for history-dependent materials'. *Computer methods in applied mechanics and engineering* 118 (1-2): 179–196.

Tran, Quoc-Anh, and Wojciech Sołowski. 2019. 'Generalized Interpolation Material Point Method modelling of large deformation problems including strain-rate effects–Application to penetration and progressive failure problems'. *Computers and Geotechnics* 106:249–265.
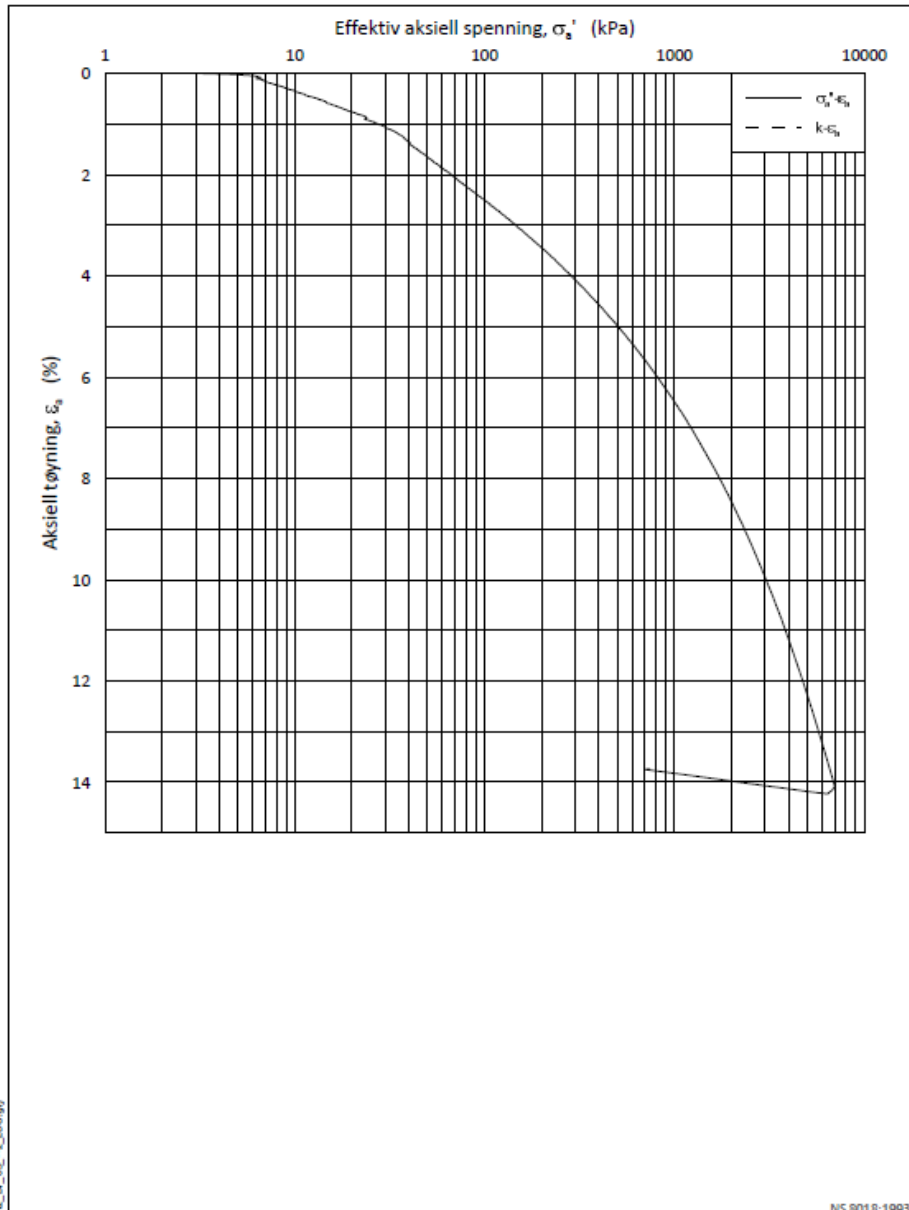
# Additional Material

# Appendix A

**Effektiv aksiell spenning, $\sigma_a'$ (kPa)**

Legend:
- $\sigma_a'$-$\varepsilon_a$
- 1. belastning, $\sigma_a'$-M
- Rebelastning, $\sigma_a'$-M

Y-axis (left): Aksiell tøyning, $\varepsilon_a$ (%)
Y-axis (right): Modul, M (MPa)

NS 8018:1993

| Ødometer_NGI | | | | Dokument nr. | |
|---|---|---|---|---|---|
| Oedometer test: CRS | Borhull: M1_Dr_45 | | | Figur nr. X.XX | |
| Sylinder: | Dybde = | | m | Dato 2022-03-29 | Tegnet av FP |
| Del: | $p_0'$ = | | kPa | | |
| Test: 1 | $w_i$ = 25.6 | % | | NGI | |
| Lab.: NGI Oslo | $\gamma_i$ = 19.5 | kN/m³ | | | |

**Effektiv aksiell spenning, $\sigma_a'$ (kPa)**

Aksiell tøyning, $\varepsilon_a$ (%)

Modul, M (MPa)

Legend:
- $\sigma_a'$-$\varepsilon_a$
- 1. belastning, $\sigma_a'$-M
- Rebelastning, $\sigma_a'$-M

NS 8018:1993

| | | | Dokument nr. |
|---|---|---|---|
| **Ødometer_NGI** | | | |
| Oedometer test: CRS | Borhull: M2_Dr_65 | | Figur nr. X.XX |
| Sylinder: | Dybde = m | | Dato 2022-03-29 / Tegnet av FP |
| Del: | $p_0'$ = kPa | | |
| Test: 2 | $w_i$ = 24.4 % | | NGI |
| Lab.: NGI Oslo | $\gamma_i$ = 19.6 kN/m³ | | |

Effektiv aksiell spenning, $\sigma_a'$ (kPa)

Aksiell tøyning, $\epsilon_a$ (%)

$\sigma_a'\text{-}\epsilon_a$

$k\text{-}\epsilon_a$

NS 8018:1993

| Ødometer_NGI | | Dokument nr. | |
|---|---|---|---|
| Ødometer test: CRS | Borhull: M2_Dr_65 | Figur nr. X.XX | |
| Sylinder: | Dybde = m | Dato 2022-03-29 | Tegnet av FP |
| Del: | $p_0'$ = kPa | | |
| Test: 2 | $w_l$ = 24.4 % | NGI | |
| Lab.: NGI Oslo | $\gamma_l$ = 19.6 kN/m³ | | |

Dato/Rev: 2018-05-0Y/01

# Appendix B

**NTNU plot**

Effective radial stress, σ'r (kPa)

(σ'a- σ'r )/2

- Dr 50 % (NTNU)
- Dr 50 % (NGI)
- Tolkning tanϕ=0,7



**p' - q**

Effective mean stress, p' [kPa]

deviatoric stress, q [kPa]

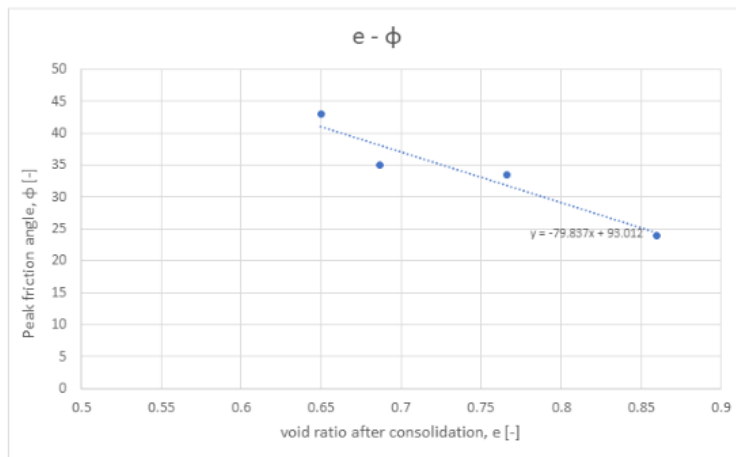- Dr 50 % (NTNU)
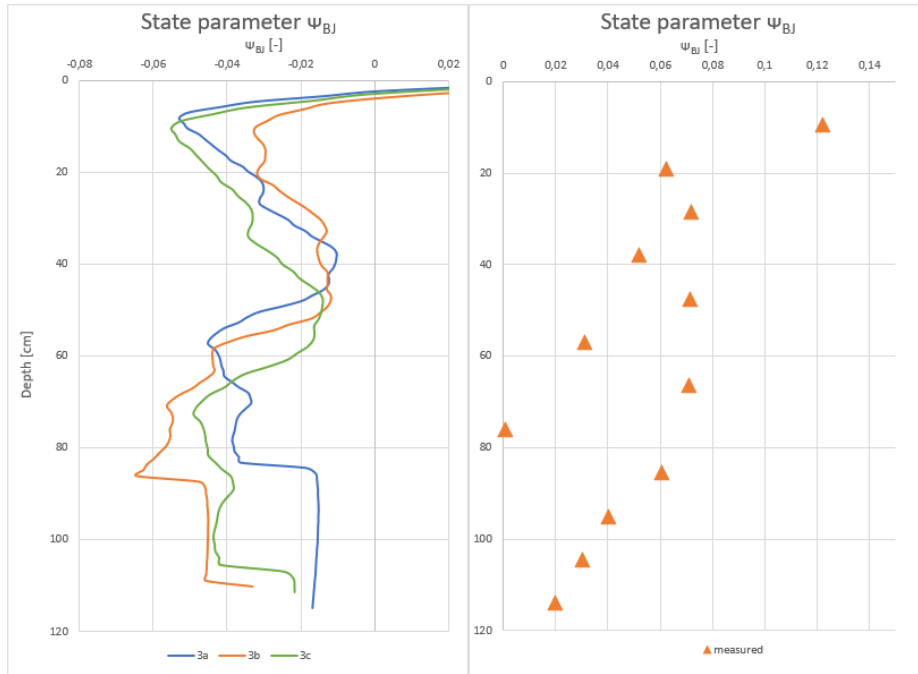- Dr 50 % (NGI)
- M-line

Void ratio vs peak friction angle for linear interpolation of friction angle. Results from triaxial tests performed by Hammer (2020) is also added.
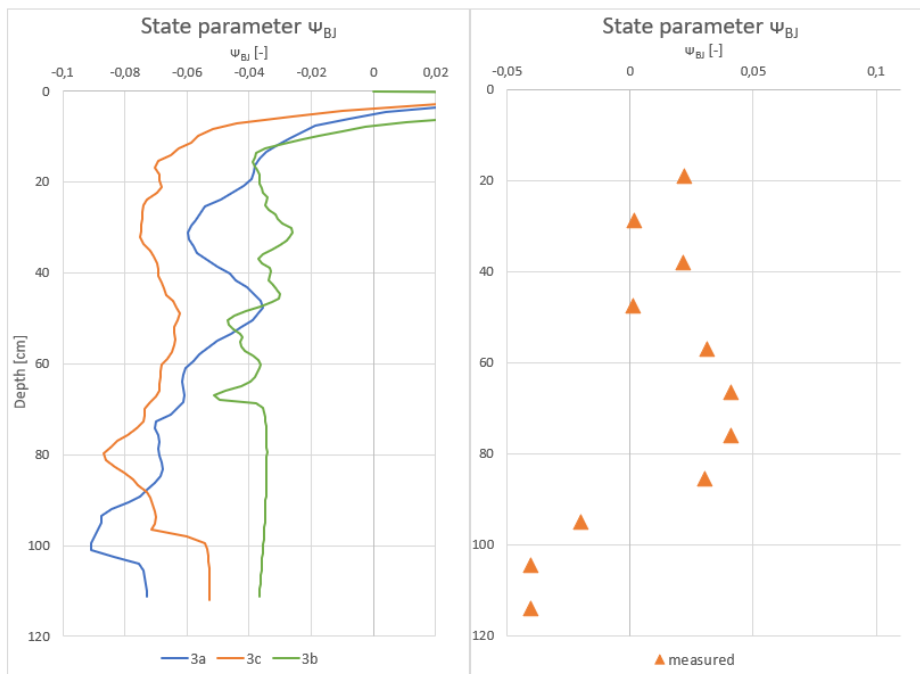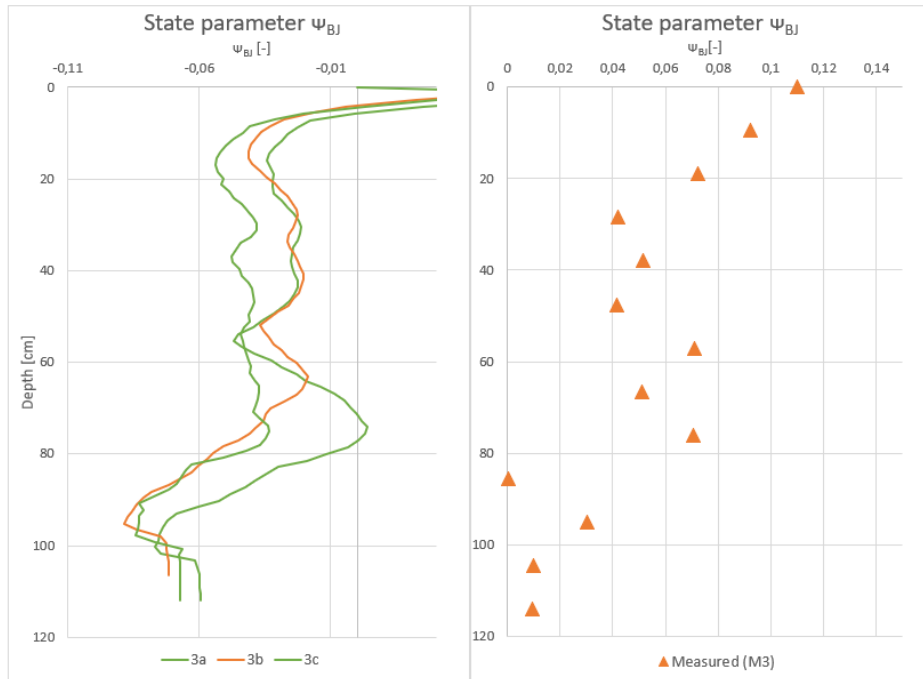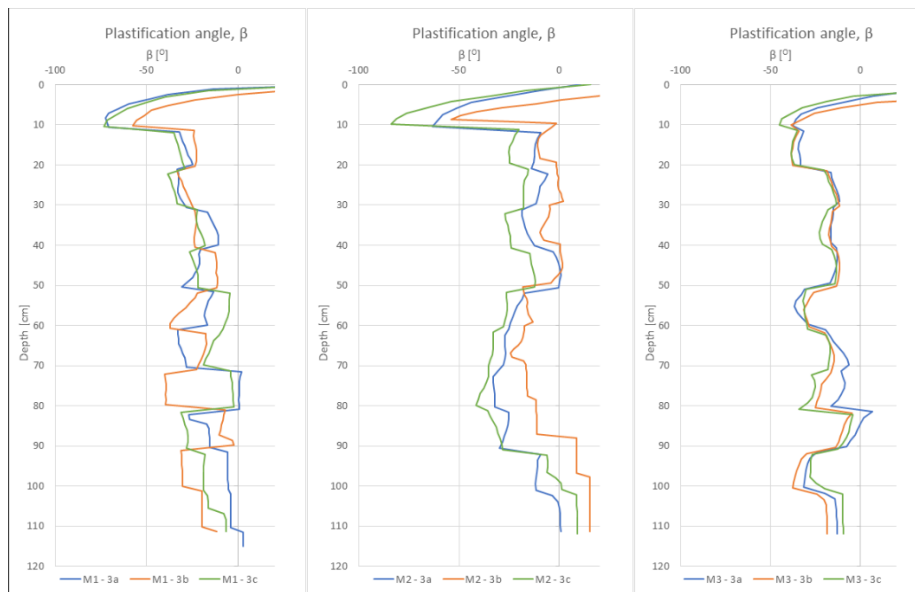
# Appendix C

State parameter $\psi_{BJ}$ — Experiment M1

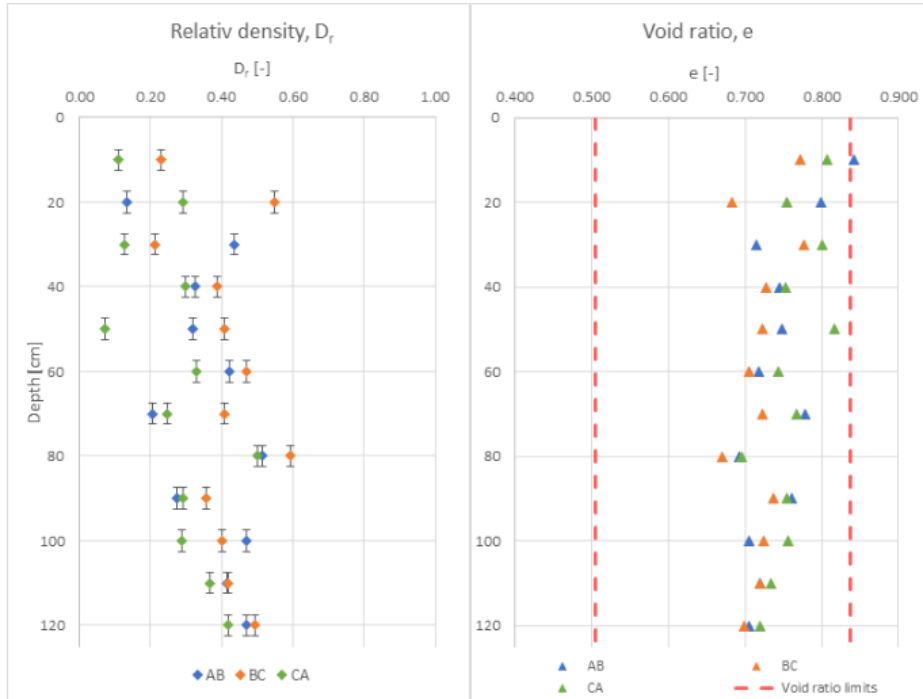State parameter $\psi_{BJ}$ — Experiment M2

State Parameter – Experiment M3



# Appendix D

# Appendix E

Density test M1



Density test M2
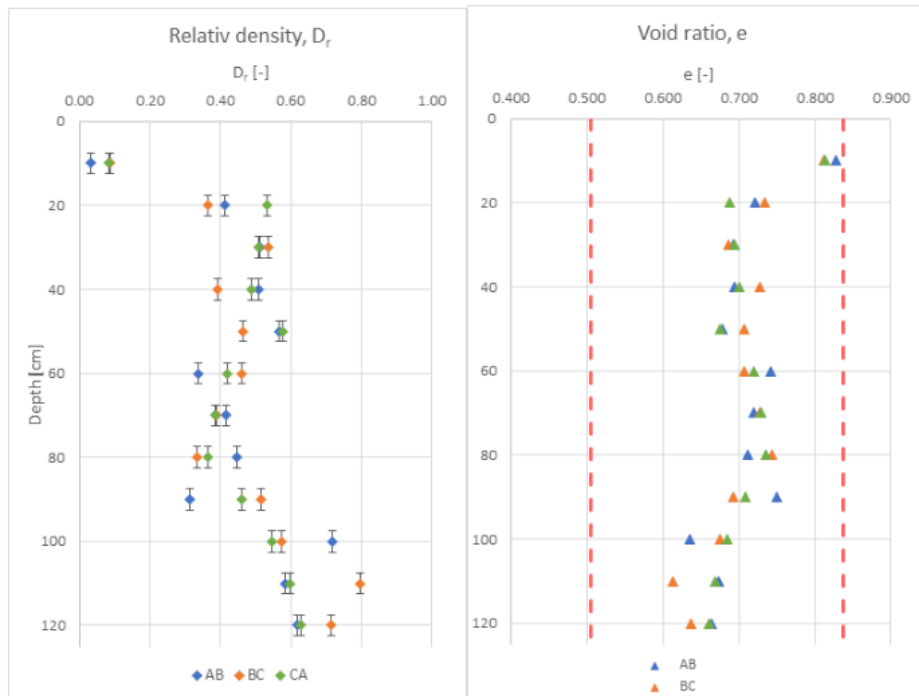
Density test M3

## Appendix F

# Grain Size Distribution

NTNU
Geoteknikk

| Test site: | Søberg Sand | | Date: | |
|---|---|---|---|---|
| Hole no: | | | Group: | |
| Depth: | | | Material: | |



| SIEVE | | Mass of retained material on each sieve [g] | | Sum of material retained on the sieve | | | Sum of material retained [%] | Remarks |
|---|---|---|---|---|---|---|---|---|
| | Sive opening [mm] | 1 | 2 | 1 | 2 | Mean | | |
| Vekt av prøve | | 1126,9 | 767,1 | | | 947 | | |
| | 63 | | | | | | | |
| | 45 | | | | | | | |
| | 31,5 | | | | | | | |
| | 19 | | | | | | | |
| | 16 | | | | | | | |
| | 11,2 | | | | | | | |
| | 8 | 4,6 | 0 | 4,60 | 0 | 2,3 | 0,24 | |
| | 4 | 15,9 | 16,5 | 20,50 | 16,5 | 18,5 | 1,95 | |
| | 2 | 64 | 39,7 | 84,50 | 56,2 | 70,35 | 7,43 | |
| | 1 | 243,7 | 138,9 | 328,20 | 195,1 | 261,65 | 27,63 | |
| | 0,5 | 346,5 | 193,5 | 674,70 | 388,6 | 531,65 | 56,14 | |
| | 0,25 | 308,7 | 214,2 | 983,40 | 602,8 | 793,1 | 83,75 | |
| | 0,125 | 108,8 | 126,3 | 1092,20 | 729,1 | 910,65 | 96,16 | |
| | 0,063 | 24,4 | 28,80 | 1116,60 | 757,9 | 937,25 | 98,97 | |
| < 0.075 | 0,000 | 10,800 | 9,30 | 1127,40 | 767,2 | 947,3 | 100,03 | |
| Sum | | 1127,4 | 767,20 | 1127,4 | 767,20 | 947,3 | 100,03 | |
| Svinn | | -0,5 | -0,10 | | | | -0,03 | % |

# Appendix G

This gives a more detailed presentation and documentation of the laboratory work, in terms of the building of the samples. The build-in process is very time-consuming labor. Pictures illustrate the building process.

The bottom of the chamber is filled with a 10 cm layer of gravel to ensure that the water was evenly distributed in the sand sample during the filling of water. The base layer of gravel was covered with a synthetic fabric cloth to prevent any fine-grained particles from being washed out.



*Figure 1: Base layer of gravel and filter cloth*

Then, the first layer of sand is placed. On this layer, the earth pressure cells are built into the sample, then the water is filled such that the pressure cells are just covered with water. The pressure cells are then reset to zero.
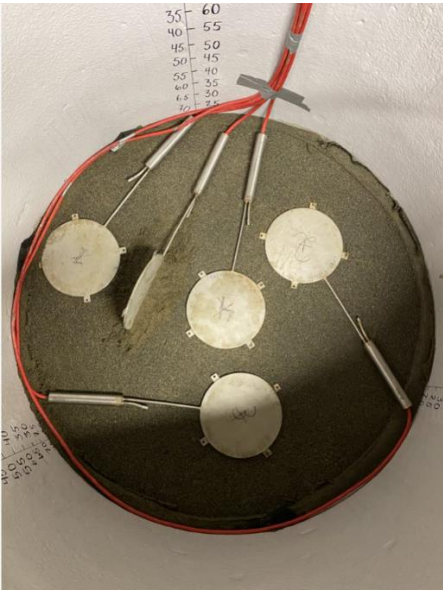


*Figure 2: Second layer with earth pressure cells*

Two layers of the plastic lining are added to the chamber, with a low-friction grease between them to limit the boundary effects from the chamber walls.



*Figure 1: Added plastic lining with low-friction grease.*

The height of the next layers is calculated to ensure the right density of the sample due to compaction. The sand is shoveled in and for each layer, the sand is leveled, and the depth is measured.



*Figure 2: The sand is shoveled in at 10 cm layers each. The height of each layer is carefully measured.*

Each layer is saturated with water from the bottom of the chamber. The layer is then leveled and measured again.



*Figure 3: The sand sample is saturated with water and the sample height is measured with each step.*

The water is emptied out and the depth is measured.



*Figure 4: Water is emptied to achieve even compaction. The height is then measured.*

After the water is emptied out, the plate vibrator is lifted inside the chamber on top of a wooden plate. The sand is vibrated for a given time and the plate vibrator and the wooden plate is lifted out. The final depth to the top of the layer is measured again.



*Figure 5: The sample is compacted using a plate vibrator. The final height of the layer is then measured.*

The build-in process is repeated for each layer of 10 cm until the base chamber is full, then all the cords and installments going into the chamber are disconnected and placed into the chamber. A rubber ring is placed along the edge of the bottom chamber, and the extension chamber element is then hoisted down on top of the base chamber. The equipment is then reconnected, and the build-in procedure is continued until the desired sample height is achieved (when the total 146 cm chamber is full). This follows the same procedure as described above.



*Figure 6: The extension chamber element is hoisted down and placed on the cottom chamber.*

When the chamber is fully filled, the loading frame is hoisted down on top of the sand and screwed on. The loading frame is secured in both directions using jack straps. This is to prevent the frame

from rotating. The extra simulated earth pressure is applied with air pressure. When the lid and extra pressure are applied, new measurements of the sample height are taken.



*Figure 7: The loading frame is installed, and new measurements of the height are taken.*

When the equipment is installed, the cone and computer are set up for testing. The actuator that pushes the cone into the sand sample is installed on wireframes above the chamber. These are secured with clamps to secure the position of the CPTU-test.



*Figure 8: The setup for CPTU-testing. Showing the actuator set up.*

The CPTU testing is conducted for each section, and in between each test, the cone is saturated.
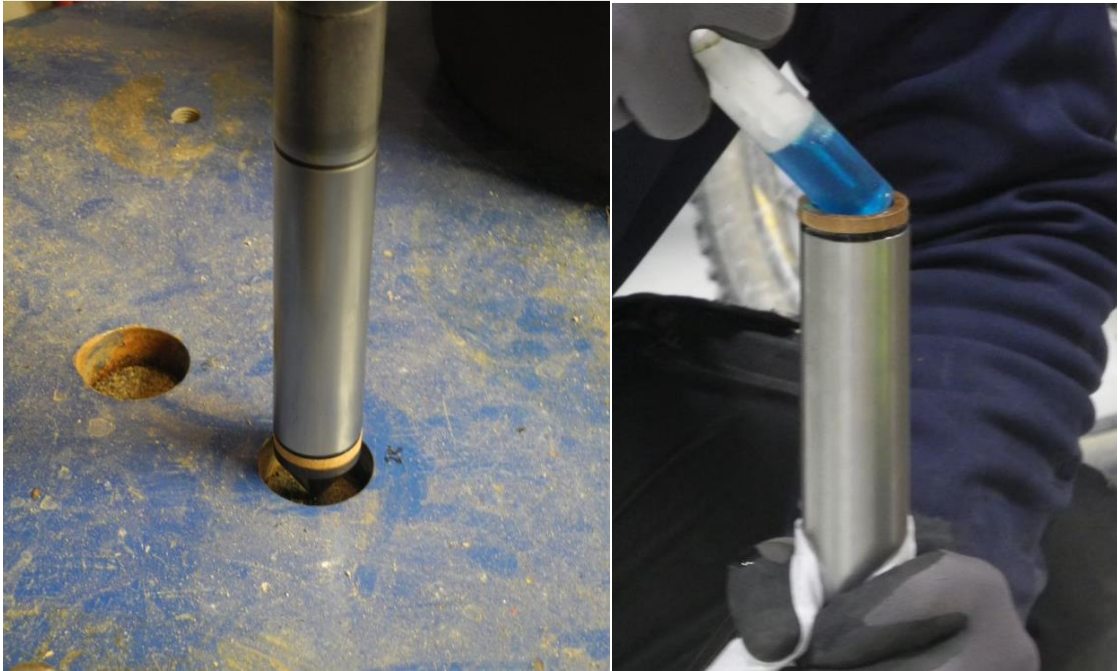


*Figure 9: Cone penetration testing is performed for each section, 1, 3a, 3b, 3c, and the cone is saturated between each test.*

After each test is complete. The pressure is unloaded, and the wireframes are hoisted up and removed from the chamber. It is then ready for excavating the chamber. This is a tedious process, as density tests are sampled for each section every 10 cm over the sample height.  The sample is carefully built out layer by layer, and density tests are sampled.



*Figure 10: Density tests are sampled for each layer of 10 cm.*

Karina T Eidem and Kristian W Lindgaard

Large scale model testing of CPTU in sand

**NTNU**
Norwegian University of
Science and Technology

NGI